UNIVERSITÀ
DEGLI STUDI
FIRENZE

DOTTORATO DI RICERCA IN
FISICA E ASTRONOMIA

CICLO XXIX

COORDINATORE Prof. Gurioli Massimo

Study of the very forward electromagnetic component produced in proton-proton collisions at $\sqrt{s}=13$ TeV with the LHCf experiment

Settore Scientifico Disciplinare FIS/04

Dottorando
Dott. Tiberio Alessio
Alessio Tiberio

Tutore
Dott. Bonechi Lorenzo
Lorenzo Bonechi

Coordinatore
Prof. Gurioli Massimo
Massimo Gurioli

Anni 2013/2016

Alla mia Principessa

Abstract

The main purpose of the LHCf experiment is to test phenomenological hadronic interaction models used to simulate cosmic rays induced air-showers in the Earth's atmosphere. The experiment is composed of two independent detectors (Arm1 and Arm2) located at 140 m from the ATLAS's interaction point (IP1) on opposite sides. The detectors are placed on the beam axis between the two beam pipes containing the colliding beams of LHC. This particular position allows LHCf to measure neutral secondary particles (mainly photons, π^0s and neutrons) produced at zero degrees. This work describes how the energy spectrum of photons produced in proton-proton collisions at $\sqrt{s} = 13$ TeV was obtained using the data measured by the Arm2 detector.

The relation between the total energy deposit in the calorimeters and the energy of the primary particle was studied with detailed Monte Carlo simulations of the detector. The correction for the non-uniformity of the detector response due to the shower leakage and due to the light collection efficiency of the scintillators was also studied with simulations.

The calibration of the detector was performed with a beam test at the CERN Super Proton Synchrotron using both electron and muon beams. An energy resolution of $\sim 2\%$ was found with electromagnetic showers and the linearity of the calorimeters was better than 0.5%. The correction for the leakage and light collection efficiency was also tested, resulting in a non-uniformity suppressed to the $\sim 1\%$ level.

The data acquired by the Arm2 detector in proton-proton collisions at $\sqrt{s} = 13$ TeV were reconstructed, corrected for the particle identification cut and unfolded to correct for the detector response. The energy spectrum of photons was compared with the predicted spectra from several hadronic interaction models in the pseudorapidity (η) regions $\eta > 10.94$ and $8.81 < \eta < 8.99$. There is not a single model well reproducing the data in the whole energy range, but the measured energy spectrum is enclosed between the predictions of the tested hadronic interaction models.

Contents

Chapter 1

Introduction

1.1 Cosmic rays physics

Cosmic rays are high-energy particles coming from the outer space that hit the Earth atmosphere. These high energy particles are produced and accelerated in astrophysical sources or by their interaction with the interstellar medium. When a cosmic ray interacts with a nucleus of the Earth atmosphere a shower of secondary particles (the so called “air-shower”) is produced. In this context the particle hitting the atmosphere is called “primary cosmic ray”, while the particles produced in the air-shower are called “secondary cosmic rays”.

Charged primary cosmic rays are composed of 86 % by protons, 11 % by helium nuclei, 1 % by heavier nuclei and 2 % by electrons [1]. Also positrons and antiprotons are present in small percentage, which are supposed to be produced in the interaction of cosmic rays with the interstellar medium. Neutral primary cosmic ray are composed instead of gamma rays, neutrinos and antineutrinos. When comparing the relative abundance of elements of the Solar System with elements composing cosmic rays, it can be noted that there is an excess of Li, Be, B and elements with atomic number $Z = 21 \div 25$ in cosmic rays with respect to the Solar System abundance, as can be seen in figure 1.1 [2]. The excess of Li, Be and B can be understood as the contribution of spallation reactions between light nuclei (like C and O) produced in the stellar nucleosynthesis and the interstellar hydrogen. Sc, Ti, V and Mn are produced instead by spallation of Fe and Ni nuclei.

Because of the galactic magnetic field, which is of the order of $1 \div 4$ μG [3], charged cosmic rays propagating in the interstellar space are deviated from their original direction. Since the typical distance travelled by a galactic cosmic ray is of the order of 10^6 parsec [4] and the radius of curvature of a

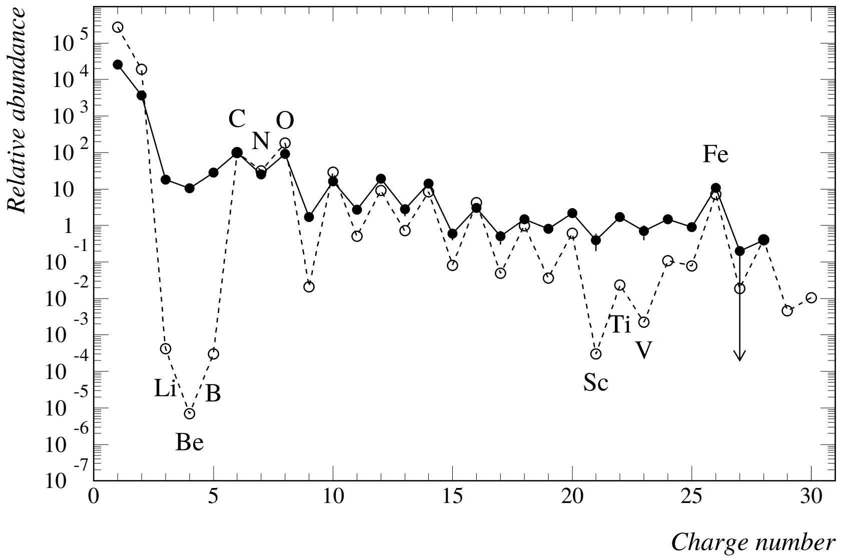

Figure 1.1: Relative abundance of elements in cosmic rays (solid line) compared with abundance in the Solar System (dashed line).

particle in the galactic magnetic field is much smaller than it (for example, 10^{-4} parsec for a proton with ∼1 TeV/c momentum), the information on the initial direction of the cosmic ray is lost. For this reason, the cosmic rays arrival direction appears to be uniform.

The energy spectrum of charged cosmic rays with energy above 10^8 eV is shown in figure 1.2 [1]. The spectrum of particles with an energy below 10^9 eV is influenced by the solar activity due to their interaction with the solar wind; during the periods with an higher solar activity the flux of cosmic rays is reduced [5]. The flux of cosmic rays can be described as a broken power law for energies above 10^9 eV:

$$\frac{dN}{dE} \propto \begin{cases} E^{-2.7} \text{ for } 10^9 \text{ eV} < E < 10^{16} \text{ eV} \\ E^{-3.0} \text{ for } 10^{16} \text{ eV} < E < 10^{18.5} \text{ eV} \\ E^{-2.7} \text{ for } E > 10^{18.5} \text{ eV} \end{cases} \tag{1.1}$$

The two turning points around $\sim 10^{16}$ eV and $\sim 10^{18.5}$ eV are called “knee” and “ankle”, respectively. The existence of the knee is attributed to the fact that the main mechanism which is though to be responsible for acceleration of galactic cosmic rays, the Fermi mechanism in supernovae [6,7], can accelerate particles up to $\sim 10^{15}$ eV. Furthermore, cosmic rays with energy above 10^{15} can not be confined in the galaxy by its magnetic field. Since the confinement

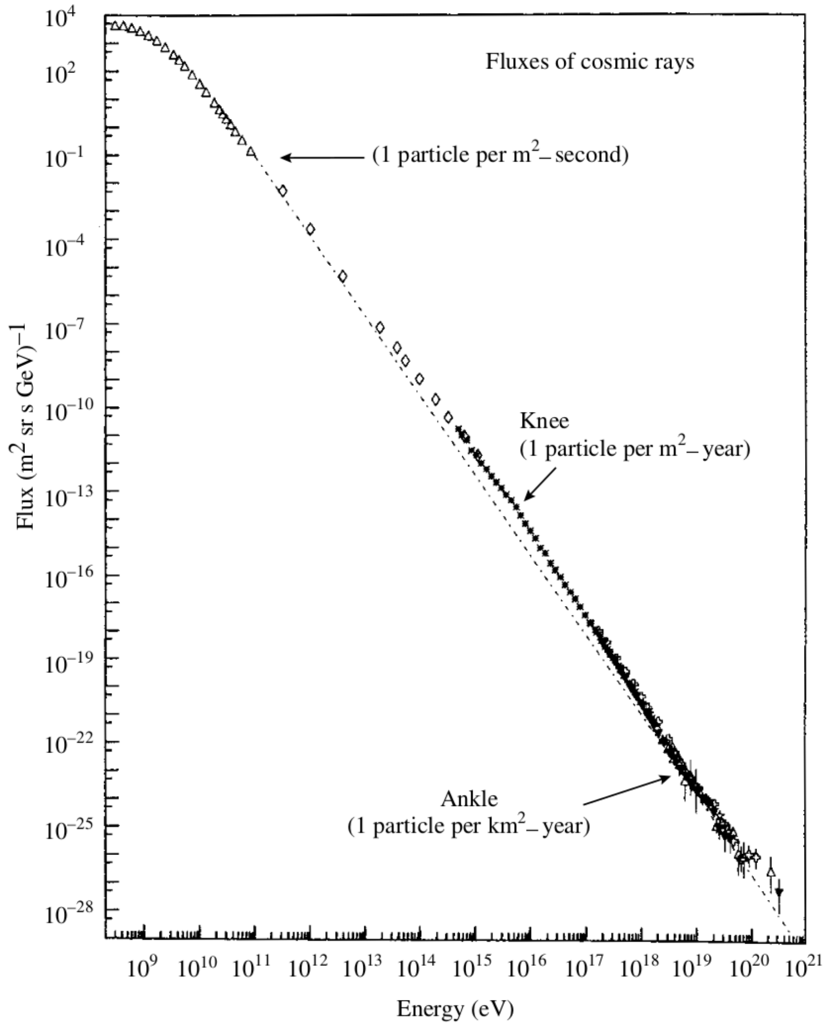

Figure 1.2: Flux of charged cosmic rays as a function of the energy. "Knee" and "ankle" point are indicated together with the flux of particles at energies above that points.

depends on the rigidity[1] of the particle, in addition to the energy dependence there is also a charge dependence. This implies that the element composition of cosmic rays is expected to change around the region of the knee. The ankle is interpreted as the energy where the contribution from extragalactic cosmic rays become dominant with respect to the galactic one. The principal

---

[1] The rigidity is defined as $R \equiv p/q$, where p is the momentum and q is the charge of the particle. The gyroradius r_L of a charged particle with rigidity R in a magnetic field B is $r_L = R/B$

candidates for accelerating such high energy particles are though to be Active Galactic Nuclei (AGN) and Gamma Ray Bursts (GRB).

An hypothesis proposed by Greisen, Zatsepin and Kuzmin in 1966 predicts a cutoff of the cosmic rays spectrum at energies around 10^{20} eV, the so called "GZK cutoff" [8, 9]: protons with energy above $\sim 4 \times 10^{19}$ eV can interact with photons of the Cosmic Microwave Background Radiation and undergo the reactions:

$$\begin{aligned} p + \gamma &\rightarrow p + \pi^0 \\ p + \gamma &\rightarrow n + \pi^+ \end{aligned} \tag{1.2}$$

The mean free path of this reaction is of the order of 3 Mpc, much less than typical intergalactic distances ($\sim 10 \div 100$ Mpc). So, if particles above the ankle are originated from extragalactic sources, the GZK cutoff must be observed. Latest experimental observations [10, 11] indicate the presence of the GZK cutoff in measured data, as shown in figure 1.3.

1.2 Indirect measurements of cosmic rays

Since the flux of cosmic rays rapidly decreases increasing the energy, direct measurements in the very high energy region using experiments placed on satellites are limited by the acceptance of the detectors, which must respect the mechanical constraints on weight and size of the satellites. In order to measure particles with energy above $\sim 10^{15}$ eV indirect measurements are performed observing the secondary particles produced by the interaction of the primary cosmic ray with a nucleus of the atmosphere.

The interaction of a primary cosmic ray with an atmospheric nucleus produces secondary particles which in turn decay or interact again with the atmosphere giving rise to the formation of an air-shower. The average hadronic interaction length is 10^2 g cm^{-2}, to be compared with the total thickness of the atmosphere which is 10^3 g cm^{-2} [1]; therefore, the first interaction happens generally in the Earth stratosphere. Most of the secondary particles produced in the first interaction are charged and neutral pions ($\pi^{\pm}$, π^0). π^0s quickly decays into two gammas which generate an electromagnetic shower, composed of gammas, electrons and positrons. The dominant processes in electromagnetic showers are pair production for photons and bremsstrahlung for electrons and positrons [12]. Since the typical interaction length of these processes (the "radiation lenght") is much smaller than the typical hadronic interaction length, electromagnetic showers are usually absorbed in the upper layers of the atmosphere. The electromagnetic component of the shower is called the "soft component" because of its rapid development. Charged pions

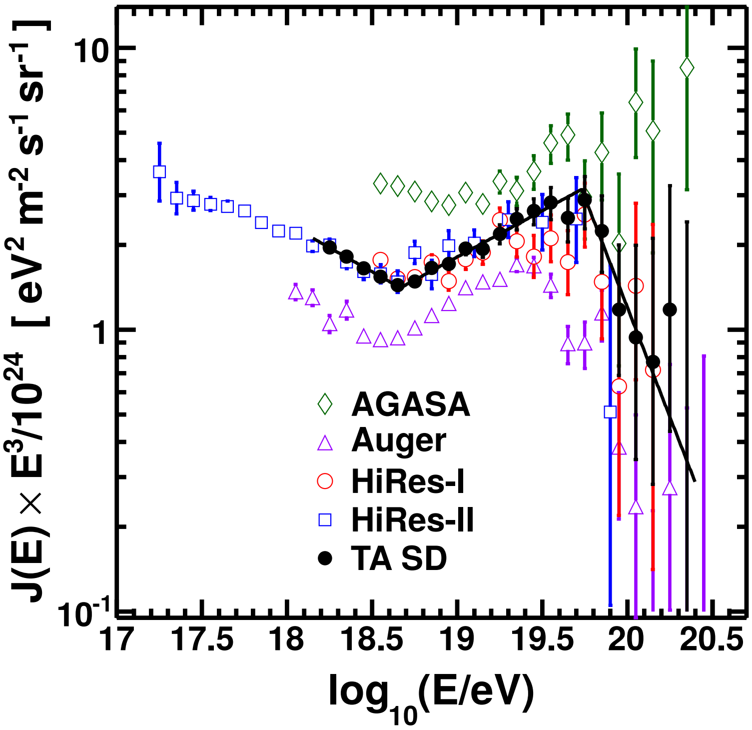

Figure 1.3: Cosmic rays flux multiplied by E^3 measured by several experiments. All experiments (except AGASA) measured a cutoff around $10^{19.5} \div 10^{20}$ eV [11].

can interact with the atmospheric nuclei or decay into muons and neutrinos ($\pi^- \rightarrow \mu^- + \bar{\nu_\mu}$, $\pi^+ \rightarrow \mu^+ + \nu_\mu$). The probability for these processes to happen depends on the energy of the pion because of the relativistic time dilation which increases the mean lifetime of the particle in the reference frame of the atmosphere. Most of the pions with an energy $\sim$ 1 GeV decay without interacting, while nuclear reactions with nuclei of the atmosphere became important with energies above $\sim$ 100 GeV [1]. Muons produced from $\pi^\pm$ decays can in turn decay into electrons and neutrinos ($\mu^- \rightarrow e^- + \bar{\nu_e} + \nu_\mu$, $\mu^+ \rightarrow e^+ + \nu_e + \bar{\nu_\mu}$). Most of the muons with energy up to $\sim$ 1 GeV decay in the atmosphere, while muons with an higher energy can reach the Earth surface. The muon component of the shower is called “hard component” because of its deep penetrating capability. A schematic representation of an air-shower is represented in figure 1.4.

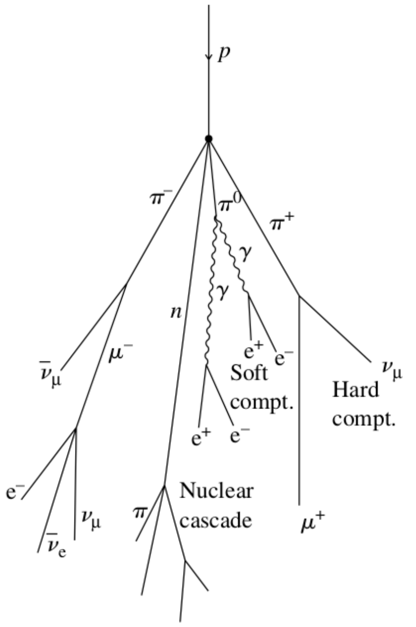

Figure 1.4: Schematic representation of an air-shower indicating the different components of the shower.

The techniques used to detect secondary cosmic rays with ground-based experiments are mainly two:

- Measure charged particles hitting the Earth surface using an array of detectors distributed over a large area and operating in coincidence. By measuring the difference between the arrival time of particles detected in different surface detectors it is possible to reconstruct the arrival direction of the primary cosmic ray which generated the shower. The Pierre Auger Observatory, for example, uses 1600 stations of detectors distributed over a 3000 km^2 area [13]. Each station contains a water Cherenkov detector readout by photomultipliers. The Telescope Array experiment uses instead 507 detector units distributed over an area of 700 km^2 [14]. Each unit is composed of two layers of plastic scintillators.
- Detect the fluorescence and Cherenkov light emitted by the interaction of the secondary cosmic rays with the atmosphere using telescopes and photomultipliers. Cherenkov light is emitted in a narrow angle with respect to the trajectory of the particle and typically arrives to the ground around $\sim$ 100 m from the barycentre of the shower. Fluorescence light is instead emitted isotropically, so it is possible to detect

air-showers several kilometres far from the detector and thus increasing the detector acceptance. Both Auger and Telescope Array experiments are provided with fluorescence light detectors.

Due to the big acceptance of these experiments it is possible to detect the most energetic cosmic rays despite their very low flux. The drawback of this approach is that to derive the energy and type of the primary cosmic ray from the measured parameters of the secondary particles shower, detailed Monte Carlo simulations of the development of the air-shower with accurate hadronic interaction models are needed.

1.3 Hadronic interaction models

In order to obtain cosmic rays astrophysical parameters like energy spectrum and mass composition, Monte Carlo simulations must be performed to estimate the relation from the observable parameters of air-showers and the characteristics of the primary particle. Since most of the energy flow in an air-shower is concentrated in the very forward region, hadronic interaction models implemented in simulations must give a precise estimation of the very forward particles production in a high energy collision between a cosmic ray and the atmosphere.

Most of the particles produced in the forward region are generated in soft QCD processes, which are processes with a low momentum transfer ($<$ 1 GeV/c). Since a perturbative approach cannot be used in soft processes, several phenomenological models based on the Gribov-Regge theory [15, 16] have been proposed. Experimental data are fundamental for the tuning of these models because they can give information about the forward secondary particles produced in high energy collisions. Since particle colliders cannot reach the energies of the most energetic cosmic rays, the models have to be extrapolated at very high energies, leading to a big systematic uncertainty when estimating astrophysical parameters of the primary particle. The Large Hadron Collider (LHC) provides the highest energy proton-proton collisions with a centre of mass energy of 13 TeV, which corresponds to a 0.9×10^{17} eV cosmic ray incident on a fixed target. Even if there are not models tuned using LHC data at $\sqrt{s} = 13$ TeV, LHC data obtained in collisions at $\sqrt{s} = 7$ TeV, corresponding to a 2.6×10^{16} eV cosmic ray incident on a fixed target, were used for the tuning of some models.

In case of the energy measurement the model dependence is not critical because most of the visible energy deposit of the air-shower comes from the electromagnetic component, whose development is well understood. About 80% of the total energy of the shower is transferred to the electromagnetic component in less than five nuclear interactions [17]. The mean depth of the air-shower where the maximum number of particles is present (X_{max}) is a parameter sensitive to the the mass composition of cosmic rays. The relation between the energy of the primary cosmic ray and X_{max} measured by several experiments compared with prediction of Monte Carlo simulations before the tuning with LHC data at $\sqrt{s} = 7$ TeV is shown in figure 1.5. The

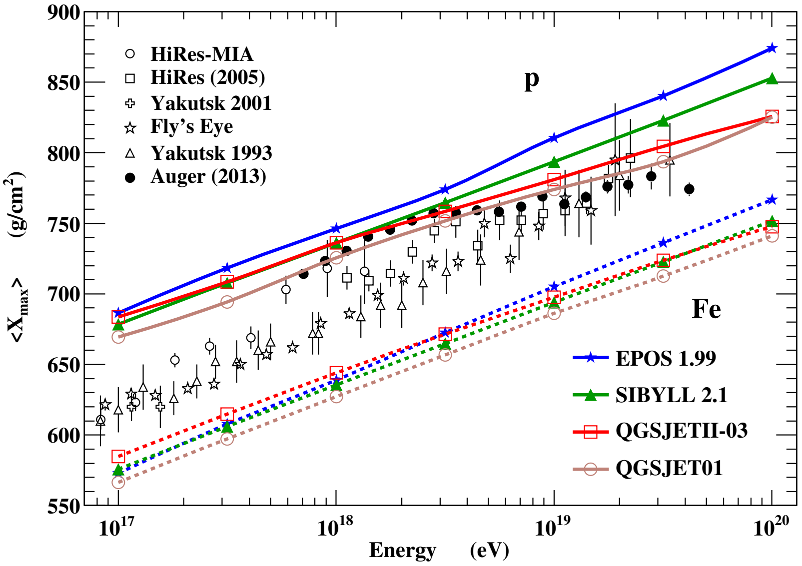

Figure 1.5: Relation between X_{max} and the primary energy measured by several experiments compared with the predictions of different hadronic interaction models before the tuning using LHC data at $\sqrt{s} = 7$ TeV [17, 18]. The predicted relations for proton primaries are shown with solid lines, while they are represented as dashed lines for iron primaries. Black points indicate measured data.

different predictions of models lead to a big systematic uncertainty in the interpretation of the data about the relative abundance of proton and iron nuclei in the primary cosmic rays. Moreover, also the slope of the X_{max} function is not consistent between different models making very difficult to interpret changes of the slope (i.e., changes of the composition) in data.

Figure 1.6 shows the prediction of X_{max} as a function of energy of models tuned with LHC data at $\sqrt{s} = 7$ TeV. After tuning, the discrepancy between the models was decreased, in particular at very high energies, and also the slope of the X_{max} function is consistent between the tuned models. Also the number of muons observed at ground level can be used to derive information

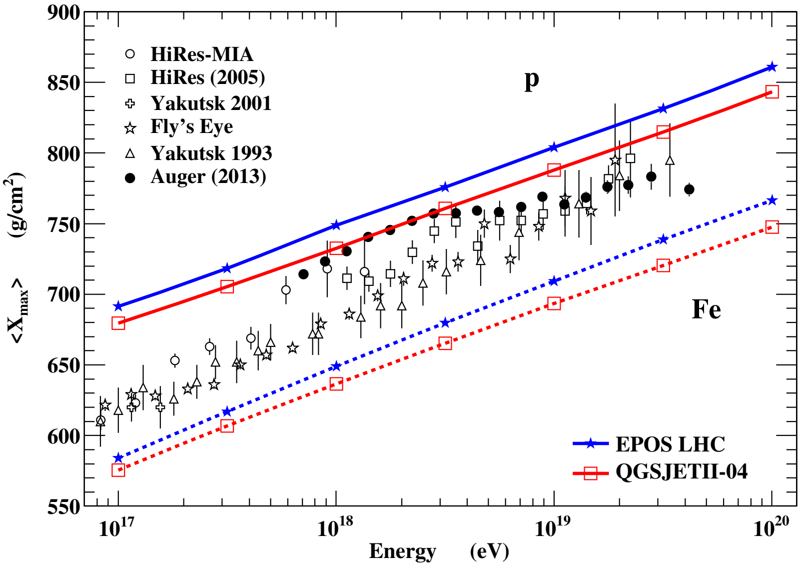

Figure 1.6: Relation between X_{max} and the primary energy measured by several experiments compared with the predictions of two hadronic interaction models tuned with LHC data at $\sqrt{s} = 7$ TeV [17,18]. The predicted relations for proton primaries are shown with solid lines, while they are represented as dashed lines for iron primaries. Black points indicate measured data.

about the mass composition of primaries. Figure 1.7 shows the relation between the flux of muons at ground and the energy of the primary cosmic ray predicted by hadronic interaction models before and after the tuning with LHC data, respectively. Before the tuning it was nearly impossible to derive an information about the mass composition due to the overlap of the proton and iron functions of different models, while after the tuning the situation is really improved.

The improvement of the models after the tuning demonstrates the importance of accelerator experiments for the development of hadronic interaction models used to simulate cosmic rays induced air-showers. The LHCf experiment fits in this context since its purpose is to measure the very forward spectrum of neutral particles produced at LHC for the tuning of hadronic interaction models. The particular position of the experiment (as described in the next chapter) allows LHCf measuring forward particles produced up to zero-degree: it is the only experiment so far which can do precise measurements in the very forward region at the high energies that can be reached at the LHC accelerator. LHCf already collected data with proton-proton

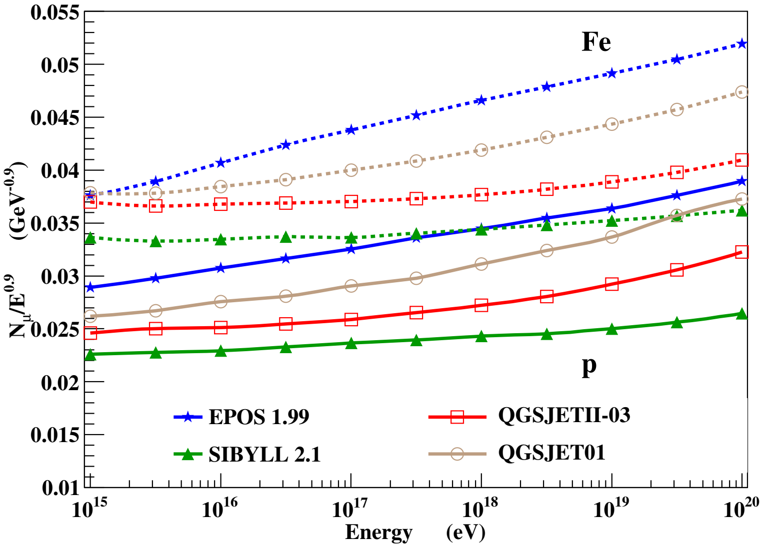

(a) Before tuning

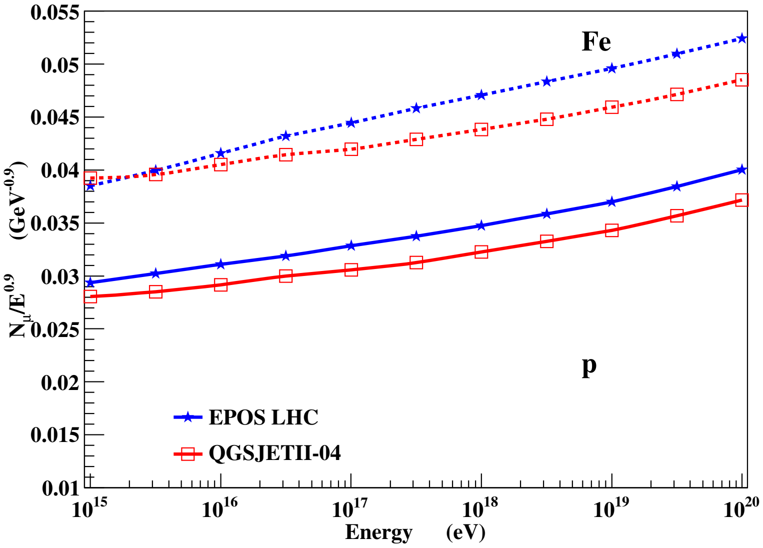

(b) After tuning

Figure 1.7: Prediction of the muon flux (divided by $E^{0.9}$) at ground level as a function of the primary energy from hadronic interaction models before and after the tuning with LHC data at $\sqrt{s} = 7$ TeV. The predicted relations for proton primaries are shown with solid lines, while they are represented as dashed lines for iron primaries.

collisions at $\sqrt{s} = 0.9, 2.76, 7, 13$ TeV and with proton-lead collisions at $\sqrt{s_{NN}} = 5.02, 8.16$ TeV. The photon energy spectrum in proton-proton collisions at $\sqrt{s} = 0.9$ and 7 TeV, the neutron energy spectrum in proton proton collisions at $\sqrt{s} = 7$ TeV, and the π^0 transverse and longitudinal momentum spectra in proton proton collisions at $\sqrt{s} = 2.76, 7$ and in proton-lead collisions at $\sqrt{s_{NN}} = 5.02$ TeV have already been published [19–24].

The purpose of this work is to derive the energy spectrum of photons produced in proton-proton collisions at $\sqrt{s} = 13$ TeV using the Arm2 detector of the LHCf experiment and to compare it with the predictions of Monte Carlo generators commonly used for the simulation of air-showers. The LHCf measurements at $\sqrt{s} = 7$ TeV indicate that none of the models lies within the errors of data over the entire energy range [19]. However, data lie between the predictions of all models. The upgrade of the centre of mass energy from 7 TeV to 13 TeV extends the equivalent cosmic ray energy from 2.6×10^{16} eV to 9×10^{16} eV, which is the maximum available energy that can be reached with an accelerator experiment nowadays. Furthermore, the coverage in the transverse momentum (P_T) phase space of secondary particles produced in collisions was extended: in the acceptance region of the LHCf experiment used in this analysis the maximum detectable P_T was increased from ~ 1.0 GeV/c to ~ 1.9 GeV/c.

In the 7 TeV analysis the measured photon energy spectrum was compared with the spectra predicted by Monte Carlo simulations which also implemented the effect of the detector response. In order to obtain a measured energy spectrum which can be directly compared with the prediction of hadronic interaction models, in the 13 TeV analysis described in this work the data were corrected for the detector response using the unfolding technique, as will be explained in section 5.5.

The LHCf experiment and the necessary upgrade of the detectors to operate at $\sqrt{s} = 13$ TeV will be described in chapter 2. In chapter 3 the study of the detector performance with Monte Carlo simulations will be presented. The beam test performed at the CERN Super Proton Synchrotron for the calibration of the detectors will be discussed in chapter 4. The analysis procedure to derive the photon energy spectrum measured at LHC in proton-proton collisions at $\sqrt{s} = 13$ TeV will be explained in section 5. The photon spectrum measured by the Arm2 detector will be then compared with the predictions of several hadronic interaction models.

Chapter 2

The LHCf experiment at the LHC

2.1 The Large Hadron Collider

The Large Hadron Collider (LHC) [25] is the largest particle accelerator in the world. LHC is located at CERN and it uses the 27 km long tunnel that previously contained the Large Electron Positron collider (LEP). The 27 km long tunnel houses a collider composed of two parallel circular beam pipes. LHC can provide proton-proton, proton-lead and lead-lead collisions. The possibility to provide collisions with lighter ions in the future is under consideration. 1232 superconductive dipole magnets are installed to guide each beam along the ring and 392 quadrupoles are used to focus it. The design luminosity[1] was 10^{34} cm^{-2} s^{-1} with a centre of mass energy of 14 TeV. In order to achieve this high collision energy, the magnetic dipoles must operate at a temperature of 1.9 K in superfluid helium to provide a 8.33 T magnetic field (for the maximum beam energy of 7 TeV). Four interaction points (IP) are provided for four big experiments: IP1 for ATLAS, IP2 for ALICE, IP5 for CMS and IP8 for LHCb. Also three smaller experiments are installed at LHC: LHCf at IP1, TOTEM at IP5 and MoEDAL at IP8. The position of the main four LHC experiments along the ring is shown in figure 2.1.

Following the incident of 2008, when an electrical connection fault between a dipole and a quadrupole caused a mechanical damage and a release of the helium used to cool the magnets, the center of mass energy and luminosity were decreased to 7 TeV and 7.7×10^{33} cm^{-2} s^{-1} (peak value), respectively, during the so called Run 1 of LHC which was started at the end of 2009 and was concluded at the beginning of 2013 [26]. During 2012 the

---

[1] The luminosity L is defined as $L = \frac{1}{\sigma}\frac{dN}{dt}$, where $\frac{dN}{dt}$ is the rate of observation of a process and σ is its cross section.

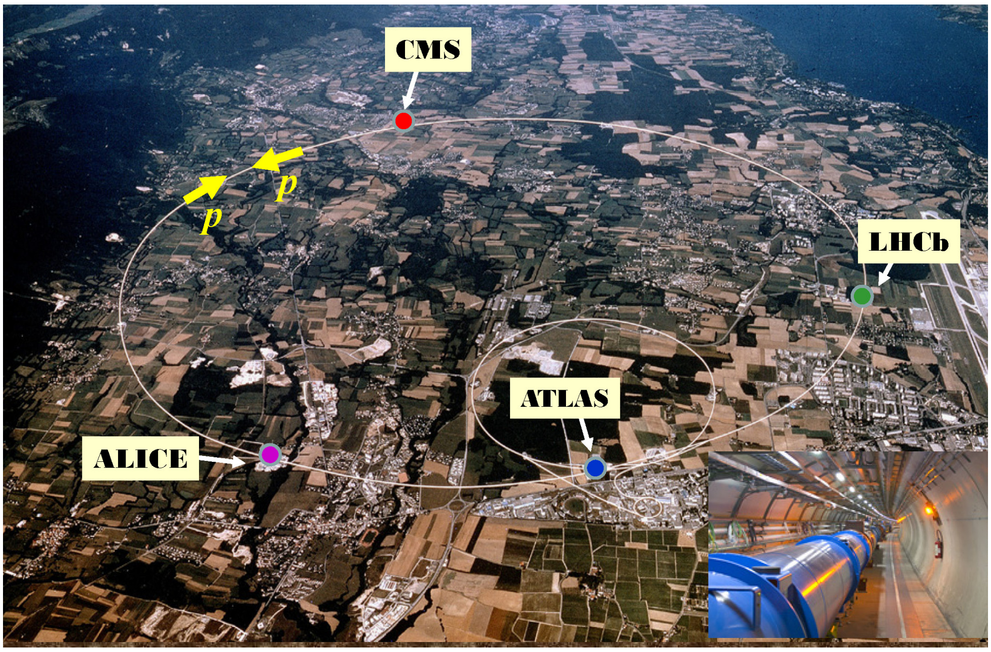

Figure 2.1: Position of the main LHC experiments along the 27 km long tunnel of the accelerator. LHCf experiment is located near the ATLAS experiment.

centre of mass energy was increased to 8 TeV. LHC operation were stopped for two years (Long Shutdown 1, or LS1) for the upgrade of magnet interconnections to solve the problem that occurred in 2008 and to let each beam to reach an energy of 6.5 TeV. The Run 2 of LHC started in 2015 and produced for the first time proton-proton collisions at the record centre of mass energy of 13 TeV on May 25, 2015.

2.2 The LHCf detector

The LHC-forward experiment (LHCf) is located near the interaction point 1 (IP1) of LHC. LHCf is composed of two independent detectors, called Arm1 and Arm2, located 140 meters away from the IP1 on opposite directions along the beam line Each detector is located in the instrumentation slot of the Target Absorber Neutral (TAN) which is designed to absorb neutral particles emitted in the very forward direction, not bended by the dipole magnets. The TAN is located where the beam pipe coming from the interaction point is splitted into the two separate pipes of the colliding beams, as shown in figure 2.2. This particular position allows LHCf measuring particles emitted

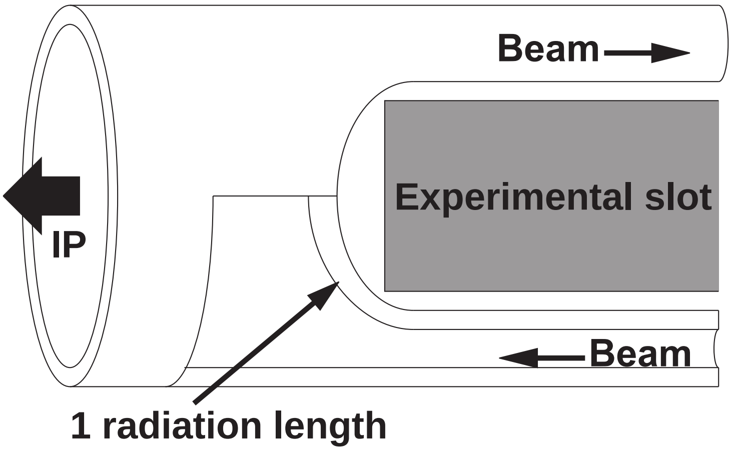

Figure 2.2: Schematic view of the TAN area where the LHCf experiment is located. The detector is placed into the experimental slot.

at zero-degree with respect to the beam axis. The energy flow of secondary particles peaks in the very forward region around pseudorapidity[2] $\eta \sim 9$ (corresponding to a ~ 0.25 mrad angle with respect to the beam) in case of a $\sqrt{s} = 14$ TeV collision, as shown in figure 2.3. Since the energy flux of secondary particles is very important for the study of air showers, measurements in the very forward region are very useful for the understanding of shower development.

A dipole magnet (called D1) is placed between IP1 and the TAN region to deviate the proton beam coming from the interaction point into the appropriate beam pipe of the ring and vice-versa for the other colliding beam. Charged particles produced in the collision are deflected by D1 magnet while neutral particles, mostly neutrons and photons, are not affected from it and can be detected by the LHCf detector.

Each LHCf detector is composed of two sampling and position sensitive calorimeter, which will be called "towers" hereafter. During the Run 1 of LHC each calorimeter used 17 tungsten layers as absorber material and 16 platic scintillators (EJ-260) as active layers to sample particle-induced showers. The depth of the calorimeters was 44 radiation lengths (X_0) corresponding to 1.6 hadronic interaction lengths (λ_I). The first 11 layers and the last one had a thickness of 7 mm, while layers from the 12th to the 16th were 14

---

[2] The pseudorapidity is defined as $\eta \equiv -\ln\left[\tan\left(\frac{\theta}{2}\right)\right]$, where θ is the angle between the particle and the beam axis.

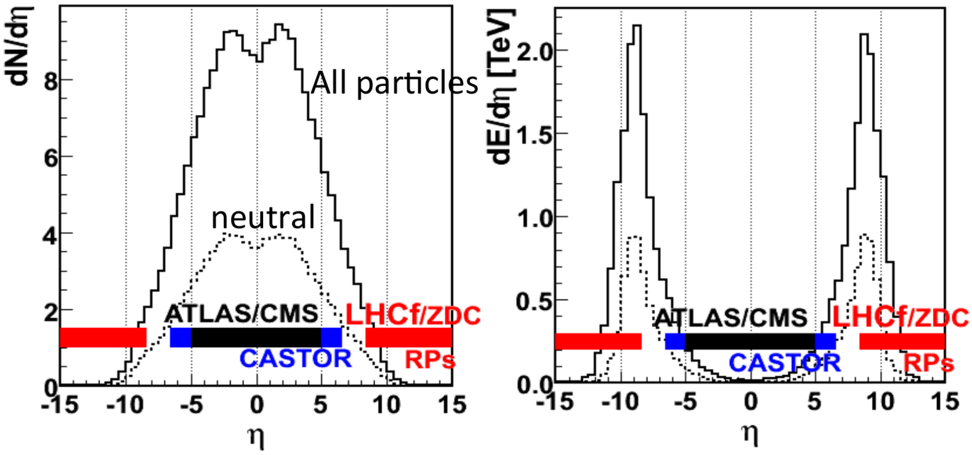

Figure 2.3: Multiplicity (left picture) and energy flow (right picture) of secondary particles produced in Monte Carlo simulations of proton-proton collisions at $\sqrt{s}$ = 14 TeV. Solid line refers to all particles while dashed line refers to only neutral particles. The pseudorapidity coverages of some LHC experiments are shown as coloured bands.

mm thick. The sampling step of the latter layers was greater than the first layers because they were dedicated to the measurement of hadronic showers whose interaction length is much greater than that of electromagnetic showers (which are contained mostly in the first layers). The thickness of plastic scintillators was 3 mm for all layers. The light signal from the scintillator was transported through a quartz light guide and read with a photomultiplier tube (PMT, HAMAMATSU R7400). The transverse size of calorimeters was 20 mm × 20 mm and 40 mm × 40 mm for the two calorimeters of Arm1 while it was 25 mm × 25 mm and 32 mm × 32 mm for Arm2. The smaller calorimeter of each detector will be called “small tower” hereafter, while the other one will be called “large tower”. Apart from transverse area, the main difference between Arm1 and Arm2 was about the position sensitive layers: Arm1 used 4 planes of plastic scintillating fibres (SciFi) with a 1 mm pitch, while Arm2 used 4 planes of silicon microstrip detectors with a 160 μm pitch. More details about the silicon detectors can be found in [27]. Each position sentitive plane was composed of two position detectors, one for the measurement of X coordinate and the other to measure Y coordinate. The longitudinal structure of the towers is shown in figure 2.4. Energy resolution was 5% for photons and 40% for neutrons, while position resolution for electromagnetic showers was 200 μm and 40 μm for Arm1 and Arm2,

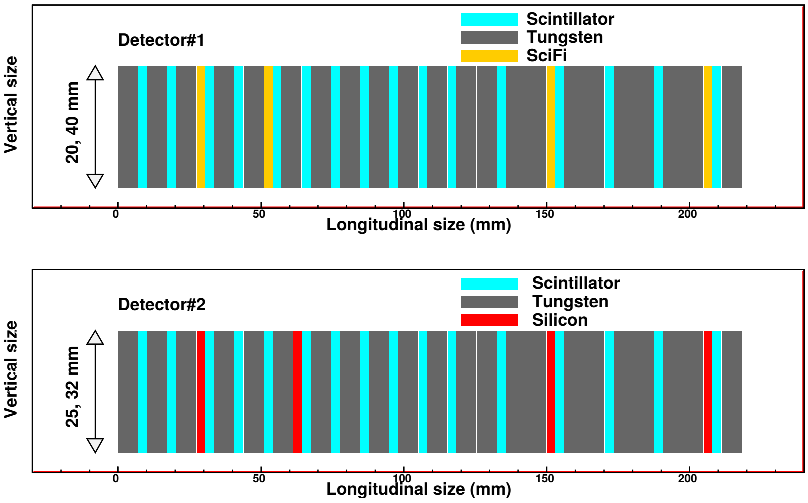

Figure 2.4: Longitudinal structure of Arm1 (upper picture) and Arm2 (lower picture). Grey, cyan, yellow and red layers represent tungsten, scintillator, SciFi and silicon layers, respectively. The upstream side of detectors is on the left of the picture.

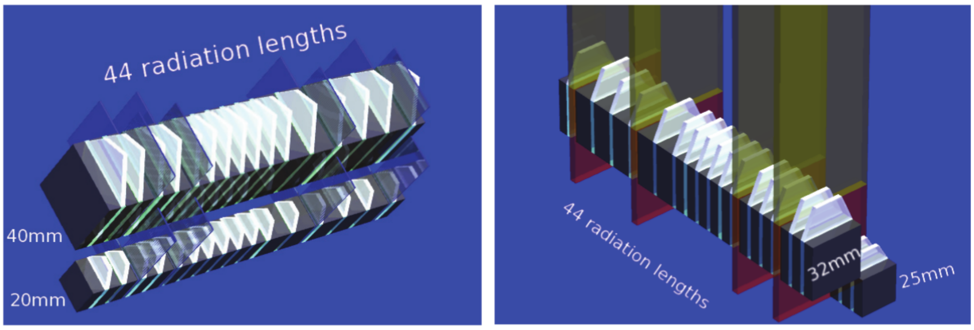

Figure 2.5: Schematic representation of Arm1 (left picture) and Arm2 (right picture).

respectively. The detectors were upgraded before Run 2 operation but the structure of the calorimeters is basically the same described above. Details about the upgrade are described in section 2.3.

The pseudorapidity coverage of the small tower is $\eta > 9.6$, so it can detect zero-degree particles, while the large tower covers the range $8.4 < \eta < 9.4$. The two-towers structure of both detectors gives the possibility to detect separately two photons from a π^0 decay: in this way there is the possibility to check the absolute energy scale by measuring the π^0-mass peak in the two-photon invariant mass distribution and to measure kinematic parameters of π^0s produced in collisions.

This work describes the analysis of Arm2 data recorded during the Run2 of LHC in proton-proton collisions. Therefore, everything in the next chapters will refer to the Arm2 detector if not specified otherwise.

2.3 Upgrade of the detector for 13 TeV operation

Before the data taking in Run 2 operation several part of the detectors were upgraded:

1. The plastic scintillators were replaced by Gd_2SiO_5 (GSO) scintillators with 1 mm thickness, because of their higher radiation hardness. The estimated absorbed dose was of the order of 300 Gy for the expected ~ 10 nb^{-1} of integrated luminosity at $\sqrt{s} = 13$ TeV. GSO can maintain its light yield up to 10^6 Gy [28], while plastic scintillators start experiencing a degradation at about $\sim 10^2$ Gy. Also the scintillating fibres of Arm1 were replaced by GSO bars with 1 mm × 1 mm cross section and with the same lenght of the plastic ones [29].

2. The longitudinal position of silicon detectors in Arm2 was changed in order to better sample the longitudinal profile of the showers inside the calorimeter and to give the possibility in the future to reconstruct the energy of the particle from the energy deposit in silicon, in addition to the measurement with the scintillators [30]. In the last two planes the X and Y views were separated one from each other as shown in figure 2.6.

3. All the silicon detectors in Arm2 were replaced by new ones. In the new silicon detectors a different bonding scheme for the microstrips was used to reduce the collected signal charge to about 50% of the signal in the old configuration. The distance between two strips was 80 μm but only half of the strips were read while the others were left unconnected (“floating”). However, the energy deposit in floating strips was shared between the two nearest read strips by capacitive coupling. In the upgraded detector the floating strings were bonded to ground instead of being left floating, so the energy deposit in these strips is

lost. The new bonding scheme allows the silicon readout electronics to saturate at higher energies with respect to the old configuration.

4. The large tower of Arm2 was moved on the opposite side (toward the inner part of the LHC ring) to reduce the background from high energy protons in diffractive interactions, which are not properly deviated by the D1 dipole magnet.

The longitudinal configuration of the upgraded Arm2 detector is shown in figure 2.6. Photos of the upgraded detectors are shown in figures 2.7 and 2.8.

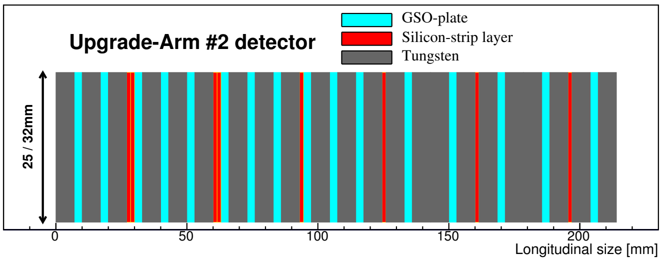

Figure 2.6: Longitudinal structure of Arm2 after the upgrade before Run 2 operation. Grey, cyan and red layers represent tungsten, GSO scintillator and silicon layers, respectively. The upstream side of detector is on the left of the picture.

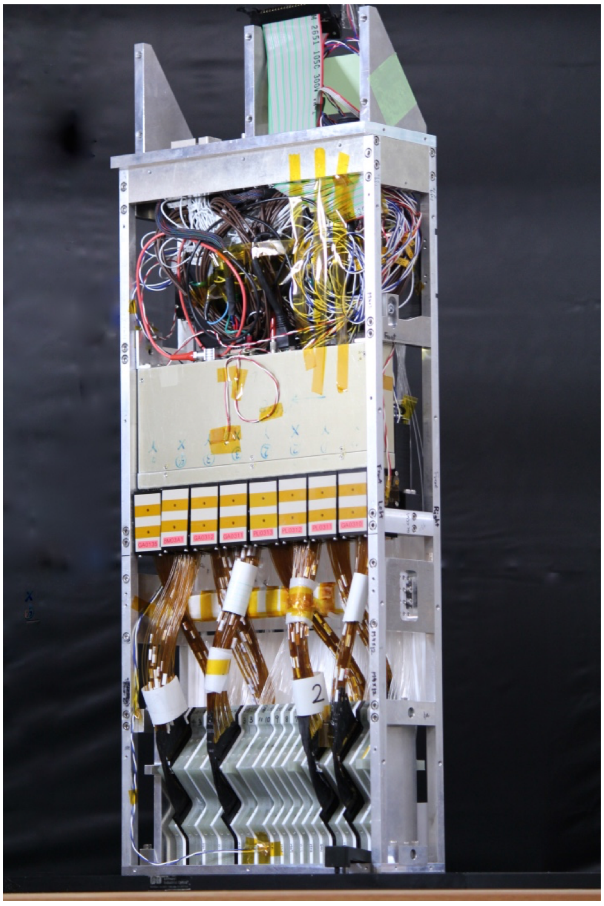

Figure 2.7: Photo of the upgraded Arm1 detector. The two calorimeters are positioned in the bottom of the pictures.

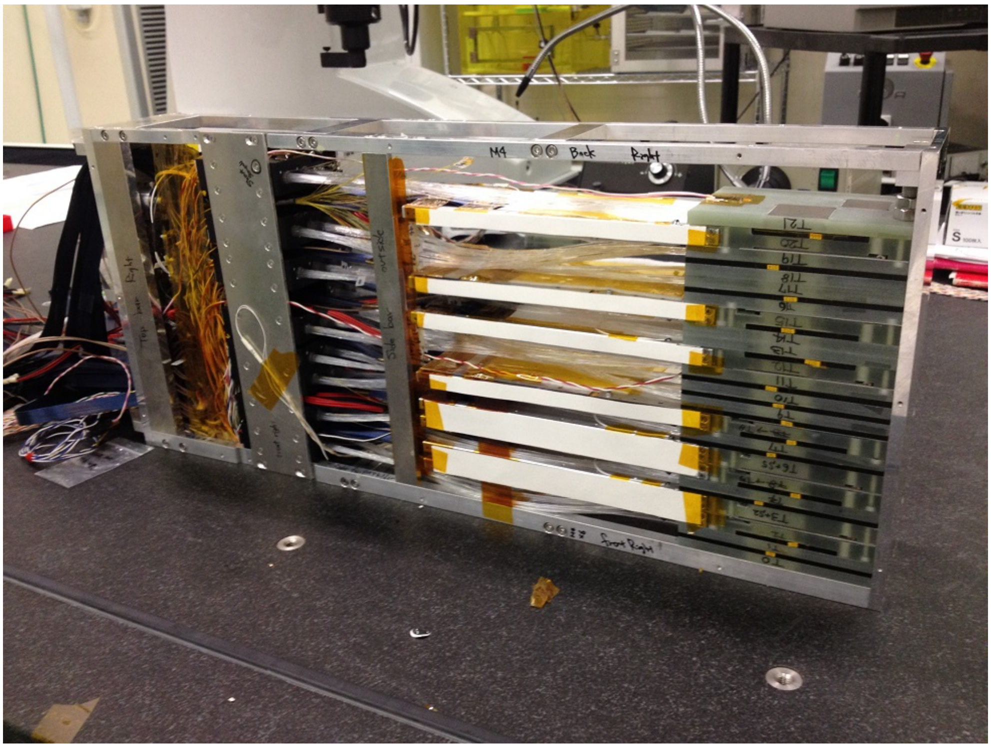

Figure 2.8: Photo of the upgraded Arm2 detector (lying sideways). The two calorimeters are positioned on the right of the picture.

Chapter 3

Performance study with simulations

Results from Monte Carlo simulations were used to study the performance of the system, estimate corrections for detector effects and to calibrate the calorimeters (together with data, as will be described in chapter 4). Predictions of several simulation models will be compared with measured data at the end of section 5. The simulation of an event recorded by LHCf can be divided in 3 steps:

1. Simulation of the collision between two protons (generator).
2. Propagation of secondary particles from the interaction point to the TAN region. The decay probability of secondaries was also considered and daughter particles were propagated as well.
3. Simulation of the interaction between collision products and the detector.

In the first step, one of several widely used models for air showers simulations was chosen to simulate the interaction between two protons at $\sqrt{s} = 13$ TeV: DPMJET 3.06 [31,32], QGSJET II-04 [33], SIBYLL 2.1 [34], EPOS-LHC [35] and PYTHIA 8.212 [36, 37]. QGSJET II-04 and EPOS-LHC were the only two model tuned using experimental results in the central rapidity region obtained by LHC experiments during Run 1. In PYTHIA 8.212 only soft inelastic processes were activated and the default parameters set was used. In the second and third steps, COSMOS 7.645 and EPICS 9.165 Monte Carlo simulation codes [38,39] were used to simulate the interaction of particles with the beam pipe and with the detector. The models available in COSMOS and EPICS for the interaction were DPMJET 3.04 and QGSJET II-04. DPMJET

3.04 was used to simulate the interaction inside the detector because it gave the best agreement with data using a 350 GeV proton beam [40]. However, in case of electromagnetic showers there were no difference between models because they only differ in the treatment of hadronic interactions. Version number of models will be omitted hereafter if not strictly necessary.

A sample of 10^8 inelastic collisions events were simulated with the QGSJET generator and propagated to the detector. This sample has been used as a template for the particle identification correction and to generate the response matrix of the detector for the unfolding, as will be explained in chapter 5. Another sample of 5×10^7 inelastic collisions were generated using EPOS model and collision products propagated in order to estimate the systematic uncertainties related to the choice of the generator model, as will be described in section 5.6.5.

In this chapter some studies of the detector behaviour will be described: the relation between the total energy deposit and the energy of the incident particle will be described in section 3.1, while the study of the position dependence of the signal in the calorimeters will be discussed in section 3.2. Since these studies are related only to the detector, only the step 3 of the simulation process was performed, generating particles directly in front of the detector.

3.1 Energy conversion function

In order to measure the energy of the detected particle, the relation between the total energy deposit measured in sampling scintillator layers and the energy of the incident particle was determined. The total energy deposit were defined as the sum of the energy deposit of layers from 2nd to 13th and it will be called “Sum-dE” hereafter. The energy deposit of layers from 12th to 16th was multiplied by a factor 2 because the sampling step is doubled with respect to previous layers. The first layer was excluded from the sum to avoid the contribution from low energy background particles. The contribution of layers from 14th to 16th for electromagnetic showers was negligible, therefore they were eliminated from the summation to avoid including a contribution mainly from noise fluctuations.

To study the relation between the Sum-dE and the energy of the incident particle, Monte Carlo simulations of photons incident at the centre of the towers were performed. The photons were generated before the point where the beam pipe splits into two separate pipes, about one meter upstream of the detector. So, also the interaction with the wall of the beam pipe just before the calorimeter was simulated. In each set of simulated events the photon energy was fixed. Seven simulation sets were generated for each tower with seven different energies: 100, 200, 500, 1000, 2000, 3000 and 6000 GeV. In every set 10^4 events were generated. The mean of the Sum-dE were calculated for each energy and it was plotted as a function of the primary energy. The error associated to the mean was $\sigma/\sqrt{N}$, where σ is the standard deviation of the Sum-dE distribution and N is the number of simulated events. The relation between Sum-dE and energy was fitted with a 2nd order polynomial function:

$$\text{Sum-dE} = p_o + p_1 \cdot E + p_2 \cdot E^2 \tag{3.1}$$

where E is the energy of the photon and p_0, p_1 and p_2 are free parameters. The 2nd order term was included to eventually consider deviations from linearity. The Sum-dE vs energy plots and the fit functions are shown in figures 3.1 and 3.2 for small and large tower, respectively. From the 2nd order term there is only a very small contribution to the total Sum-dE (less than 0.4% over all the energy range), so the relation can be considered almost linear. The negative constant term ($p_0 \sim -100$ MeV) indicates that there is a threshold for the energy E of about $2 \div 3$ GeV before measuring a non negligible Sum-dE. The 2nd scintillator layer (the first used in Sum-dE) is placed after 4 X_0 of tungsten and in addition there is 1 X_0 of the beam pipe wall to be considered, so the particle shower must have a depth of at

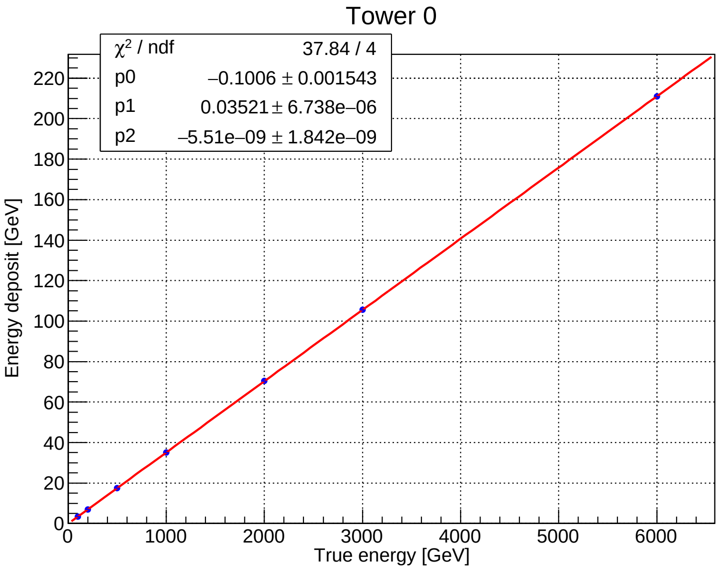

Figure 3.1: Sum-dE as a function of energy for photons incident at the centre of the small tower. The fit function is drawn as a red line.

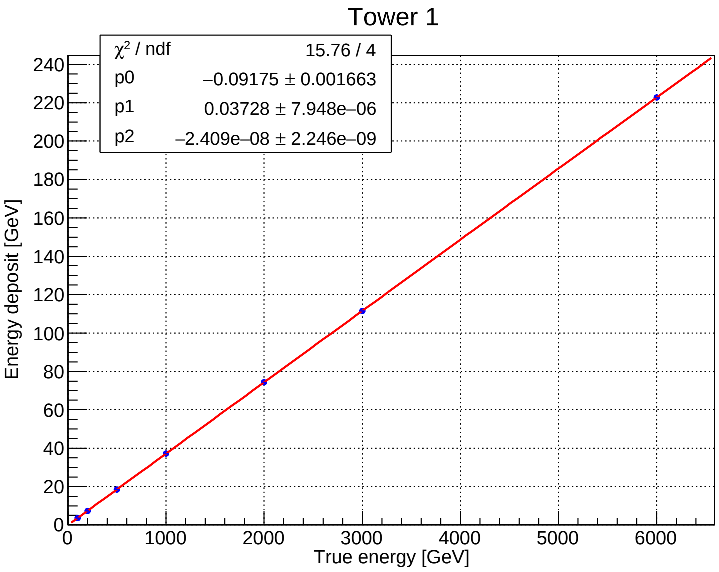

Figure 3.2: Sum-dE as a function of energy for photons incident at the centre of the small tower. The fit function is drawn as a red line.

least 5 X_0 to be detected. Using the Rossi-Heitler model for electromagnetic showers [41, 42], the depth of the shower maximum is approximately $5.5 \div 6$ X_0 for a $2 \div 3$ GeV photon. Even if not consistent, which is understandable since the threshold was extrapolated from results at $E > 100$ GeV and the Rossi-Heitler model is a basic approximation, this value is of the same order of the predicted depth. Relative residuals of the fit are shown in figures 3.3 and 3.4 for the small and large tower, respectively. Even if the value of the reduced χ^2 of the fit is much greater than 1 ($\sim$ 9 and 4 for small and large tower, respectively), the relative residuals are less than 0.1%. Since it is negligible with respect to the other systematic uncertainties, equation 3.1 was considered an acceptable approximation of the relation between Sum-dE and energy and it was used in the analysis that will be described in chapter 5.

3.2 Position dependence of signal

The energy deposit in the calorimeters strongly depends on the position of the incident particle. There are two effects that are responsable for that dependence: the leakage effect and the light collection efficiency of scintillators. The leakage effect will be described in section 3.2.1, while the light collection

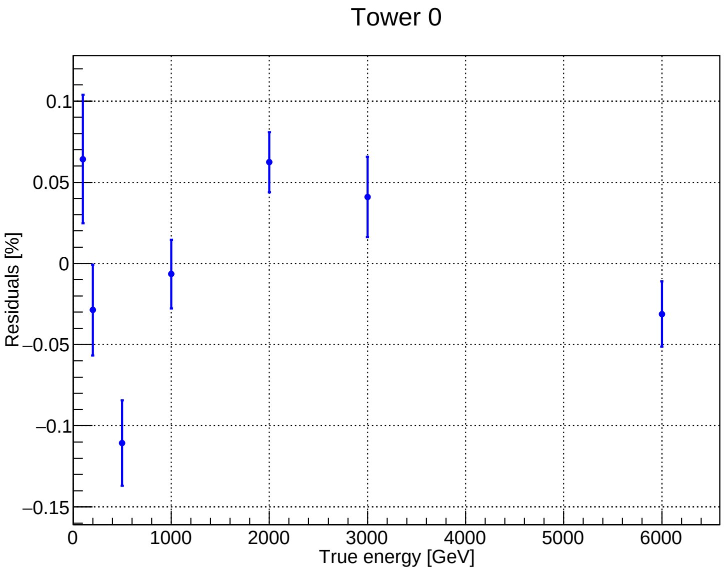

Figure 3.3: Relative residuals of the fit with equation 3.1 of the Sum-dE vs energy plot for the small tower.

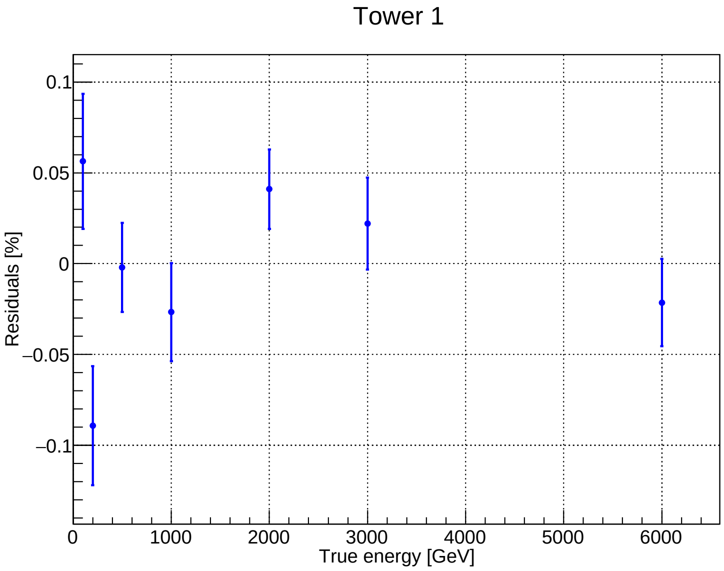

Figure 3.4: Relative residuals of the fit with equation 3.1 of the Sum-dE vs energy plot for the large tower.

efficiency will be discussed in section 3.2.2. The description of the correction for these effects will be explained in section 3.2.3.

3.2.1 Leakage effect

When a photon hits one of the towers, a shower of secondary particles is produced inside the detector. The typical width of the shower is given by the Molière radius of the absorber material, which is defined as the radius of the cylinder which contains 90% of the energy deposit of the shower generated from an high energy photon or electron. In case of tungsten, the Molière radius is 0.93 cm. Particles hitting the calorimeter near the edges lose part of the shower outside the detector: as a consequence, the measured energy deposit is less than the one observed with a particle of the same energy hitting the centre of the calorimeter. A two-dimensional map of the mean Sum-dE measured as a function of the transverse coordinates X and Y was generated simulating mono-energetic 500 GeV photons incident uniformly on the surface of each tower. Particles were generated ∼1 meter before the detector, as previously described in section 3.1. The Sum-dE values in each position bin were normalised to the Sum-dE at the centre of the tower. Figures 3.5 and 3.6 show the Sum-dE map for the small and large tower, respectively. Since the leakage effect mainly depends on the shape of the shower developed in the calorimeter, the leakage map is almost independent from the photon energy. Deviations of the map for 100 GeV, 200 Gev, 1 TeV, 2 TeV photon simulations relative to 500 GeV results were found to be of the order of 0.5%.

3.2.2 Light collection efficiency of scintillators

The light emitted in the scintillation process must reach the PMT through the light guide to be detected. The light collection efficiency of a scintillator is defined as the fraction of generated scintillation light that reaches the PMT. It depends on the geometry of scintillator and light guide, on the optical coupling between scintillator, light guide and PMT, and on the reflectiviy of the scintillator coating material. The position dependence of the light collection efficiency was studied using the data of a beam test at the Heavy Ion Medical Accelerator in Chiba (HIMAC) that was done in 2013 with a 290 MeV/n ^{12}C ion beam. Details about the beam test setup can be found in [43]. For each scintillator, a map of the signal recorded by the PMT as a function of the position of the energy deposit were measured with the carbon beam. The light collection efficiency maps measured at the HIMAC are shown in figures 3.7 and 3.8 for the 4th layer of the small tower and for the 5th layer

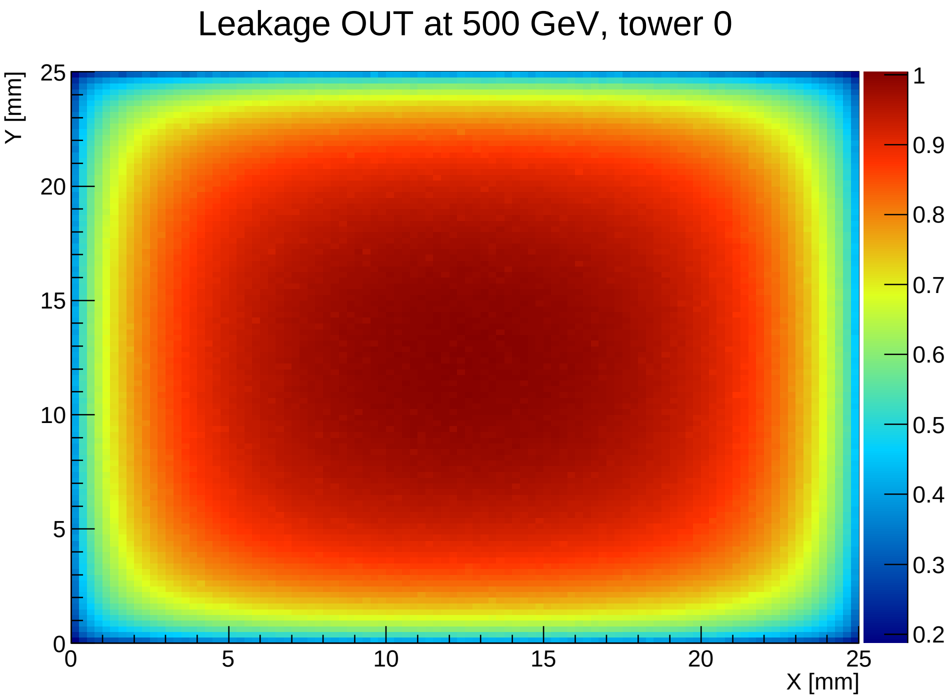

Figure 3.5: Position dependence of the Sum-dE of the small tower, generated with 500 GeV photon uniformly distributed along X and Y axis. Sum-dE values were nomalised to the value at the centre of the calorimeter.

of the large tower, respectively. The maps for the other layers are shown in figures 1 and 2 of the appendix for the small and large tower, respectively.

The efficiency measured at the HIMAC are related to a localised energy deposit, so the associated position dependence for an electromagnetic shower is the convolution of the efficiency map and the transverse profile of the shower. In order to get the position dependence map for an electromagnetic shower, the efficiency map was directly implemented in the simulation: the energy deposit of each particle of the shower in a scintillator was multiplied by the value of the light collection efficiency in that point. The efficiency value was obtained by a linear interpolation of the measurements grid using equation 3.2, where $\epsilon(x, y)$ is the interpolated efficiency at the coordinates (x, y), (x_i, y_j), with i, j = 1 or 2, are the coordinates of the four nearest

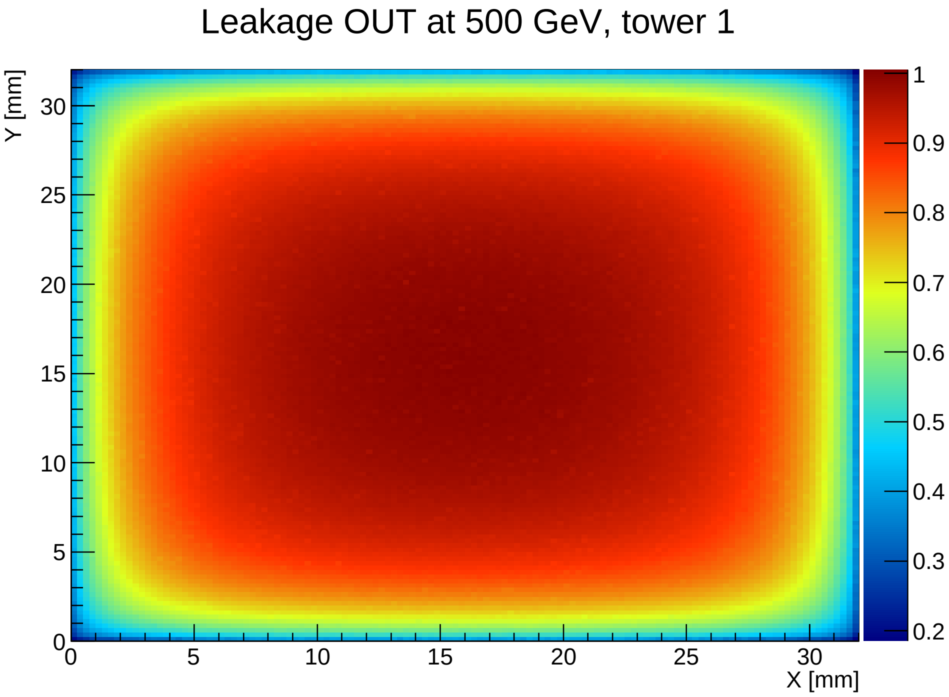

Figure 3.6: Position dependence of the Sum-dE of the large tower, generated with 500 GeV photon uniformly distributed along X and Y axis. Sum-dE values were nomalised to the value at the centre of the calorimeter.

measured points and ϵ_{ij} are the measured efficiencies in (x_i, y_j):

$$\begin{aligned} \epsilon(x,y) = [(x_2 - x_1)(y_2 - y_1)]^{-1} \cdot [\ & \epsilon_{11}(x_2 - x)(y_2 - y) + \\ & \epsilon_{21}(x - x_1)(y_2 - y) + \\ & \epsilon_{12}(x_2 - x)(y - y_1) + \\ & \epsilon_{22}(x - x_1)(y - y_1)\ ] \end{aligned} \tag{3.2}$$

3.2.3 Correction of the position dependence

When analysing data, the energy deposit in each scintillator must be corrected for the above-mentioned leakage and light collection efficiency effects in order to properly reconstruct the energy using equation 3.1, which was obtained with particles incident at the center of the calorimeter. The correction was based on Monte Carlo simulations which implemented also light collection efficiency as described in the previous sections, so it was possible to correct for the non-uniformity of detector response simultaneously for both

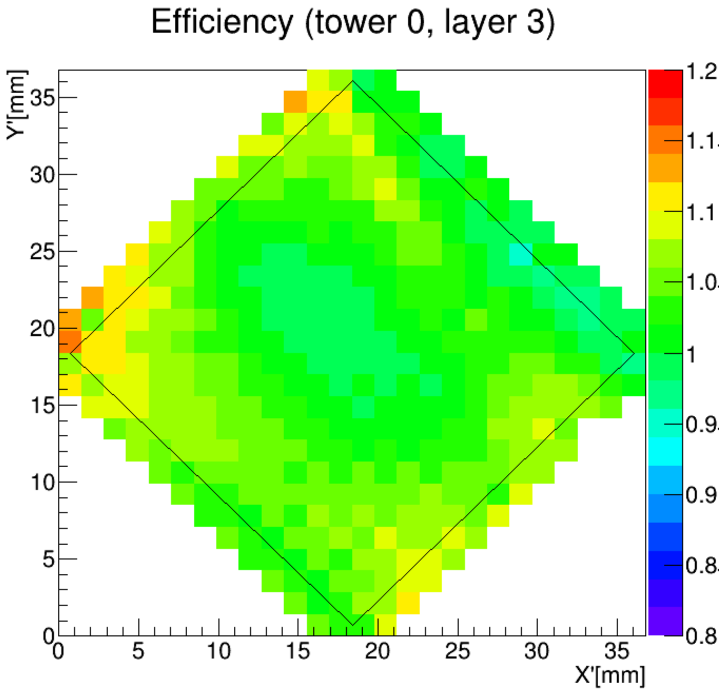

Figure 3.7: Light collection efficiency maps for the 4th scintillator layer of the small tower as a function of transverse position. The color map represents the intensity of the signal recorded by the PMT in that position, normalised to the signal recorded at the center of the scintillator. Since the grid of measurements was rotated by 45 degrees with respect to the scintillator, the map was rotated in the same way. The light guide is located in the upper-left side of the picture.

effects.

A sample of 10^6 and 1.6×10^6 events was simulated for the small and large tower respectively. 500 GeV mono-energetic photons were generated uniformly distributed on the surface of the detector. A two-dimensional map were created for each scintillator layer showing the mean energy deposit as a function of the position of the incident photon, normalised to the energy deposit at the centre. The map was composed of 50×50 and 64×64 bins for the small and large tower, respectively, so the bin size was 0.5 mm for both calorimeters. The correction map for the 4th layer of the small tower and for the 5th layer of the large tower are shown in figures 3.9 and 3.10, respectively. The maps for the other layers are shown in figures 3 and 4 of the appendix for the small and large tower, respectively.

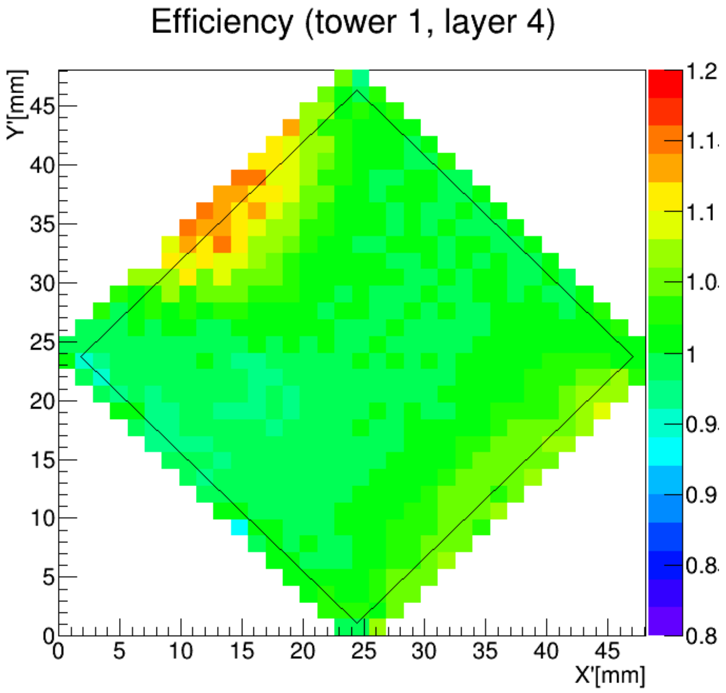

Figure 3.8: Light collection efficiency maps for the 5th scintillator layer of the large tower as a function of transverse position. The color map represents the intensity of the signal recorded by the PMT in that position, normalised to the signal recorded at the center of the scintillator. Since the grid of measurements was rotated by 45 degrees with respect to the scintillator, the map was rotated in the same way. The light guide is located in the upper-left side of the picture.

The correction was applied dividing the energy deposit of each event in the scintillators by the value of the correction map corresponding to the reconstructed position of the incident particle (the method used to reconstruct the position with the silicon detectors will be explained in section 5.2.1). The value of the correction was computed by a linear interpolation of the map, with a formula analogous to equation 3.2. This method for the correction of the non-uniformity of the detector response was used in the analysis described in chapter 5. A test of the correction with beam test data will be discussed in section 4.5.2.

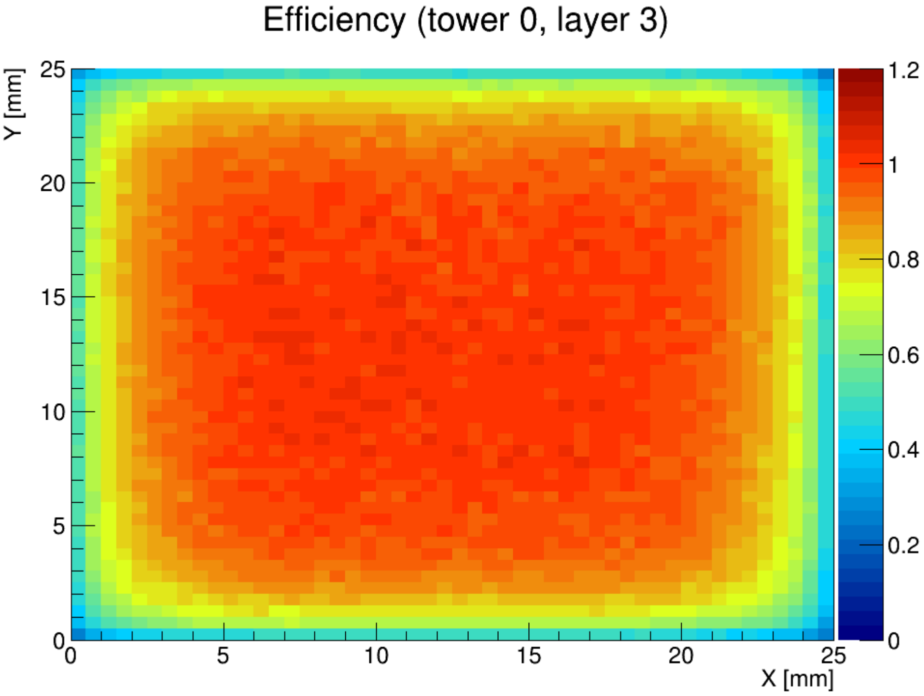

Figure 3.9: Position dependence correction map for the 4th scintillator layer of the small tower generated with a 500 GeV photon Monte Carlo simulation. Both leakage and light collection efficiency effects are implemented in the simulation.

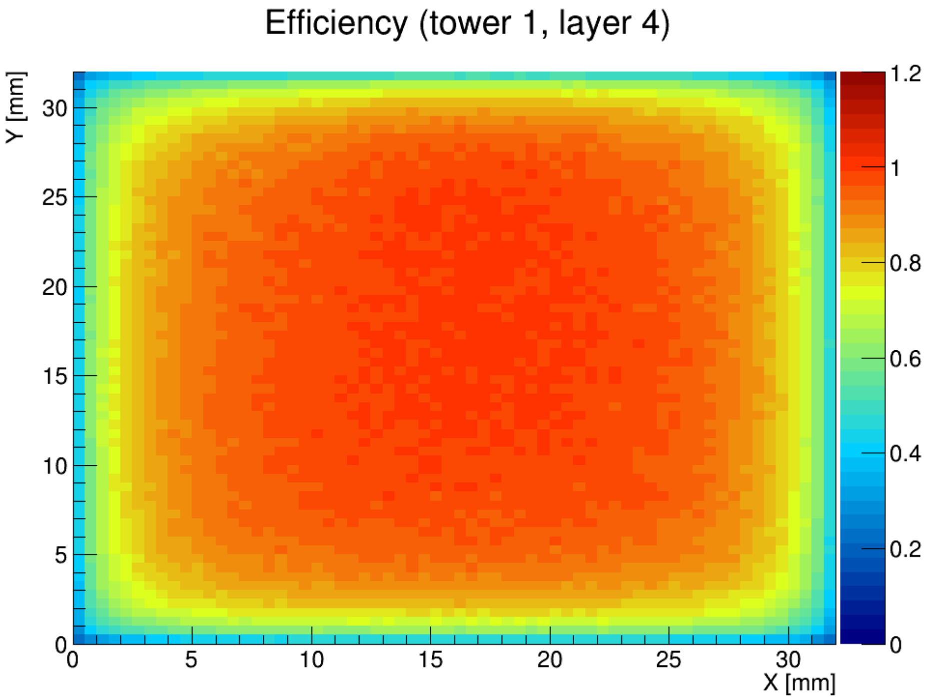

Figure 3.10: Position dependence correction map for the 5th scintillator layer of the large tower generated with a 500 GeV photon Monte Carlo simulation. Both leakage and light collection efficiency effects are implemented in the simulation.

Chapter 4

Beam test at the Super Proton Synchrotron

In order to calibrate the detector response two beam tests at the CERN Super Proton Synchrotron (SPS) were performed on October 2014 and August 2015. The aim of the first test was to check the detector performance after the upgrade in 2014 and to calibrate the calorimeter response for the operation at the LHC. The second test was useful to post-calibrate the detector and verify its performance after the data taking at the LHC. In both the beam tests electron, proton and muon beams were available.

This work is concentrated on the beam test of 2015 for two reasons: the test was done just after the data taking at the LHC (which was on June 2015) and the data sample used for 13 TeV photon analysis is at the end of the LHCf run. Therefore detector state at LHC was more similar to the state at test of 2015 than the one in 2014. Another reason is that the test beams of 2015 were far more stable than that on 2014, so the results from the second test are more reliable than the first ones since they are all taken in the same experimental situation. All the following results refer to the beam test of August 2015.

The energies available were 100, 150, 180, 200, 230 and 250 GeV for the electron beam, 300 and 350 GeV for the proton beam and 150 GeV for the muon beam. Electron beam data were used for the calibration of detector response with electromagnetic showers. Muon beam data were used for the calibration of deep layers of the calorimeters where electromagnetic showers from electrons are not well developed. Proton data were not used in this work.

The experimental setup will be described in section 4.1. In section 4.2 the event sample of both data and Monte Carlo simulations used in this analysis will be shown. The procedure to determine the conversion factors for the conversion of the collected charge signal to the real energy deposit will be explained in section 4.3. The obtained energy resolution of the calorimeters and the linearity of the detector response will be discussed in section 4.4. Finally, an estimation of systematic uncertainties related to the calibration and to the position dependence of the signal will be discussed in section 4.5.

4.1 Experimental setup

The beam test was performed in the T2H4 beam line of the SPS. The detector was installed in an aluminum box and the temperature inside the box was controlled by a chiller. All operations were carried out under a stable temperature: the temperature variation was less than 0.1 degree per hour. To minimise materials along the beam axis before the detector, a small window on the upstream-side of the box was made and it was covered with a thin paper. Detectors and electronics were placed on a movable stage which could move along the perpendicular plane to the beam axis in order to scan all the calorimeter surface. On the stage, a micro-strip silicon detector (ADAMO [44]) was placed in front of the detector to measure the position of incident particles. Two 20 mm and 30 mm square plastic scintillators were installed between the detector and the beam pipe to generate the trigger signal. Typical beam transverse size was less than 20 mm, so the scintillators covered all the beam area. The coincidence of these scintillator signals was used as the trigger of data acquisition. Figure 4.1 shows a schematic view of the beam test setup.

The ADC module used to digitise the analogue signal of the PMTs (CAEN V965) is provided with two digital output channels for each analogue input: in the first channel the analogue signal is directly digitised (low-gain mode), while in the second channel the analogue signal is amplified by a factor 8 (high-gain mode). During electron beam operation a voltage of 600 V was applied to the PMTs and the low-gain output of ADC were used. When acquiring data with muon beam, PMTs voltage was set to 1000 V and high-gain output of ADC were used because of the much lower signal expected compared to electrons.

4.2 Data sample

A sample of ∼200k of triggered events at the center of each tower were selected for each energy for both electron and muon beams. All the events in each sample were acquired in consecutive runs. More than 1 million of

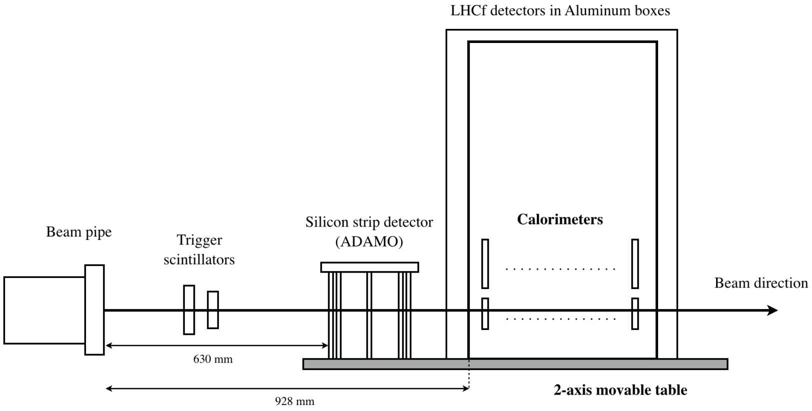

Figure 4.1: The experimental setup of the beam test at the SPS North Area. Provided beams were injected to the detector from the left side.

triggered events were collected at 150 and 200 GeV scanning all the area of the calorimeter acceptance to check the position dependence of the signal.

Since a comparison between data and simulations was necessary for the calibration (as it will be explained in section 4.3), also a set of Monte Carlo simulations was generated. The configuration of the experimental setup, including the last 12 meters of the beam pipe, was implemented in the geometry of simulations. Almost the same amount of events as the data was simulated: 200k events for each energy and for each tower. Incident particles were mono-energetic and uniformly distributed in a 5×5 mm and 10×10 mm square around the tower center for the small and large tower, respectively. For the position scan, more than 2 millions of events were simulated at 150 and 200 GeV for electrons and only 150 GeV for muons.

4.3 Detector calibration

In order to estimate the energy deposited in each layer from the measured charge (expressed in ADC units), charge distributions of each sampling GSO layer with mono-energetic electron and muon beams were compared with the prediction of Monte Carlo simulations. The first 10 scintillator layers were calibrated using electron beam, while muon beam was used for the calibration of layers from 11th to 16th since the energy deposit of electromagnetic showers was very low in the latter layers.

4.3.1 Calibration with electron beam

In order to compare data and simulations, the energy deposit of each Monte Carlo event was scaled with a conversion factor different for each scintillator layer. The energy deposit E_j^i (measured in GeV) of th i_{th} event in the j_{th} layer was multiplied by a conversion factor C_j (in ADC/GeV units), different for each layer. After the conversion, a fluctuation σ_j^i to this value was added to simulate pedestal fluctuations. The equation used for conversion is shown in equation 4.1, where S_i in the final converted energy deposit in ADC units.

$$S_j^i = C_j \cdot E_j^i + \sigma_j^i \tag{4.1}$$

Fluctuations σ_j^i are randomly sampled from a set of real pedestal events (i.e, events randomly triggered without any incident particle). A simpler approach would have been to randomly generate Gaussian fluctuation independently for each layer with a standard deviation based on measured pedestal, but in that case layer by layer correlation of the noise would not be cosidered. The energy deposit histogram was then built with the scaled energy deposit S_j^i for each layer. In case of data, the energy deposit is left as it is without any scaling. Agreement between data and simulation distributions was measured using a χ^2 test as shown in equation 4.2, where D_j^k and M_j^k are the k_{th} bin content of the j_{th} layer for data and Monte Carlo, respectively, while $\sigma_{D_j^k}$ and $\sigma_{S_j^k}$ are the statistical errors associated to bin contents.

$$\chi_j^2(C_j) = \sum_k \frac{(D_j^k - M_j^k)^2}{\sigma_{D_j^k}^2 + \sigma_{M_j^k}^2} \tag{4.2}$$

The sum $\sum_k$ ranges only over histogram bins with a content above 30% of the maximum of the distribution to avoid tail components, where there can be a contribution from the hadron contamination of the beam. All the process was repeated for several values of C_j in order to obtain the configuration which minimises the χ_j^2. After plotting χ_j^2 as a function of C_j, a fit with a 2nd order polynomial ($f(x) = a \cdot x^2 + b \cdot x + c$) was done around the minimum, as shown in figure 4.2. The fits for layers from the 2nd to the 10th are shown in figures 5 and 6 of the appendix for the small and large tower, respectively. The minimum value of the fit function ($\chi_{j,min}^2$) was chosen as the best value for the conversion factor C_j. The error on the conversion factor (ΔC_j) was defined as the interval of C_j around the minimum where the χ_j^2 increased less than "1" above the minimum value (i.e., it satisfied the relation $\Delta\chi_j^2 \equiv |\chi_j^2 - \chi_{j,min}^2| < 1$). Since there is only one free parameter (C_j), the condition $\Delta\chi_j^2 < 1$ gives a confidence interval of 1-σ for the estimation of

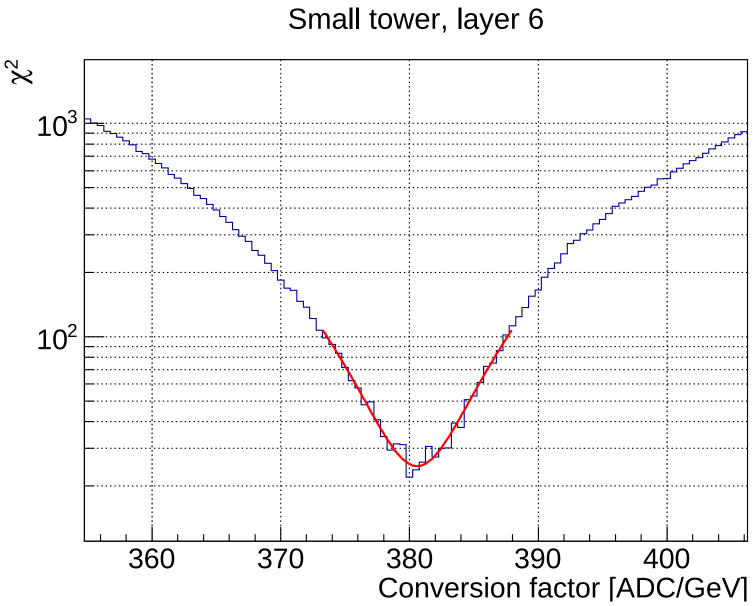

Figure 4.2: χ^2_j as a function of C_j for the 6th layer of small tower with 200 GeV electron beam (blue histogram). The fit function is represented as a red line.

the conversion factor [45]. An example of the comparison between data and Monte Carlo distributions after the fit is shown in figure 4.3.

Events selected for the calibration had to satisfy the following conditions:

1. Incident position of particles inside a square of 5 mm × 5 mm and 10 mm × 10 mm around the calorimeter center for small and large tower, respectively, to limit effects of shower leakage and non uniformity of light collection efficiency of scintillators.

2. Only one particle incident in the same tower. Events with more than one particle ("multi-hit" events) were recognized from the transverse distribution of the shower inside the calorimeter measured by the silicon detector and from the number of tracks in the ADAMO silicon tracker.

3. More than 90% of the total energy deposit released within 20 radiation lengths to avoid contamination from hadrons (whose showers develop in deeper layers of the calorimeter compared to electrons).

4. Sum-dE within 3 σ of the mean of Sum-dE distribution. At first the Sum-dE distribution was obtained for the events that satified the previous conditions, then the mean and σ of the distribution was measured

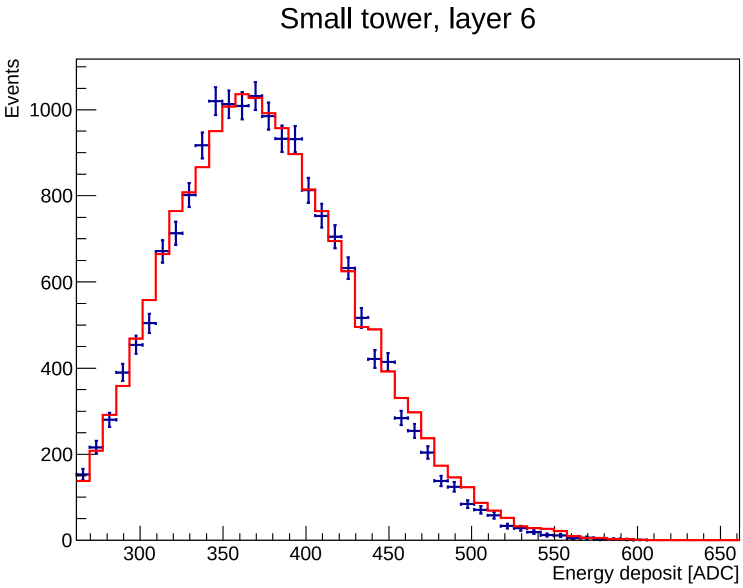

Figure 4.3: Energy deposit distribution of data (blue points) and simulation (red histogram) obtained with 200 GeV electrons for the 6th layer of small tower. The Monte Carlo distribution with best agreement with data is plotted.

with a Gaussian fit. Finally, events that satisfied this condition were selected.

Since the last two conditions needed an estimation of the C_j for all layers to equalise scintillator gains, all the procedure for the estimation of the conversion factors was iterated several times.

Best-fit distributions of energy deposit for layers from the 2nd to the 10th are shown instead in figures 4.4 and 4.5 for the small and large tower, respectively. Scaled Monte Carlo distributions well reproduce data distributions. Final results for the conversion factors with 200 GeV electron beam are presented in table 4.1. Values of the reduced χ_j^2 confirm the good agreement between data and simulations.

4.3.2 Calibration with muon beam

Since muons could penetrate through all the length of calorimeters, data obtained with muon beam were used to calculate conversion factors for all layers. The calibration procedure with muon beam was similar to the one used

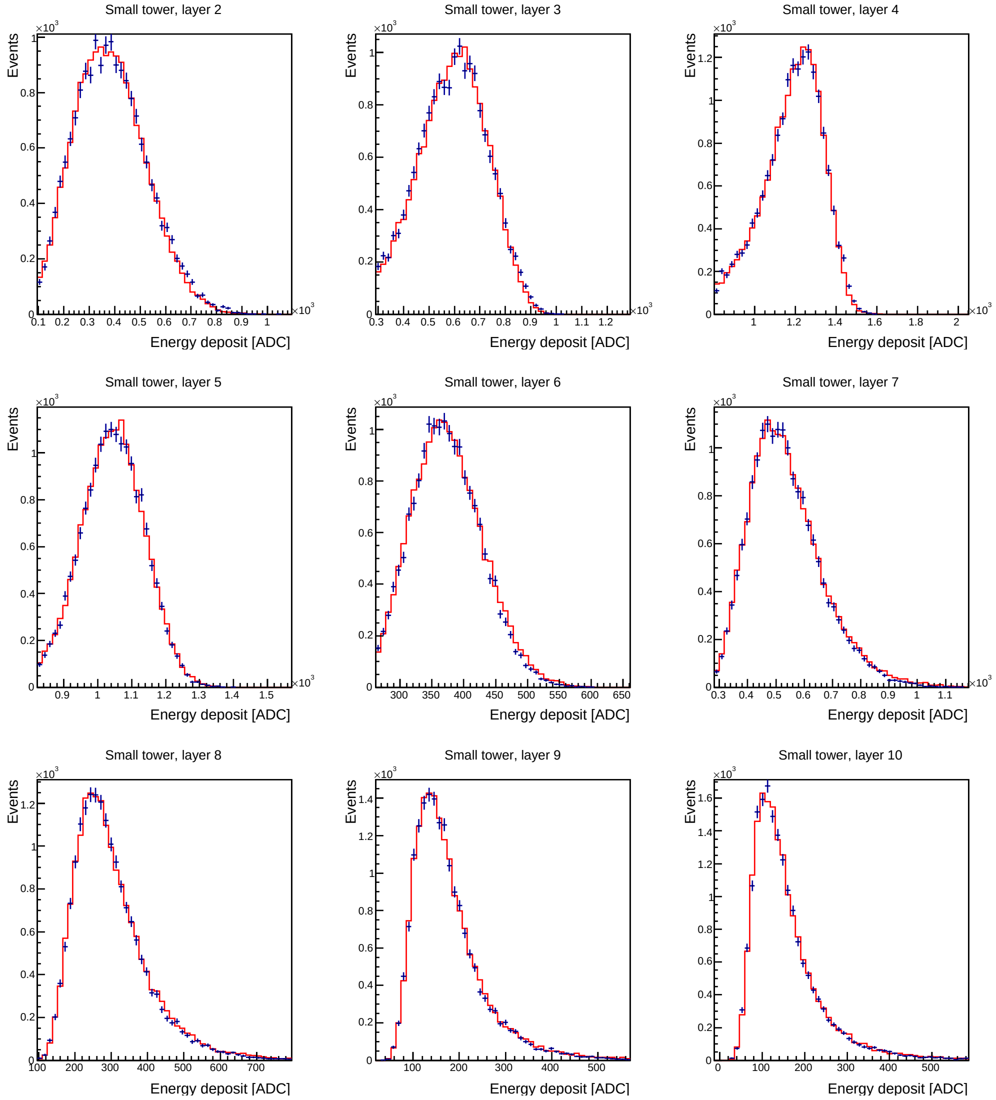
Small tower, layer 2

Small tower, layer 3

Small tower, layer 4

Small tower, layer 5

Small tower, layer 6

Small tower, layer 7

Small tower, layer 8

Small tower, layer 9

Small tower, layer 10

Figure 4.4: Energy deposit distribution of data (blue points) and simulation (red histogram) obtained with 200 GeV electrons for layers from the 2nd to the 10th of the small tower. The Monte Carlo distribution with best agreement with data is plotted.

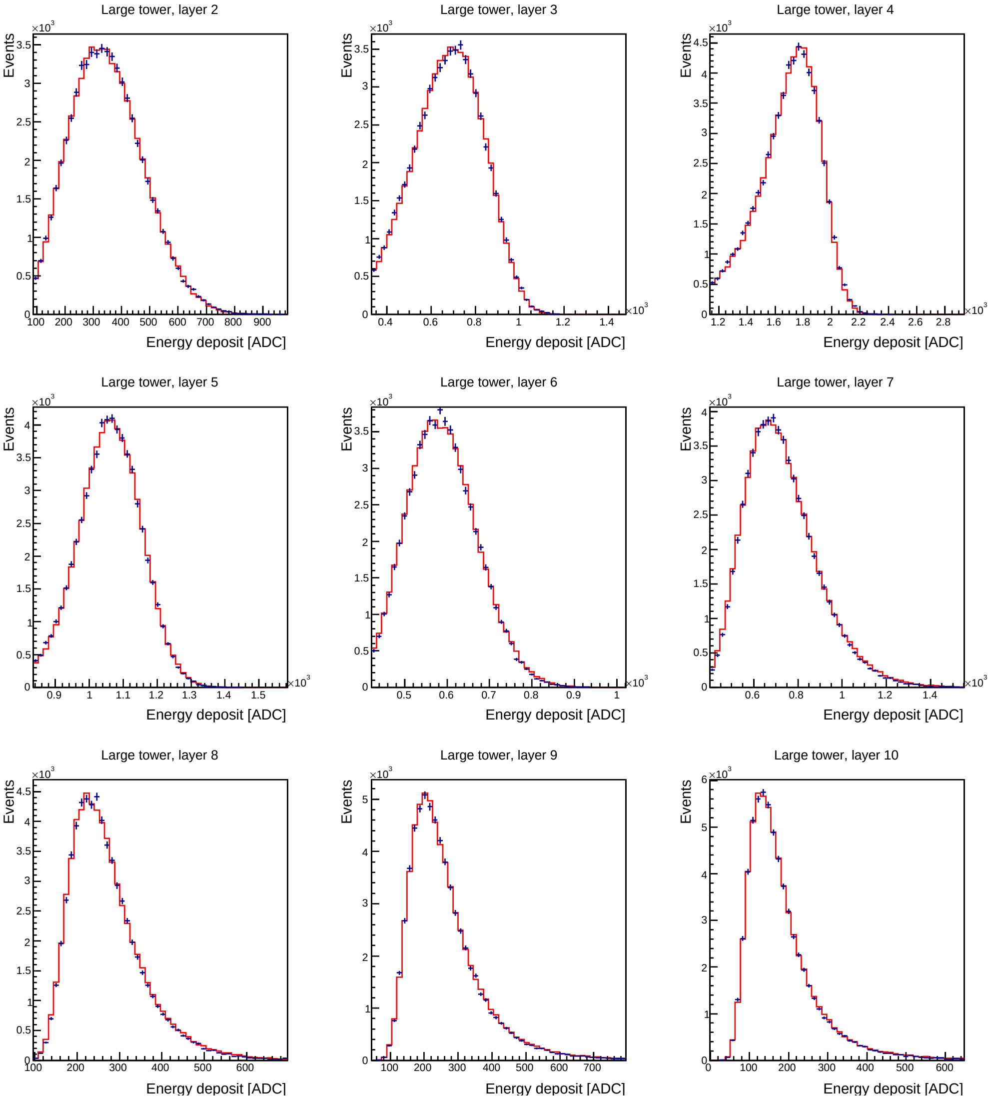

Figure 4.5: Energy deposit distribution of data (blue points) and simulation (red histogram) obtained with 200 GeV electrons for layers from the 2nd to the 10th of the large tower. The Monte Carlo distribution with best agreement with data is plotted.

	Small tower			**Large tower**		
Layer	C_j	ΔC_j	χ_j^2/ndf	C_j	ΔC_j	χ_j^2/ndf
1	820	±6	0.90	995	±4	0.51
2	828	±5	0.80	757.4	±1.9	0.52
3	576.2	±1.5	0.98	643.7	±0.9	0.81
4	802.3	±1.0	0.38	1118.0	±0.7	0.77
5	742.9	±0.8	0.75	723.1	±0.4	0.65
6	380.6	±0.8	1.00	555.1	±0.5	0.91
7	781	±2	0.31	963.1	±1.6	0.35
8	729	±3	0.25	580.9	±1.3	1.22
9	820	±4	0.80	1037	±3	0.68
10	1335	±9	0.86	1303	±4	0.25

Table 4.1: Fit results for conversion factors with 200 GeV electron beam. C_j together with its uncertainty ΔC_j and the reduced χ_j^2 are shown for each tower and layer. Units for C_j and ΔC_j are ADC/GeV.

with electrons but with an important difference: there was not only one free parameter considered but also a Poissonian smearing with mean ν_j (considered as a free parameter) was applied to simulation in addition to the scaling with the conversion factor C_j. The Poissonian smearing represents fluctuations of the number of generated photo-electrons in PMT photo-cathode that read the GSO scintillators. So, ν_j is the mean number of photo-electrons generated with a signal induced by the energy deposit of a muon in the scintillator. This smearing was negligible in case of electrons because of the very high energy deposit and, as a consequence, the high number of photo-electrons generated in each event. In addition, a Gaussian smearing (fixed to 30%) was implemented to simulate the resolution of the PMT itself. Finally, the pedestal fluctuations were implemented as was done for electrons. The implementation of these effects in simulations is shown in equation 4.3, where E_j^i is the energy deposit of the j_{th} layer in the i_{th} event, C_j is the conversion factor, $P^i(\nu_j)$ is a random number generated from a Poisson distribution with mean ν_j, $G_{30\%}^i$ is a random number generated from a Gaussian distribution with mean $= 1$ and $\sigma = 0.3$, and σ_j^i is the pedestal fluctuation. $P^i(\nu_j)$ was divided by its mean ν_j to generate a smearing distribution with mean $= 1$.

$$S_j^i = E_j^i \cdot C_j \cdot \frac{P^i(\nu_j)}{\nu_j} \cdot G_{30\%}^i + \sigma_j^i \tag{4.3}$$

Data distributions were left unchanged. The comparison between data and simulation distributions was done in the same way as in case of electrons, using equation 4.2 to calculate the χ_j^2. Since there are two free parameters, a two-dimensional grid of χ_j^2 values as a function of C_j and ν_j was created. That two-dimensional distribution was fitted with a two-dimensional 2nd order polynomial ($f(x,y) = a(x-x_0)^2 + b(x-x_0)(y-y_0) + c(y-y_0)^2 + d$) to estimate the minimum value of the χ_j^2. The error on parameters was defined as the region of (C_j, ν_j) that satisfied the relation $\Delta\chi_j^2 = |\chi_j^2 - \chi_{j,min}^2| < 2.3$ which gives a 1-σ confidence interval for the estimation of parameters C_j and ν_j [45]. The fit for the 14th layer of the large tower is shown in figure 4.6. The fits for the other layers are shown in figures 7 and 8 of the appendix for the small and large tower, respectively. An example of the comparison between data and Monte Carlo distributions after the fit is shown in figure 4.7.

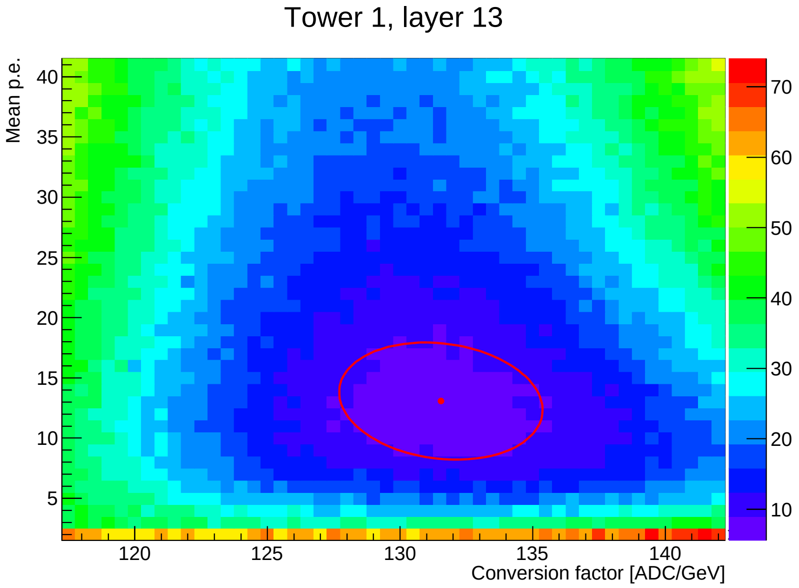

Figure 4.6: χ_j^2 as a function of C_j and ν_j for the 14th layer of large tower with 150 GeV muon beam (black points). The 1-σ confidence interval is plotted as a red line.

Events that satisfied the following conditions were selected for the measurement of the conversion factors:

1. Incident position of particles inside a square of 5 mm × 5 mm and 10 mm × 10 mm around the calorimeter center for small and large tower, respectively, to limit the effect of light collection efficiency of scintillators (leakage was not a problem since muons don't generate showers). The same acceptance area of electrons was chosen to give the possibility of a direct comparison of conversion factors.

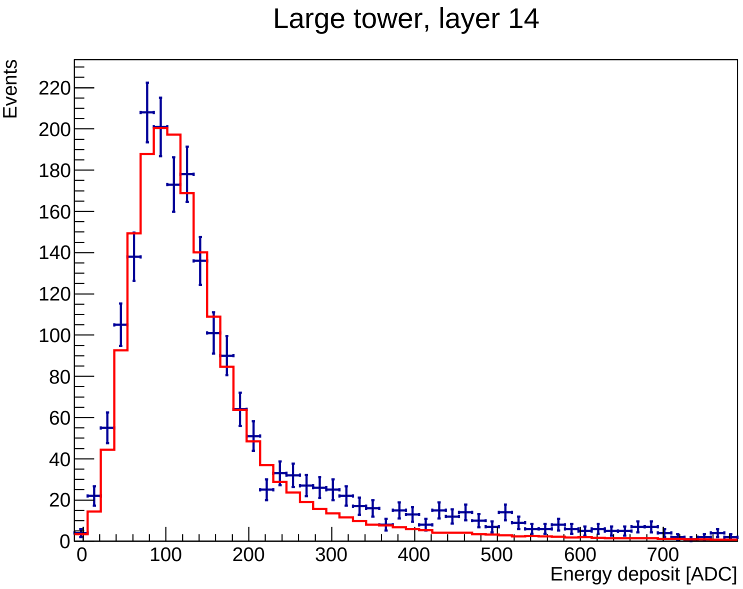

Figure 4.7: Energy deposit distribution of data (blue points) and simulation (red histogram) obtained with 150 GeV muons for the 14th layer of large tower. The Monte Carlo distribution with best agreement with data is plotted.

2. Only one particle incident in the same tower (same as electron case).
3. Alignment of the position reconstructed by the silicon microstrip layers with a tolerance of 3.2 mm (corresponding to 20 microstrips) to select non-interacting muons which passed through all the calorimeter. The tolerance could not be set smaller because of the unavoidable multiple elastic scattering of muons inside the calorimeter.

Since these conditions do not depends on C_j, an iterative method was not necessary. However, an iterative method was used to gradually decrease the intervals of C_j and ν_j where the χ_j^2 was calculated and to find the optimal intervals for the final fit.

Best-fit energy deposit distributions are shown in figures 4.8 and 4.9 for layers from the 2nd to the 13th of the small and large tower, respectively. Also in this case there is a good agreement between data and simulations. Final results for C_j estimation are shown in table 4.2. It should be noted that the PMTs voltage and gain mode of ADC used were different between electron and muon operations, so results are not directly comparable. The comparison between electron and muon beam results will be done in section 4.5 after correcting for these effects.

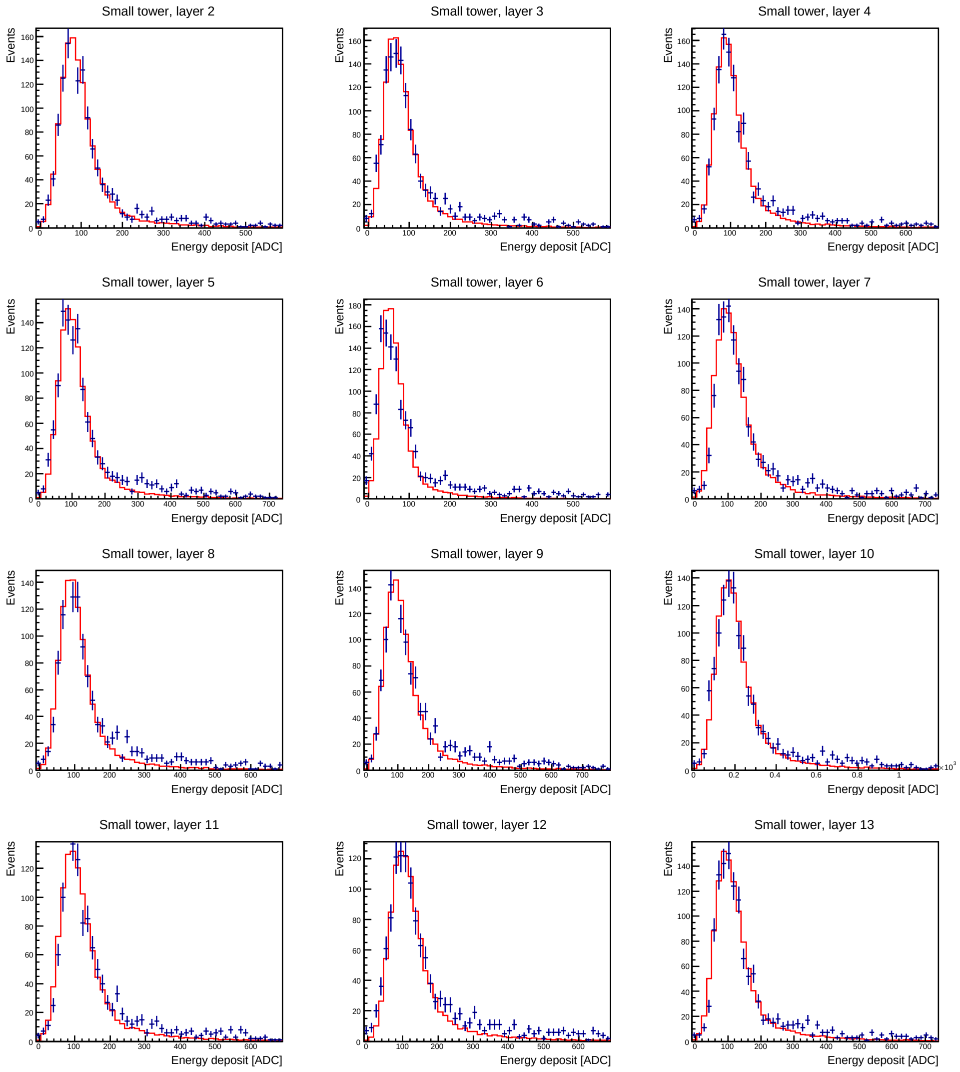

Figure 4.8: Energy deposit distribution of data (blue points) and simulation (red histogram) obtained with 150 GeV muon beam for layers from the 2nd to the 13th of the small tower. The Monte Carlo distribution with best agreement with data is plotted.

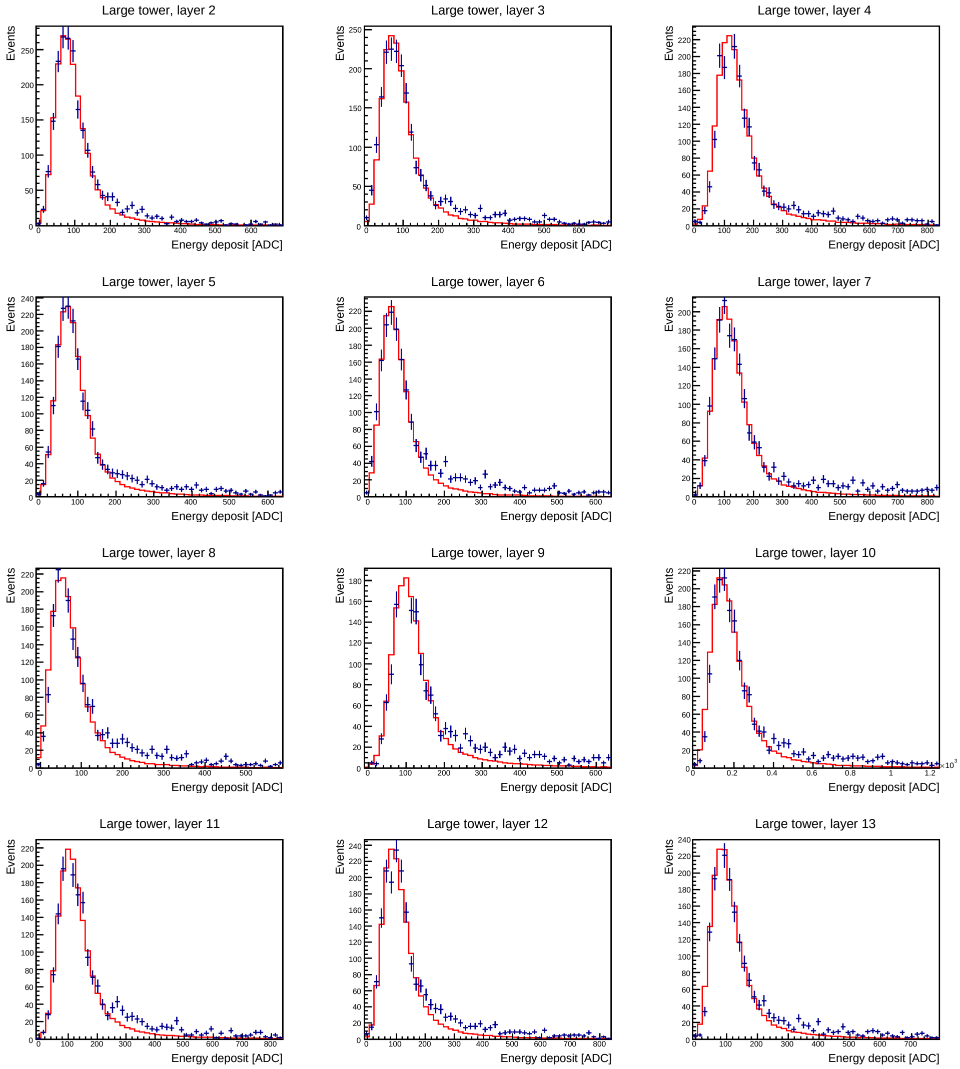

Large tower, layer 2

Large tower, layer 3

Large tower, layer 4

Large tower, layer 5

Large tower, layer 6

Large tower, layer 7

Large tower, layer 8

Large tower, layer 9

Large tower, layer 10

Large tower, layer 11

Large tower, layer 12

Large tower, layer 13

Figure 4.9: Energy deposit distribution of data (blue points) and simulation (red histogram) obtained with 150 GeV muon beam for layers from the 2nd to the 13th of the large tower. The Monte Carlo distribution with best agreement with data is plotted.

	Small tower			**Large tower**		
Layer	C_j	ΔC_j	$\chi^2/$ ndf	C_j	ΔC_j	$\chi^2/$ ndf
1	96×10^3	3×10^3	0.57	123×10^3	3×10^3	0.17
2	101×10^3	3×10^3	0.33	100×10^3	3×10^3	0.36
3	85×10^3	3×10^3	0.30	97×10^3	3×10^3	0.35
4	110×10^3	3×10^3	0.88	152×10^3	4×10^3	0.83
5	117×10^3	4×10^3	0.45	96×10^3	3×10^3	0.30
6	67×10^3	4×10^3	3.51	83×10^3	3×10^3	0.10
7	124×10^3	5×10^3	0.41	138×10^3	4×10^3	0.27
8	113×10^3	4×10^3	0.36	76×10^3	3×10^3	0.55
9	122×10^3	5×10^3	0.72	124×10^3	3×10^3	0.77
10	216×10^3	6×10^3	0.35	195×10^3	6×10^3	0.37
11	122×10^3	5×10^3	0.63	136×10^3	4×10^3	0.55
12	128×10^3	4×10^3	0.20	118×10^3	4×10^3	1.27
13	123×10^3	4×10^3	0.64	116×10^3	4×10^3	0.27
14	145×10^3	4×10^3	0.28	132×10^3	4×10^3	0.49
15	129×10^3	6×10^3	0.80	117×10^3	3×10^3	0.13
16	139×10^3	5×10^3	0.42	148×10^3	4×10^3	0.18

Table 4.2: Fit results for conversion factors with 150 GeV muon beam. C_j together with its uncertainty ΔC_j and the reduced χ_j^2 are shown for each tower and layer. Units for C_j and ΔC_j are ADC/GeV.

4.4 Energy resolution and linearity

In order to determine the energy resolution for electromagnetic showers, the total energy deposit of electrons in the scintillator layers from the 2nd to the 13th were integrated to obtain the Sum-dE, as was done in section 3.1 for simulations. Only particles incident in the center of the calorimeters were considered in order to limit the light collection efficiency and leakage effects. The chosen acceptance area was the same used for electron and muon calibration described in sections 4.3.1 and 4.3.2. Figure 4.10 shows the distribution of the Sum-dE for small tower with 200 GeV electron beam for both data and simulations. The resolution was defined as the σ divided by the mean of the Sum-dE distribution. The mean and σ were measured with a Gaussian fit on the distribution. The energy dependence of the resolution was parametrised as

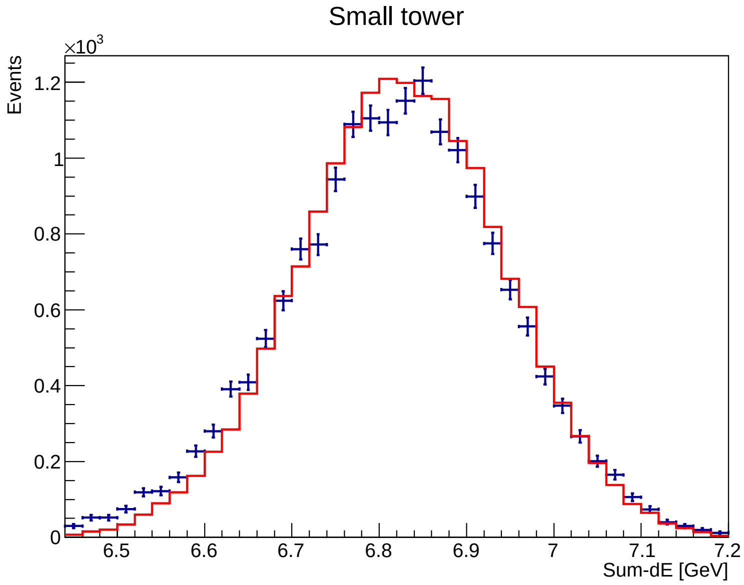

Figure 4.10: The distribution of the total energy deposit of the small tower for data (blue points) and simulation (red line) with 200 GeV electron beam.

$$\frac{\sigma}{E} = \frac{p_0}{\sqrt{E/(100\ \mathrm{GeV})}} \oplus p_1 \tag{4.4}$$

where σ/E is the resolution, E is the energy of the incident particle, p_0 and p_1 are free parameters, and '$\oplus$' represents a quadratic sum. Resolution vs energy relation measured for data and predicted by Monte Carlo together with the fit results using equation 4.4 are shown in figures 4.11 and 4.12 for

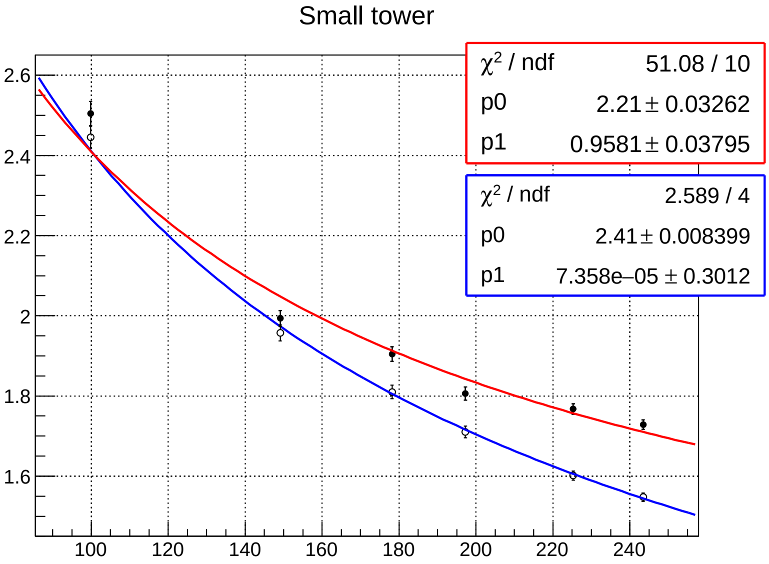

Figure 4.11: Energy dependence of the energy resolution of the small tower for data (filled circles) and simulation (open circles). The fit function is drawn as a red and blue line for data and simulation, respectively.

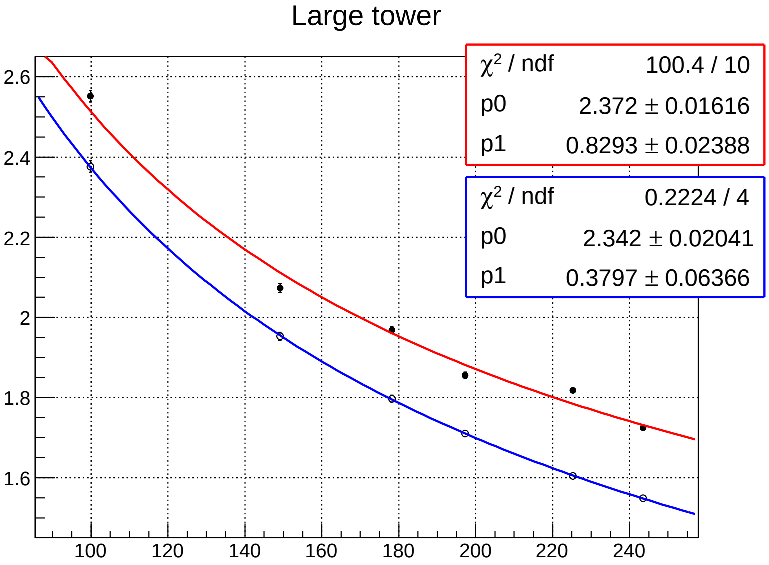

Figure 4.12: Energy dependence of the energy resolution of the large tower for data (filled circles) and simulation (open circles). The fit function is drawn as a red and blue line for data and simulation, respectively.

small and large tower, respectively. A resolution better than 2% above 150 GeV was achieved in both data and simulations. The fit function well represents simulations results but it does not agree with data within the errors. The parameter p_0 (correspondent to the stochastic contribution to the resolution) is between 2.2% and 2.4% for both data and simulations. The constant term p_1 is compatible with 0 for the small tower and 0.38% for the large tower in case of simulations, while it gives a contribution of 0.96% and 0.83% for the small and large tower, respectively, in case of data.

The linearity of the calorimeter response was checked by fitting with a linear function the relation between the Sum-dE and the energy of the incident particle ($Sum\text{-}dE = a \cdot E + b$, where E is the incident energy and a, b are free parameters) for all the electron beam energies. The energy vs Sum-dE relation and the fit function for data are shown in figures 4.13 and 4.14 for small and large tower, respectively. The deviations from linearity were smaller than 0.5% in the whole energy range between 100 GeV and 250 GeV for both towers, as shown in figures 4.15 and 4.16.

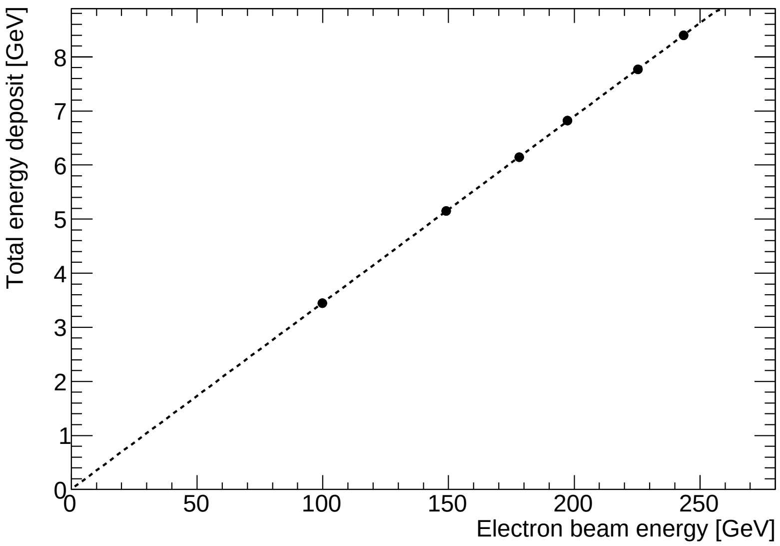

Figure 4.13: The relation between the total energy deposit and the energy of the incident particle of the small tower for measured data. The fit function is drawn as a dashed line

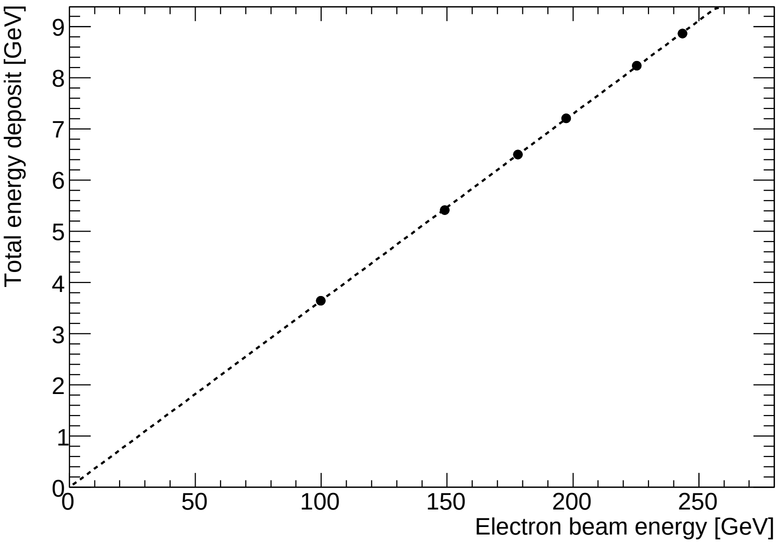

Figure 4.14: The relation between the total energy deposit and the energy of the incident particle of the large tower for measured data. The fit function is drawn as a dashed line

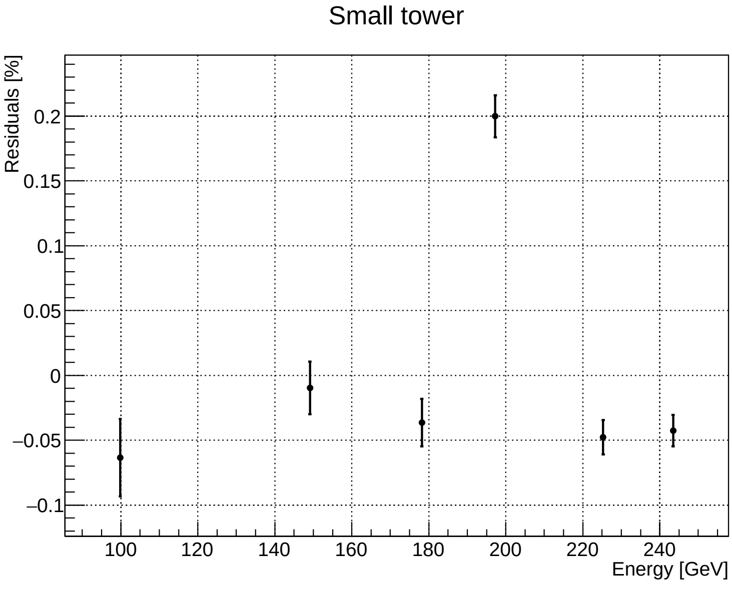

Figure 4.15: Relative residuals of the linear fit of the relation between the Sum-dE and the incident particle energy of the small tower for measured data.

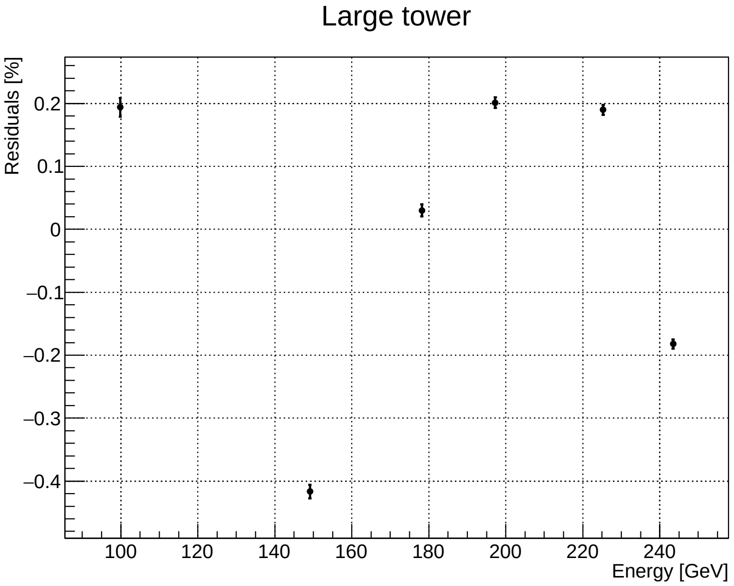

Figure 4.16: Relative residuals of the linear fit of the relation between the Sum-dE and the incident particle energy of the large tower for measured data.

4.5 Systematic errors estimation

Using SPS data there was the possibility to estimate two contribution to the systematic uncertainty of the energy scale. The uncertainty on the measurement of conversion factors will be discussed in section 4.5.1, while the error associated to the position dependence of the signal will be examined in section 4.5.2. Other contributions to the energy scale systematic error will be discussed later in section 5.6.1.

4.5.1 Conversion factors

The conversion factors determined with different electron beam energies and with muon beam were compared to estimate the systematic uncertainties associated to the measurement of factors C_j. Since the applied high voltages for the PMTs were 600 V and 1000 V for the electron and muon operations respectively, the muon conversion factors were re-scaled by the ratio of the PMT gain between the two configurations (ranging between 14 and 21). The temperature dependence of the PMT gain was also measured with a calibration laser and corrected before comparing muon factors and electron factors. Figures 4.17 and 4.18 show the conversion factors of layers from the

2nd to the 10th (called "electromagnetic layers", or "EM layers", hereafter) for muon beam and all electron beams for small and large tower, respectively. Factors are normalised to the ones measured with the 200 GeV electron beam.

Systematic error associated to the conversion factors was defined as the relative deviation of factors from the ones measured at 200 GeV. The error was estimated using only EM layers, where electromagnetic shower are well developed. The contribution from other layers to the Sum-dE is estimated from simulations as 1.4 % for a 200 GeV photon and 6 % for a 6 TeV photon, so their contribution to the energy reconstruction (and its uncertainty) is small compared to EM layers. The root mean square of deviation for electron-based factors was 0.8 %, while deviations of muon-based factors were of the order of 5-10 %. Since muon factor are used only in latter layer where the energy deposit is small, the contribution of the systematic uncertainty on muon-based factor is negligible. For this reason, the systematic uncertainty

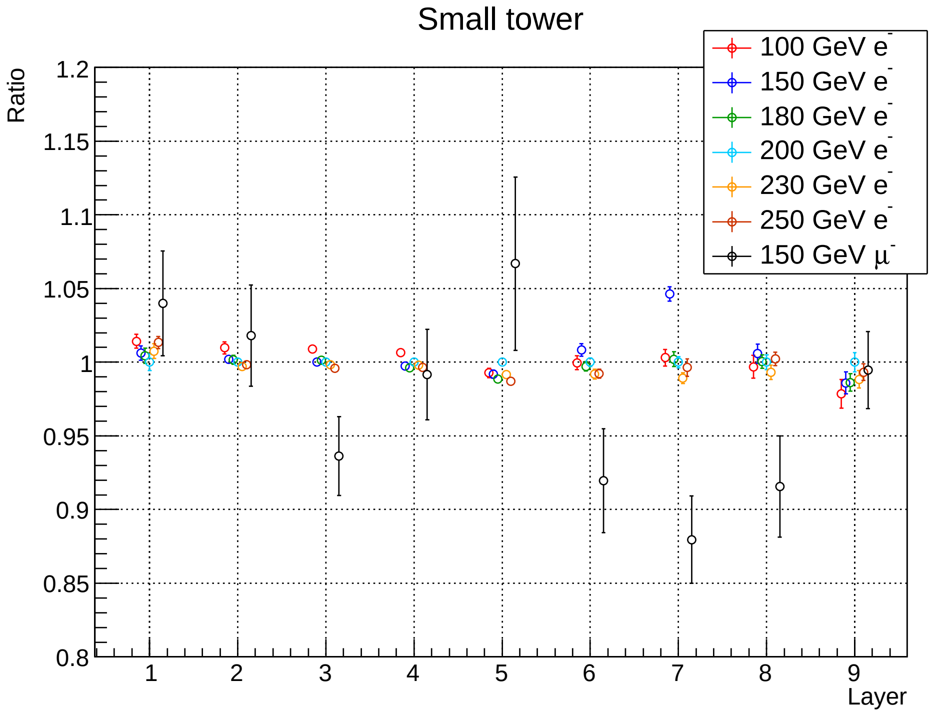

Figure 4.17: Conversion factor of the small tower measured with different electron energies (coloured points) and with muons (black points) normalised to factors obtained with 200 GeV electrons. Only electromagnetic layers are shown.

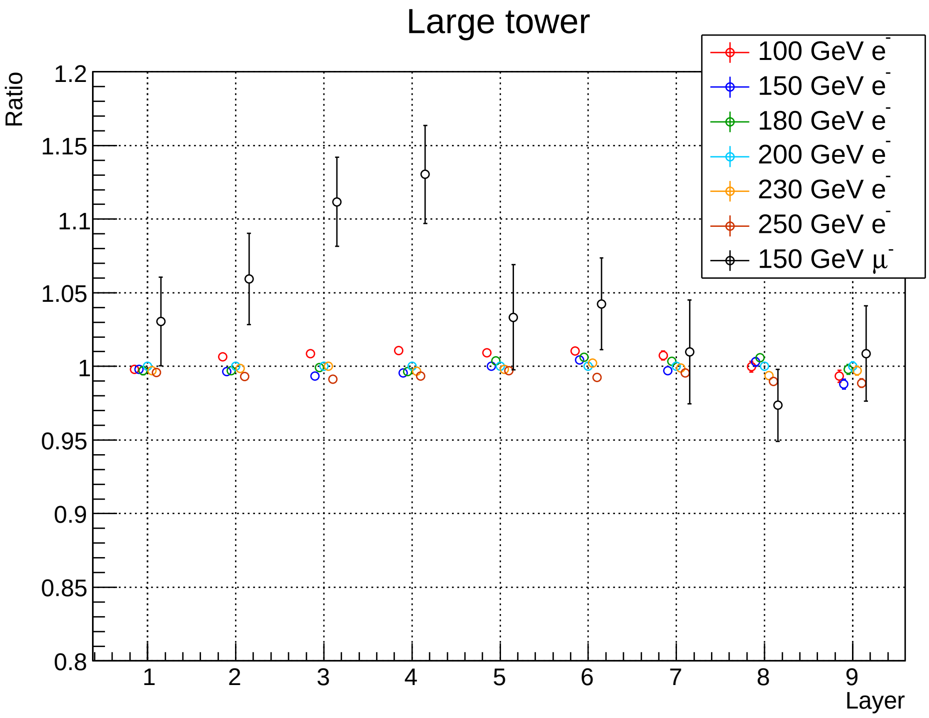

Figure 4.18: Conversion factor of the large tower measured with different electron energies (coloured points) and with muons (black points) normalised to factors obtained with 200 GeV electrons. Only electromagnetic layers are shown.

associated to the conversion factors measurement was estimated as 0.8 %. In the following analysis, coversion factors obtained with the 200 GeV electron beam were used for EM layers, while muon-based factors were used for latter layers.

4.5.2 Non-uniformity correction

Using the data sample from the scan of the whole surface of the towers, the performance of the correction for the position dependence of calorimeters response described in section 3.2.3 could be checked. The transverse surface of each tower was divided in a grid of 1 mm bins and the mean Sum-dE was computed for each position bin before and after the non-uniformity correction. The region within 2 mm from the calorimeter border was removed because the gradient of the position dependence of the signal was too large and it could not be properly corrected using this method. The map of the position dependence of the Sum-dE is shown in figures 4.19 and 4.20 for the small and large tower, respectively. The leakage and efficiency correction greatly improved the uniformity of the detector response, since the deviations from the Sum-dE at the center of the calorimeter were 1.1 % and 1.0 % for small and large tower respectively. The systematic error due to the position dependence of the detector response was set to 1.1 %.

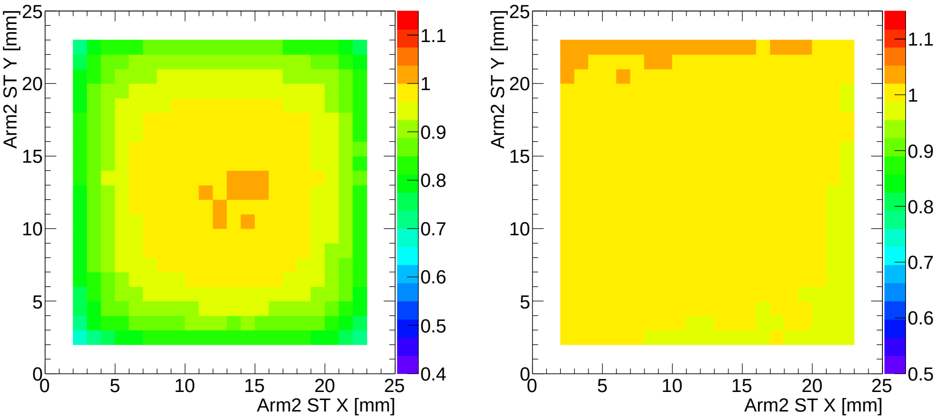

(a) Before correction

(b) After correction

Figure 4.19: The position dependence of the Sum-dE. X and Y represent the transverse coordinates of the small tower. An uniformity at the level of ~ 1 % is realized after the correction.

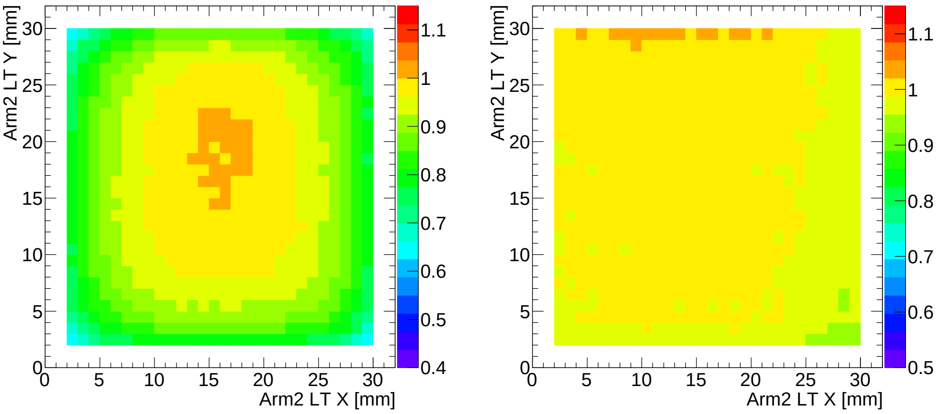

(a) Before correction (b) After correction

Figure 4.20: The position dependence of the Sum-dE. X and Y represent the transverse coordinates of the large tower. An uniformity at the level of ~ 1 % is realized after the correction.

Chapter 5

Data analysis for proton-proton collisions at $\sqrt{s} = 13$ TeV

In this chapter the details of data analysis will be described. The data taking conditions and the data sample used for this analysis will be described in section 5.1. The reconstruction procedure of each acquired event will be explained in section 5.2 while criteria for the selection of events will be discussed in section 5.3. The correction to be applied to the spectrum due to the particle identification (PID) selection will be discussed in section 5.4 while the correction for the response of the detector (unfolding) will be explained in section 5.5. The contribution from systematic errors to the energy spectrum of photons will be discussed in section 5.6 and finally the spectrum will be compared with Monte Carlo predictions in section 5.7.

5.1 The LHCf run

The LHCf data taking for proton-proton collisions at $\sqrt{s} = 13$ TeV was performed from 10th to 13th of June 2015 at the Large Hadron Collider. Since the detectors were not suitable for high luminosity operations because of radiation damage, a dedicated run with low luminosity was provided for LHCf. During all operation the trigger was exchanged with the ATLAS experiment to give the possibility of a common analysis which can provide useful information about the type of collision from which events recorded by LHCf were originated. The instantaneous luminosity was $\sim 10^{29}\text{cm}^{-2}\text{s}^{-1}$ with a pile-up [1] $\mu = 0.01$ or 0.03. The total crossing angle between colliding beams was 290 μrad, while β^* was 19 m. The total data acquisition time was 26.6 hours, during which 4×10^7 shower events in calorimeters were recorded

---

[1] Mean number of collisions in a single bunch crossing.

and 5×10^5 π^0 decays were observed. The integrated number of events as a function of time is shown in figure 5.1. An example of π^0 event is shown in figure 5.2.

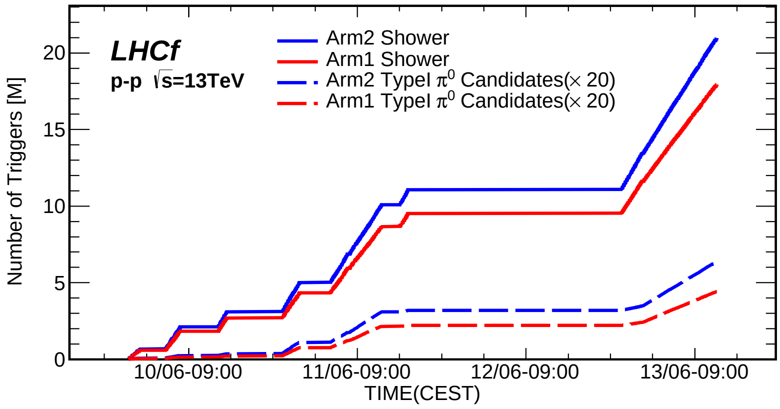

Figure 5.1: Number of integrated events recorded by LHCF as a function of time. Solid lines represent the number of showers observed in each detector, while dashed lines show the number of observed π^0 events (multiplied by 20 for convenience). Red lines show Arm1 data while blue ones show Arm2 data.

Fill #3855 was selected for the data analysis in this work. This decision was based on the fact that it was the LHCf-dedicated fill which lasted longer (14 hours) and its luminosity was more stable than the previous long fill (#3851, about 11 hours). For the first 3 hours beams were colliding with $\mu = 0.01$ and a luminosity of $\sim 0.4 \times 10^{29}$, then μ was increased to 0.03 (and the luminosity to $\sim 1.4 \times 10^{29}$). Only the data acquired with $\mu = 0.01$ were used in this analysis to minimise the probability of pile-up events. The statistics was enough for the purpose of this analysis anyway.

The integrated luminosity of the selected sample of data was calculated from the instantaneous luminosity derived by ATLAS from a calibration of the luminosity scale using x-y beam-separation scans performed in August 2015, following a methodology similar to that detailed in [46]. The instantaneous luminosity was multiplied by the DAQ efficiency of LHCf (between 40% and 50%) and integrated over all the run time. The resulting integrated luminosity recorded by LHCf was 0.191 nb^{-1} with a precision of 1.9%. Since the energy spectrum will be normalised to the number of inelastic collisions, also the inelastic cross section of proton-proton collisions (σ_{inel}) was necessary. The cross section was extrapolated from TOTEM data at $\sqrt{s} = 8$

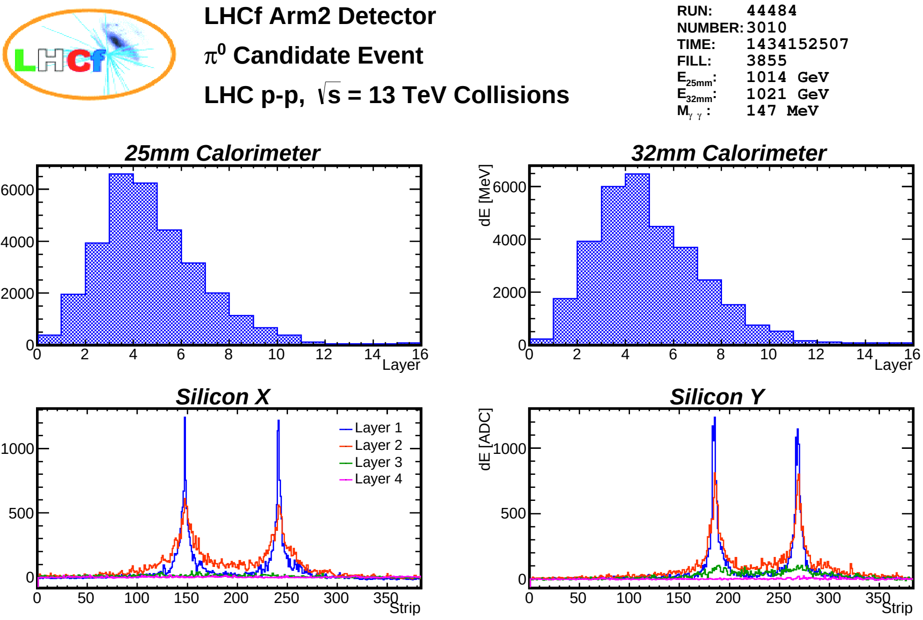

Figure 5.2: A π^0 event detected by the Arm2 detector. Each tower was hit by a ~ 1 TeV photon from a π^0 decay. Longitudinal profile of shower inside the calorimeters is shown in the upper plots, while the transverse profile measured by the silicon layers is shown in the bottom plots for both the horizontal (X) and vertical (Y) axis.

TeV using the best fit of σ_{inel} vs $\sqrt{s}$ relation done by the COMPLETE collaboration [45, 47]. The extrapolated value of the inelastic cross section at $\sqrt{s} = 13$ TeV was 78.53 mb, so the estimated number of inelastic collision was 1.50×10^7.

5.2 Reconstruction procedure

There were several steps to be performed in order to convert the measured energy deposit in scintillators into the energy of the photon. The silicon detectors were used instead to measure the position of the incident particle, which will be used to determine the angle of the particle with respect to the beam axis and to calculate the position dependence correction described in section 3.2.3. In case of Monte Carlo simulations, the same method used for data was utilised for reconstructing the events; in addition, pedestal fluctuations were implemented for both position and energy reconstruction.

5.2.1 Position reconstruction

A single silicon detector covers both small and large tower, so when measuring the position of a particle incident in a calorimeter only the range of strips that cover the tower was considered. The TSpectrum [48–50] method was used to identify position and number of the peaks observed in silicon. Then, a fit with a 3-component Lorentzian function was done on the measured transverse distribution of the shower. The fit function is expressed in equation 5.1 [51]:

$$f(x) = p_0 \left[\frac{p_2}{\frac{(x-p_1)^2}{p_3} + p_3} + \frac{p_4}{\frac{(x-p_1)^2}{p_5} + p_5} + \frac{1 - p_2 - p_4}{\frac{(x-p_1)^2}{p_6} + p_6} \right] \tag{5.1}$$

where x is the X or Y coordinate depending on the orientation of the strips and p_0 ... p_6 are free parameters. Initial values of parameters were set using the information from TSpectrum. The reconstructed position was defined as the parameter p_1 after the fit in the couple of X-Y detectors with the maximum energy deposit. In events where there were two (or more) peaks found by TSpectrum in the same tower, the fit function was constructed as the sum of two functions defined with equation 5.1: so, the number of free parameters was 14 instead of 7.

5.2.2 Energy reconstruction

The reconstruction of the energy of a particle from the energy deposit in scintillators was composed of the following steps:

1. Energy deposit conversion: the measured energy deposit in ADC units was converted to the real energy deposit according to the following equation:

   $$dE^i_j = S^i_j \cdot \frac{G_j(HV_j)}{C_j} \cdot \frac{1}{P_j(x_i, y_i)} \cdot \frac{1}{A_j} \tag{5.2}$$

   where

   - S^i_j is the measured energy deposit in ADC units for the j-th scintillator in the i-th event, after the subtraction of the pedestal.
   - C_j is the conversion factor measured at the beam test at SPS, as described in section 4.3.
   - $G_j(HV_j)$ is the factor between the gain of the PMT at 600 V (which was used at SPS) and the gain at the voltage HV_j used at LHC, ranging from 375 V to 450 V for different layers.

- $P_j(x_i, y_i)$ is the correction factor for the non-unifomity of the detector response calculated for the reconstructed position (x_i, y_i), as described in section 3.2.3.
- A_j is the attenuation factor of the analog signal along the ~ 200 meters long cable that connects the detector to the readout electronics. It was measured at the SPS using a replica of the 200 meters long cable.
- dE^i_j is the energy deposit measured for the j-th scintillator in the i-th event converted to GeV units and corrected for the position dependence of the signal.

Obviously, this step was not performed when analysing Monte Carlo simulations,

2. Total energy release: the total energy deposit in the calorimeter was obtained computing the Sum-dE as defined in section 3.1:

$$\text{Sum-dE} = \sum_{j=2}^{13} dE_j \cdot w_j \tag{5.3}$$

where dE_j is the energy deposit in the j-th layer, while $w_j = 1$ for $j \leq 11$ and $w_j = 2$ for $j \geq 12$ to deal with the different sampling step of scintillator layers.

3. Energy estimation: finally, the Sum-dE was converted to the energy of the primary particle using equation 3.1, which was previously discussed in section 3.1. In order to check the validity of the absolute energy scale for data, the invariant mass of the two photons in π^0 events was reconstructed. The π^0 mass peak was not found at the expected value of 134.98 MeV, even in Monte Carlo simulations: since events with a photon in each tower were considered, part of the shower developed in a calorimeter enters in the other tower and increases its reconstructed energy (the so called "leakage-in" effect). Since there was not a correction applied for this effect, the energy scale was checked by comparing the π^0 mass peak of data with the one predicted by simulation. The peak of the invariant mass distribution was found with a Gaussian fit restricted around the maximum as shown in figure 5.3 for both data and Monte Carlo. The peak in data was found 1.6% below the one predicted by simulation. A re-scaling factor of 1.016 was applied to the energy of each photon event to account for this energy scale shift. As will be discussed in section 5.6.1, this shift was consistent with the estimated systematic error.

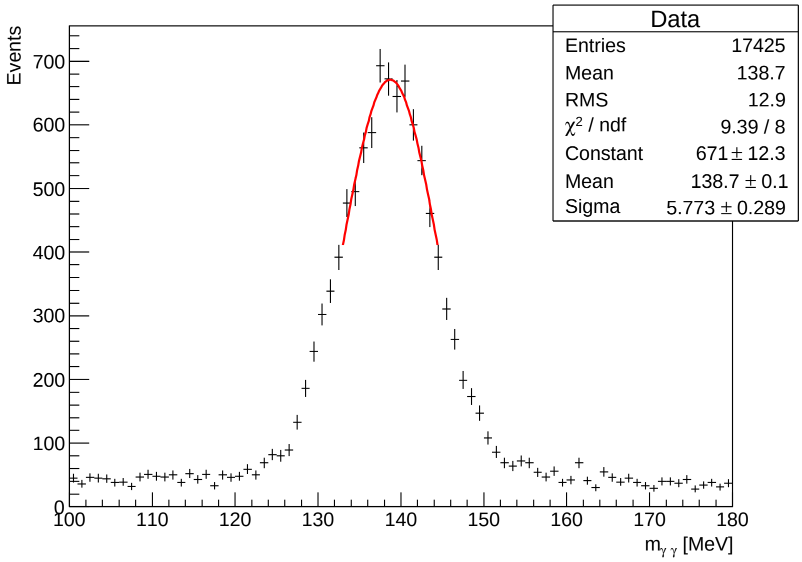

(a) Data

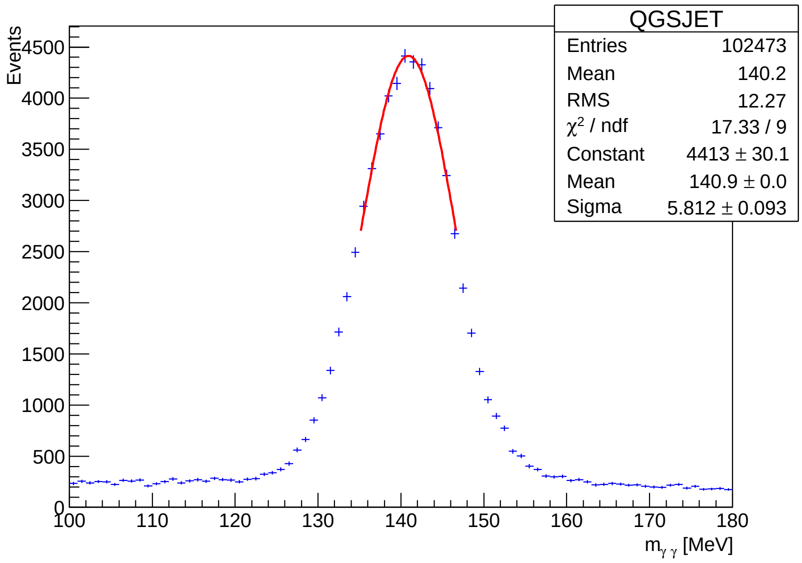

(b) Simulation

Figure 5.3: Invariant mass distribution of events with a photon incident on each tower (blue histogram). The π^0 mass peak of both data and simulation was shifted because of the leakage-in effect. A systematic shift of 1.6% of data peak with respect to Monte Carlo prediction can be seen from the result of the Gaussian fit around the peak (red line).

5.3 Event selection

In order to select the desired sample of photon events, the following cuts were applied:

- Particle identification cut (PID): hadron events was rejected to select only photon-induced showers. The discrimination was based on the longitudinal profile of the shower development in the calorimeter. The PID cut is a function of one parameter, $L_{90\%}$, which was defined as the longitudinal depth in the tower where 90% of the total energy deposit is contained. A lower value of $L_{90\%}$ is expected for electromagnetic showers with respect to hadronic ones because of the significantly lower value of the radiation length compared to the hadronic interaction length in tungsten. The $L_{90\%}$ distribution of all shower developing in the small tower is shown in figure 5.4. An energy dependent threshold, L_{thr}, was defined: particles with $L_{90\%} < L_{thr}$ were identified as photons, while other particles were identified as hadrons and discarded from the analysis. Details about the choice of the threshold and the study of the correction for efficiency and purity of this cut will be explained in section 5.4.

- Energy cut: only events with an energy $>$ 200 GeV were selected to have a $\sim$ 100% trigger efficiency and to avoid background from low energy particles produced in the interaction of collision products with the beam pipe.

- Multi-hit cut: events with more than one particle in the same tower (multi-hit events) were rejected due to the difficulty to determine the sharing of the energy deposit in scintillators between the two (or more) particles. The correction for the effect of this cut on the energy spectrum will be discussed in section 5.5.

- Position cut: as already explained in section 4.5.2, the region within 2 mm from the tower edge was excluded from the analysis because the position dependence of the signal was not properly corrected. However, the pseudorapidity cut described below automatically excluded this region.

- Pseudorapidity cut: using the reconstructed position from the silicon detectors, only events falling in a limited range of pseudorapidity η and azimuthal angle ϕ were selected: $\eta > 10.94$ and $-90^\circ < \phi < 90^\circ$ for the small tower, $8.81 < \eta < 8.99$ and $45^\circ < \phi < 65^\circ$ for the large tower. The same ranges were also chosen for Arm1 detector to allow combining later the data of both Arms. In order to calculate η and ϕ, also the position of the centre of the beam was necessary. The beam centre was measured by taking advantage of the fact that hadron distribution hitmap presents a peak in the very forward region as shown in figure 5.5. A fit with a two-dimensional exponential function was done on the hitmap of hadrons to get the beam centre [40]. The hitmap of photons with energy $>$ 200 GeV inside the selected pseudorapidity regions is shown in figure 5.6.

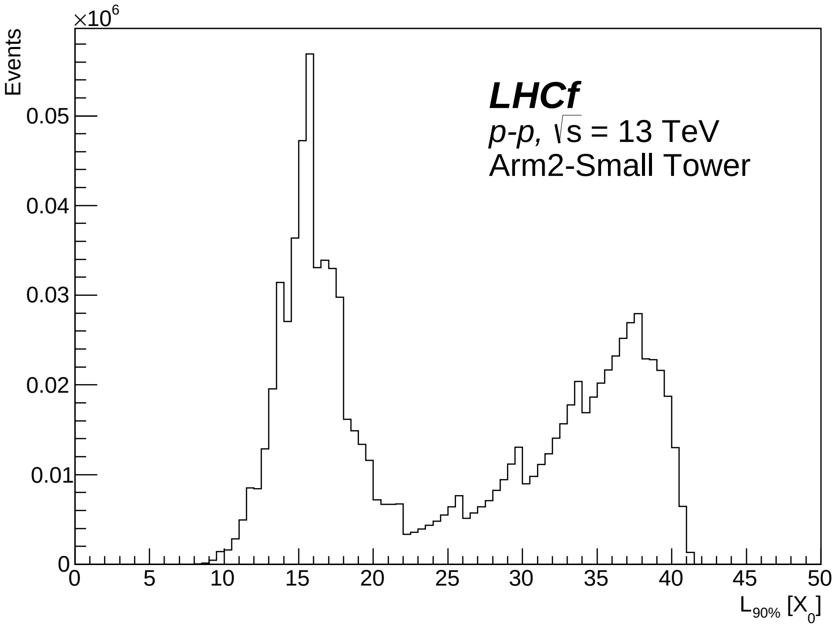

Figure 5.4: $L_{90\%}$ distribution of all events recorded in the small tower with reconstructed energy $>$ 200 GeV. The peak around 16 X_0 is related to electromagnetic showers, while the other big peak corresponds to hadronic showers. Small structures at 26, 30 and 34 X_0 are caused by the discrete sampling of the shower.

5.4 PID correction

As described in the prevoius section, the parameter $L_{90\%}$ was used to discriminate photons from hadrons. Efficiency and purity of this particle identification method must be calculated in order to correct for the bias of this cut.

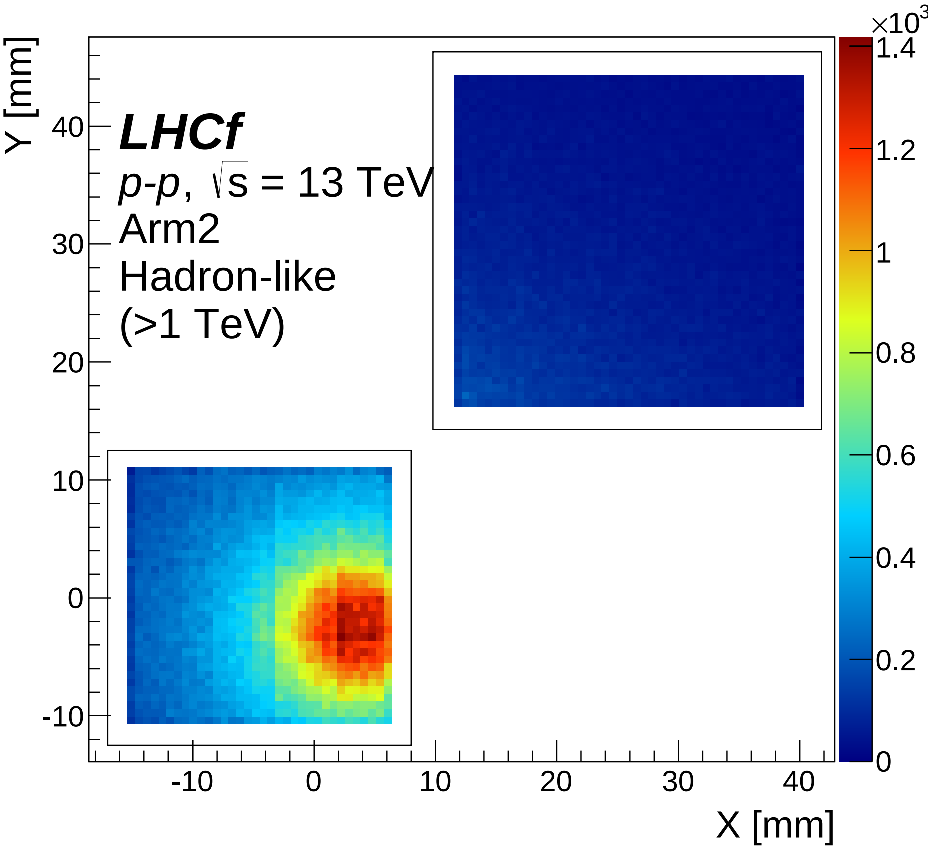

Figure 5.5: Hitmap of hadrons with energy > 1 TeV. Black boxes represent the tower boundaries. The hadron distribution features a peak in the very forward region around the centre of the beam.

The PID efficiency was defined as the fraction of photons properly identified with respect of the total number of photons:

$$\epsilon = \frac{n_{gg}}{n_{gg} + n_{gh}} \tag{5.4}$$

where n_{gg} is the number of photons properly identified and n_{gh} is the number of photons identified as hadrons (i.e., gammas with $L_{90\%} > L_{thr}$). The PID purity was defined as the fraction of real photon events in the sample of events passing the PID cut:

$$P = \frac{n_{gg}}{n_{gg} + n_{hg}} \tag{5.5}$$

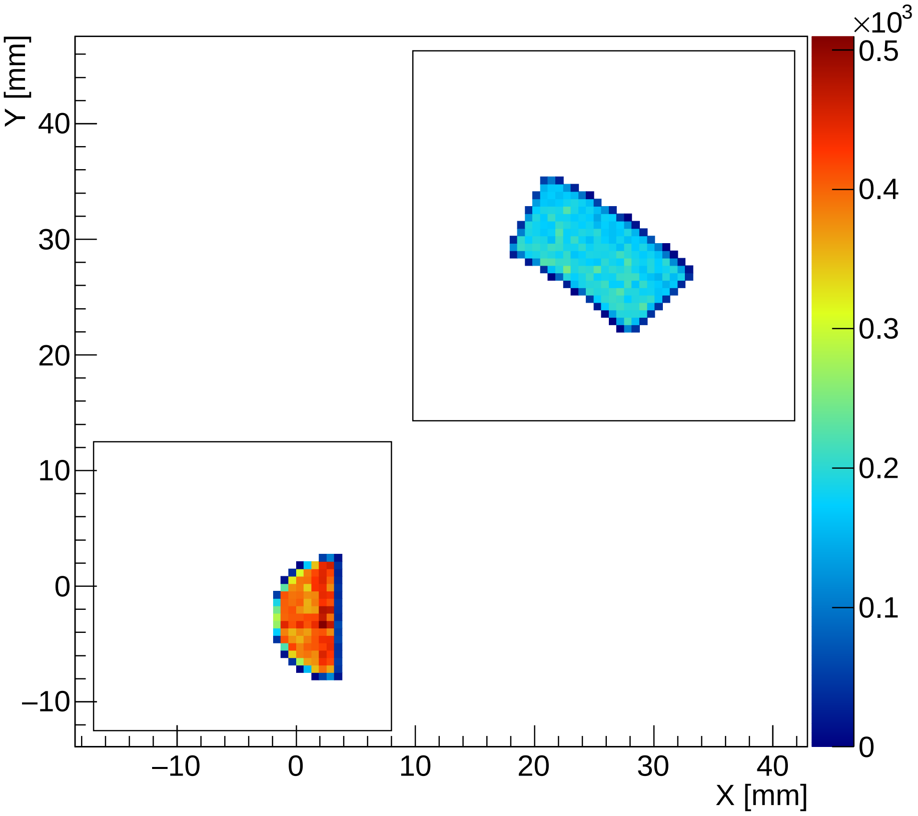

Figure 5.6: Hitmap of photons with energy $>$ 200 GeV in the selected pseudorapidity regions. Black boxes represent the tower boundaries.

where n_{gg} is the number of photons identified as gammas and n_{hg} is the number of hadrons identified as photons (i.e., hadrons with $L_{90\%} < L_{thr}$). In order to obtain the real number of photon events, the measured number has to be multiplied by a factor $P \cdot \epsilon^{-1}$. Since the distribution of $L_{90\%}$ depends on the energy of the particles, ϵ and P also depend on the energy region considered. So, efficiency and purity were estimated in each energy bin of the final energy spectrum histogram.

The sample of 10^8 events simulated with QGSJET described at the beginning of chapter 3 was used to estimate the PID efficiency as a function of L_{thr} and of energy. L_{thr} was fixed in each energy bin to obtain $\epsilon = 90\%$. In order to obtain a continuous L_{thr} as a function of the energy, the obtained

L_{thr} vs energy plot was fitted with the function

$$L_{thr}(E) = p_0 \cdot \ln(p_1 \cdot E + p_2) \tag{5.6}$$

where E is the energy and p_0, p_1 and p_2 are free parameters. The value of L_{thr} for each analysed event was calculated with equation 5.6 using the reconstructed energy of the particle. The results of the fit for small and large tower are listed in table 5.1. The plot of L_{thr} vs E, including the best fit function, is shown in figure 5.7.

Tower	p_0 $[X_0]$	p_1 $[\mathrm{GeV}^{-1}]$	p_2
Small	2.16	3.01	3.05×10^3
Large	1.66	69.3	3.50×10^4

Table 5.1:

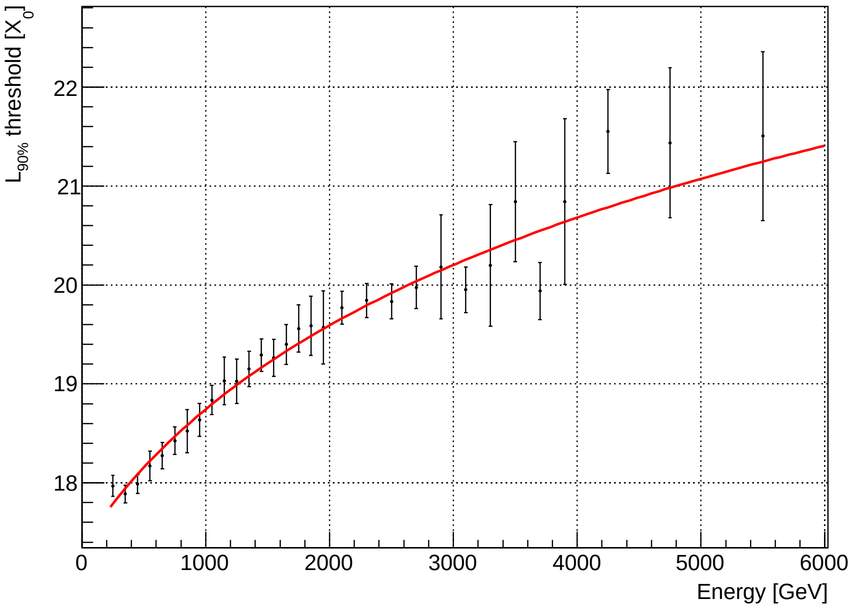

Figure 5.7: L_{thr} as a function of the energy for the small tower. The fit function is drawn in red.

While the PID efficiency only depends on the shape of the photon $L_{90\%}$ distribution, PID purity depends also on the ratio between the number of hadron events and the photon yield. The last quantity strongly depends on the model used as generator, so it was not possible to rely on results of a single model. In order to obtain a more accurate estimation of the purity, the so called "template fit" was used. In each energy bin the $L_{90\%}$ distribution of the QGSJET sample (the "template") was compared with the one obtained from measured data. The contributions of photons and hadrons to the template $L_{90\%}$ distribution were separated using the Monte Carlo truth and independently normalised to better fit the experimental distribution. Normalisation factors, indicated with α and β for the photon and hadron distribution, respectively, were treated as free parameters. The comparison of $L_{90\%}$ distribution between data and normalised simulation was done for each energy bin with a χ^2 test:

$$\chi^2(\alpha,\beta) = \sum_k \frac{(D_k - M_k(\alpha,\beta))^2}{\sigma^2_{D_k} + \sigma^2_{M_k(\alpha,\beta)}} \tag{5.7}$$

where D_k and $M_k(\alpha,\beta)$ are the counts in the k-th bin of the $L_{90\%}$ distribution histogram for data and template, respectively, while σ_{D_k} and $\sigma_{M_k(\alpha,\beta)}$ are the associated errors to the bin contents. The simulation normalised with the best-fit α and β factors was finally used to estimate the purity:

$$P = \frac{\alpha n_{gg}}{\alpha n_{gg} + \beta n_{hg}} \tag{5.8}$$

Some examples of best-fit template distributions are shown in figures 5.8 and 5.9. Normalised template distributions well reproduce data distributions.

The corrected energy spectrum and the confidence interval were estimated with a log-likelihood approach. The number of observed photon events N_{obs} follows the Poisson distribution with mean $N_{corr} \cdot \epsilon \cdot P^{-1}$, where N_{corr} is the estimated real number of photons. The probability to observe N_{obs} is given by

$$\begin{aligned} &Prob(N_{obs}|N_{corr},\epsilon,P) = \frac{\mu^{N_{obs}} e^{-\mu}}{N_{obs}!} \\ &\mu = N_{corr} \cdot \epsilon \cdot P^{-1} \end{aligned} \tag{5.9}$$

PID efficiency and purity follow instead the binomial distribution:

$$Prob(k|m,p) = \frac{m!}{k!(m-k)!}\, p^k (1-p)^{(m-k)} \tag{5.10}$$

with $m = n_{gg} + n_{gh}$, $k = n_{gg}$, $p = \epsilon$ for efficiency and $m = n_{gg} + n_{hg}$, $k = n_{gg}$, $p = P$ for purity. Since k and m were measured from the simulation and

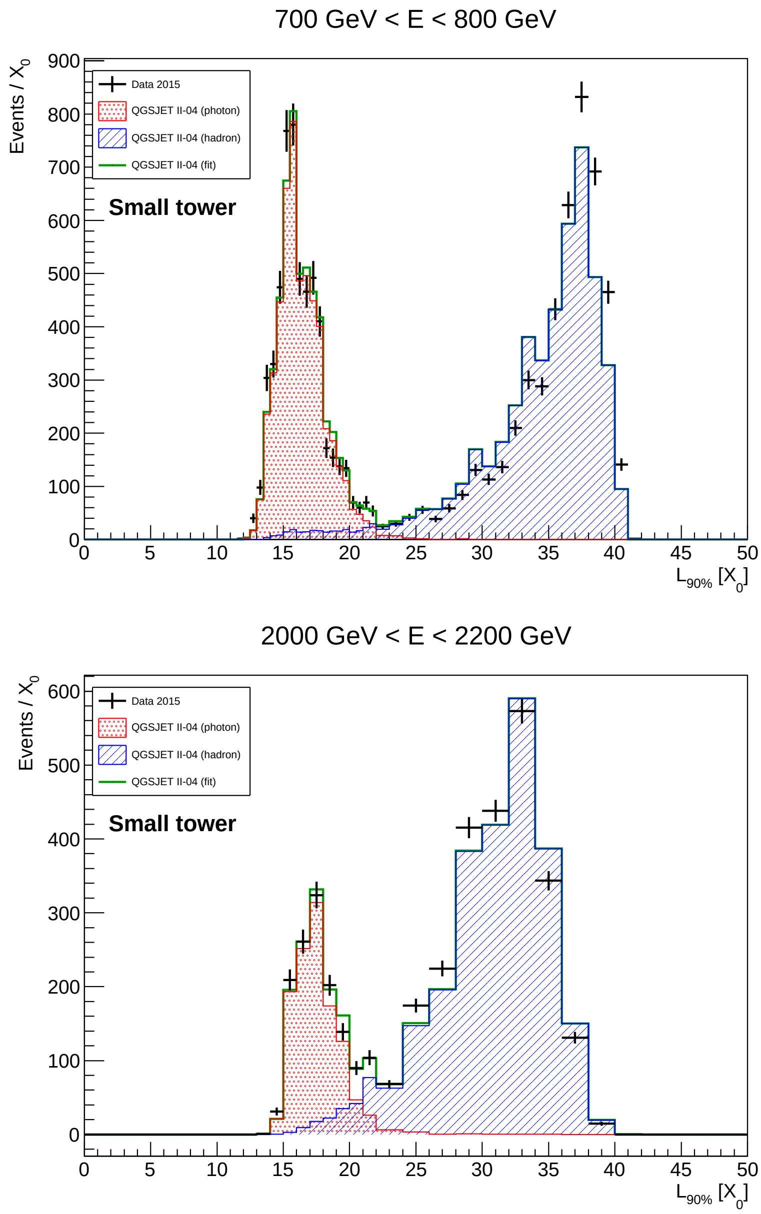

Figure 5.8: Comparison between best-fit template $L_{90\%}$ distribution and data of small tower in two different energy bins. Red and blue filled histograms represent photon and hadron distribution, respectively, green histogram shows the sum of the two above components and black points represent data.

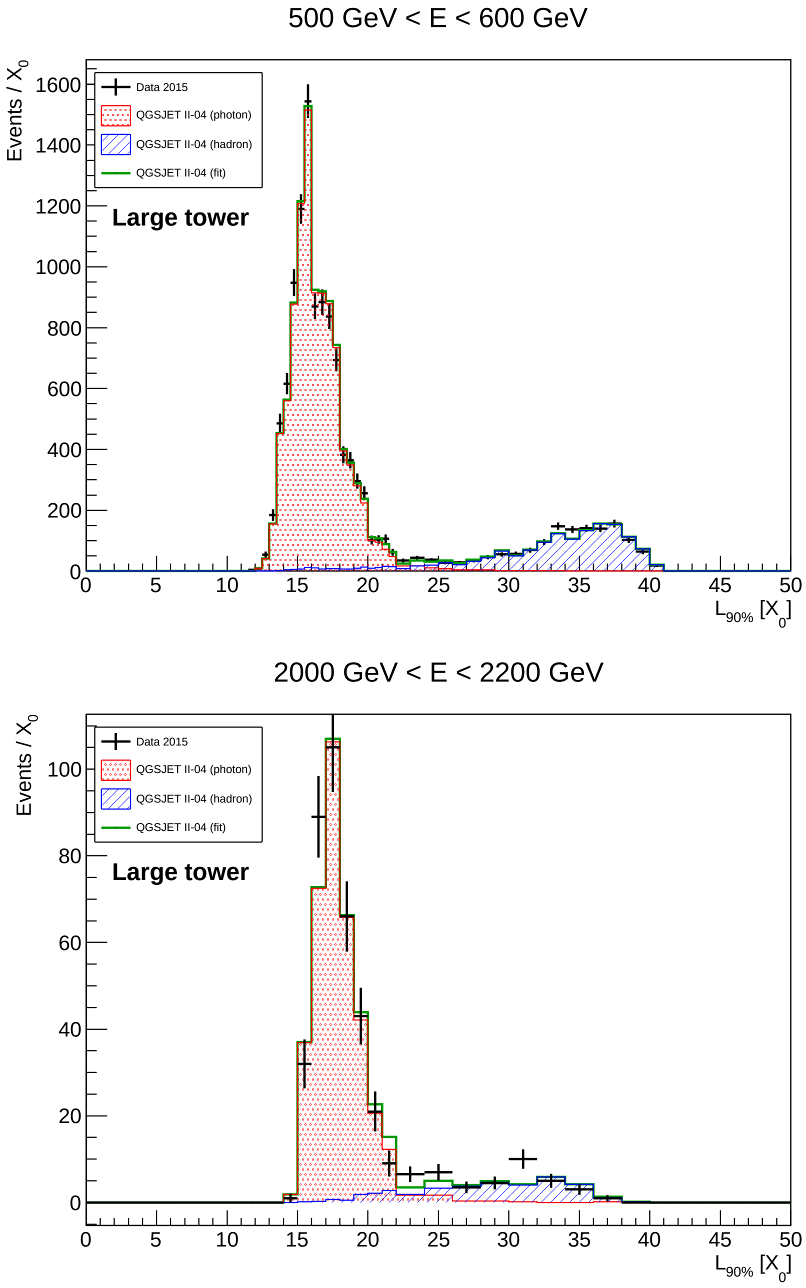

Figure 5.9: Comparison between best-fit template $L_{90\%}$ distribution and data of large tower in two different energy bins. Red and blue filled histograms represent photon and hadron distribution, respectively, green histogram shows the sum of the two above components and black points represent data.

the true value of p was unknown, the Bayes theorem was used to obtain the probability density of the real value of p once k and m are known. Assuming a prior probability of p uniform in the range $0 < p < 1$, the probability density of p was calculated:

$$Prob(p|m,k) = Z(m,k)\ p^k (1-p)^{(m-k)} \tag{5.11}$$

where $Z(m,k)$ is a normalisation constant only dependent on k and m [52]. The likelihood function was defined as

$$\begin{split} &L(N_{obs}|N_{corr}, \epsilon, P) = \\ &\qquad Prob(N_{obs}|N_{corr}, \epsilon, P) \cdot Prob(\epsilon|n_{gg}, n_{gh}) \cdot Prob(P|n_{gg}, n_{hg}) \end{split} \tag{5.12}$$

Substituting the results from equations 5.9 and 5.11 into equation 5.12, the log-likelihood ratio was constructed:

$$\begin{split} \chi^2 =& -2\log(\frac{L}{L_0}) \\ =& \ 2\left[(N_{corr} \cdot \epsilon \cdot P^{-1} - N_{obs}) - N_{obs} \log\left(\frac{N_{corr} \cdot \epsilon \cdot P^{-1}}{N_{obs}}\right)\right] \\ & - 2\left[n_{gg} \log\left(\frac{\epsilon}{\epsilon_0}\right) + n_{gh} \log\left(\frac{1-\epsilon}{1-\epsilon_0}\right)\right] \\ & - 2\left[\alpha n_{gg} \log\left(\frac{P}{P_0}\right) + \beta n_{hg} \log\left(\frac{1-P}{1-P_0}\right)\right] \frac{n_{gg} + n_{hg}}{\alpha n_{gg} + \beta n_{hg}} \end{split} \tag{5.13}$$

where ϵ_0 and P_0 are the efficiency and purity estimated from equations 5.4 and 5.8, respectively, L_0 is the likelihood function calculated substituting ϵ and P for ϵ_0 and P_0 in equation 5.12, and in the last term the normalisation of the template histogram was taken into account. Then, a fit with N_{corr}, ϵ and P treated as free parameters was done to minimise the χ^2 of equation 5.13 and to get the best estimation of N_{corr} and its confidence interval. Finally, the PID-corrected energy spectrum was constructed using the best-fit N_{corr} value found in each energy bin and the 1-σ confidence interval was assigned as the statistical error of each point. The best-fit values of efficiency and purity are shown in figure 5.10. The comparison between the spectrum before and after the PID correction is shown in figures 5.11 and 5.12.

5.5 Unfolding of the measured spectrum

The true energy spectrum of photons incident on the calorimeters is distorted because of the finite energy resolution of the detector and by the effects of

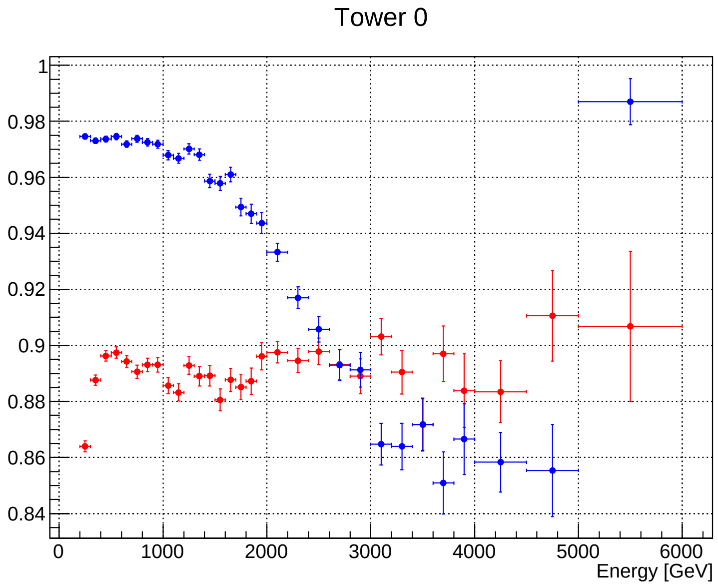

(a) Small tower

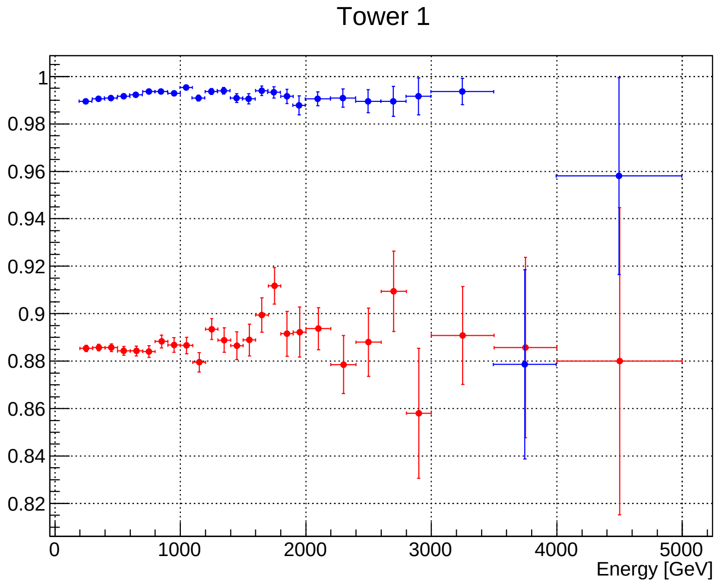

(b) Large tower

Figure 5.10: Efficiency (red points) and purity (blue point) resulting from the template fit in each energy bin.

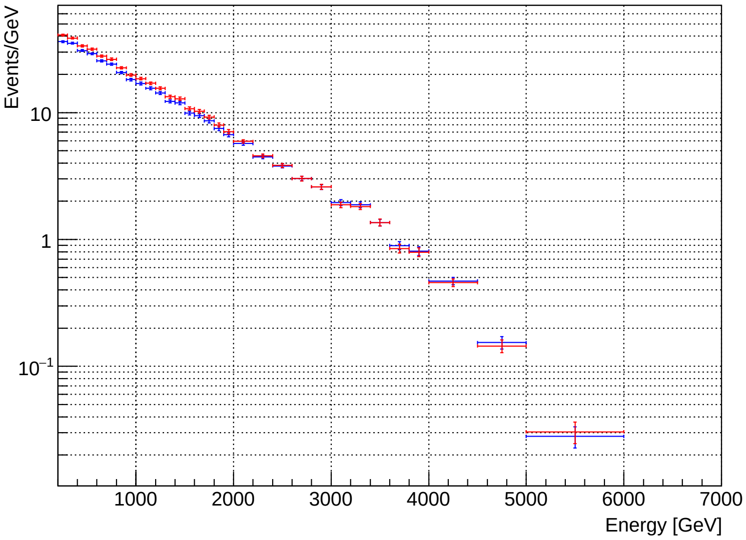

(a) Small tower

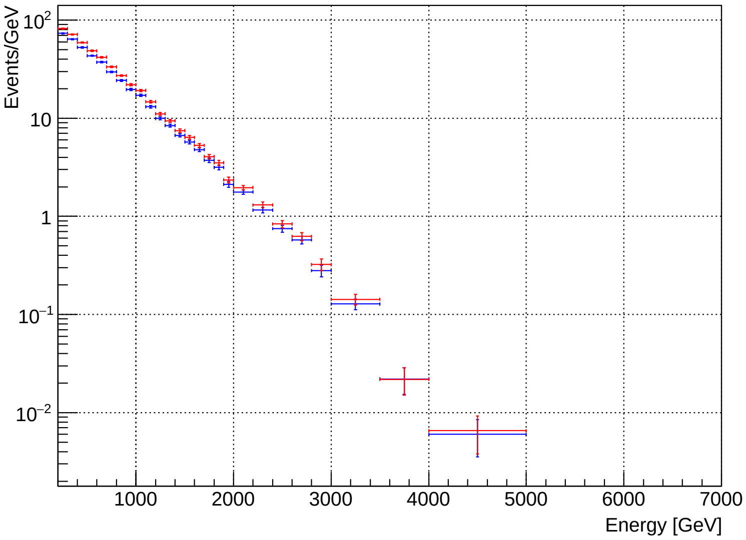

(b) Large tower

Figure 5.11: Comparison between the photon energy spectrum of both towers before and after the PID correction drawn as blue and red points, respectively. Only statistical error are displayed.

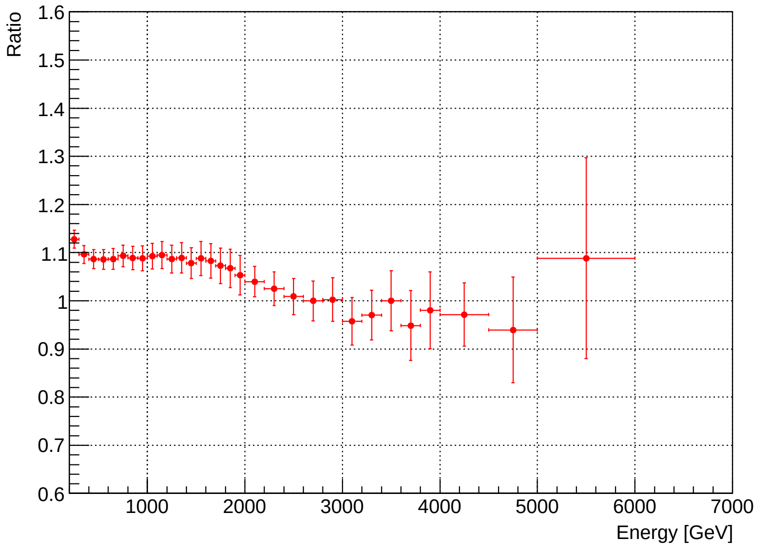

(a) Small tower

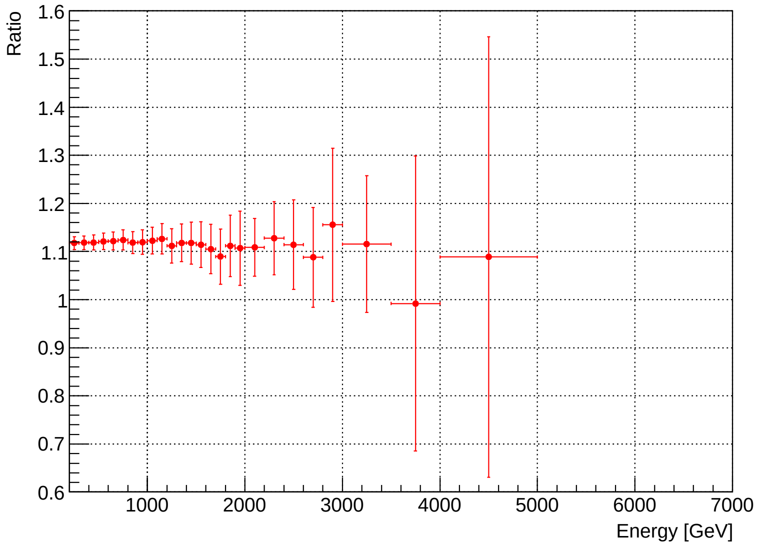

(b) Large tower

Figure 5.12: Ratio between the spectrum after and before the PID correction for both towers.

event selection criteria. The correction for the PID selection was already described in section 5.4. Energy resolution and the distortion coming from the multi-hit cut were corrected using the unfolding technique described in this section. When considering a binned distribution, the response of the detector can be modelled by a "response matrix" which acts on the vector of the bin contents of the true distribution and transform it into the measured spectrum:

$$n(M_j) = \sum_j R_{ji} \cdot n(T_i) \tag{5.14}$$

where $n(M_j)$ is the content of the j-th bin of the measured spectrum, $n(T_i)$ is the content of the i-th bin of the true spectrum and R_{ji} is the response matrix. So, R_{ji} can be seen as the probability for an event falling in the i-th bin of the true spectrum to be observed in the j-th bin of the measured spectrum. Inverting R_{ji} is not a realistic option since it is not guaranteed that the inverse matrix exists and, even in case of a non-singular matrix, the obtained inverse matrix cannot distinguish statistical fluctuations from real fine structures of the spectrum. Other approaches are commonly used in order to overcome these problems.

The method used in this analysis was an iterative unfolding algorithm based on Bayes' theorem proposed by G. D'Agostini [53]. The conditional probability for a cause T_i to be true when the effect M_j is measured is, from Bayes' theorem,

$$P(T_i|M_j) = \frac{P(M_j|T_i)\ P_0(T_i)}{\sum_k P(M_j|T_k)\ P_0(T_k)} \tag{5.15}$$

where the conditional probability $P(M_j|T_i)$ can be identified as the response function R_{ji} and $P_0(T_i)$ is the prior probability for the cause T_i to happen. The expected number of events assigned to the cause T_i can be obtained as

$$n(T_i) = \frac{1}{\epsilon_i} \sum_j P(T_i|M_j)\ n(M_j) \tag{5.16}$$

where $n(M_j)$ is the number of measured events for the effect M_j and $\epsilon_i \equiv \sum_k P(M_k|T_i)$ is the efficiency to detect the cause T_i in at least one of the measured effects. This calculation was iterated substituting the prior $P_0(T_i)$ with the probability $P(T_i) = n(T_i)/\sum_k n(T_k)$ resulting from the previous step of the iteration. The response function $P(M_j|T_i)$ can be estimated with a Monte Carlo simulation of the detector response. The choice of the first prior $P_0(T_i)$ depends on the information available on the true distribution; in case there are no hypothesis about the true distribution an uniform distribution can be used. In principle, the agreement will increase with the number of iteration and the unfolding matrix $P(T_i|M_j)$ will approach the inverse matrix. A finite number of iterations is then fixed in order to avoid the problems mentioned above when using directly the inverse matrix.

The unfolding of the LHCf photon energy spectrum was performed using the RooUnfold framework [54]. The response function was generated using the sample of QGSJET 10^8 events ("training" sample) that was used in section 5.4 for the template fit. The first prior was set as the QGSJET spectrum in order to have a prior closer to the real data distribution than an uniform distribution. The response function was built as a two-dimensional histogram with the measured energy and true energy as X and Y axes. For each event of the training sample, the histogram was filled with the appropriate measured and Monte Carlo truth energies in order to account for the resolution of the detector. Photons in a multi-hit event that had to be included in the spectrum (i.e., that satisfied all the other event cuts) were considered as "missed" events due to the limited efficiency of the detector (the ϵ_i present in equation 5.16). Also single-hit events misidentified as multi-hit events were included in missed events. Multi-hit events misidentified as a single photon were considered as background ("fake" events), to be subtracted from the measured spectrum. The calculated response function for both towers is shown in figure 5.13. The contributions of missed and fake events are shown instead in figures 5.14 and 5.15.

The criterion used to choose the number of iterations was based on the comparison between the unfolded spectrum after each step with the one from the previous step. Iteration was stopped when the χ^2 value of the comparison between the two spectra was of the order of ∼1. Further iterations would not improve significantly the unfolded spectrum, but statistics fluctuations would be emphasised. Unfolded spectra for both small and large tower compared with measured ones are shown in figures 5.16 and 5.17. The estimation of the systematic uncertainties associated to the spectrum resulting after the unfolding will be discussed in section 5.6. Finally, the spectrum will be compared with the predictions of Monte Carlo generators in section 5.7.

5.6 Systematic uncertainties

The main contributions to the systematic uncertainty of the energy spectrum are discussed in this section. The description of each source which contributes to the systematic error of the measured spectrum is given in sections 5.6.1-5.6.5. The calculation of the total systematic uncertainty is described in section 5.6.6.

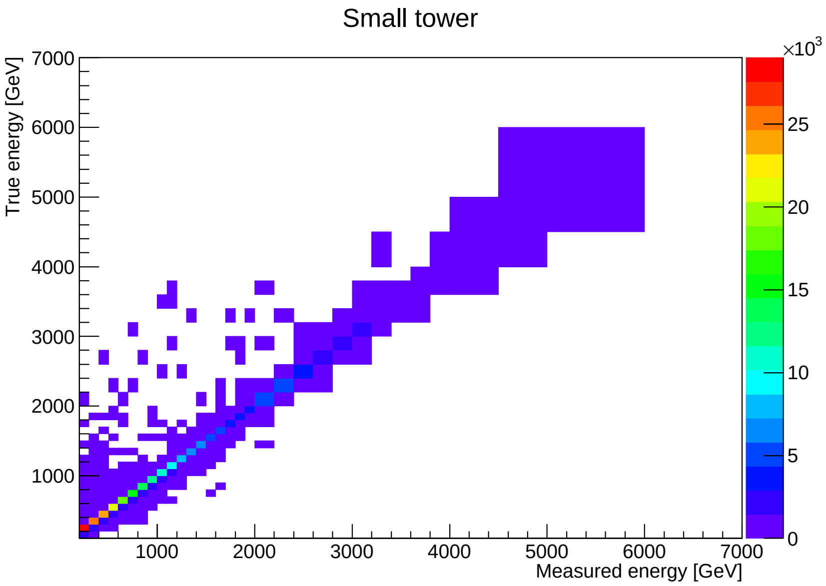

(a) Small tower

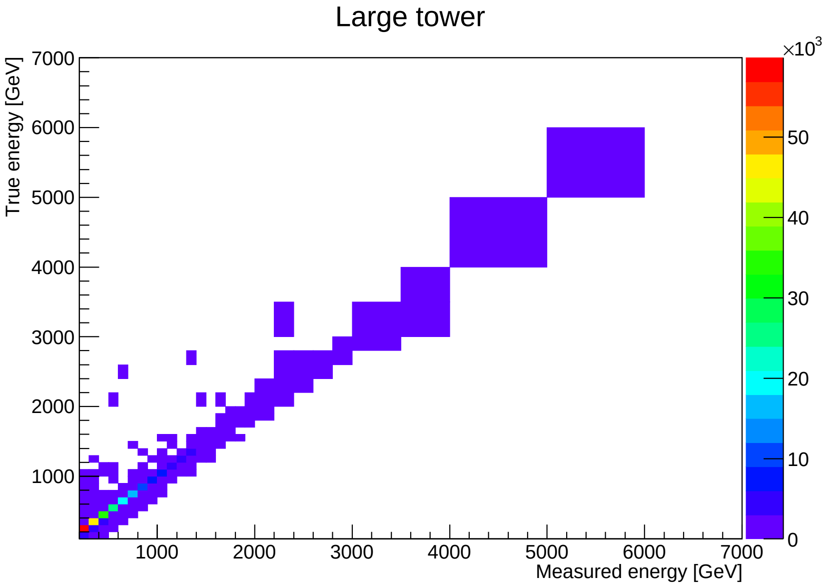

(b) Large tower

Figure 5.13: Response function of small tower and large tower generated with 10^8 events of the QGSJET training sample.

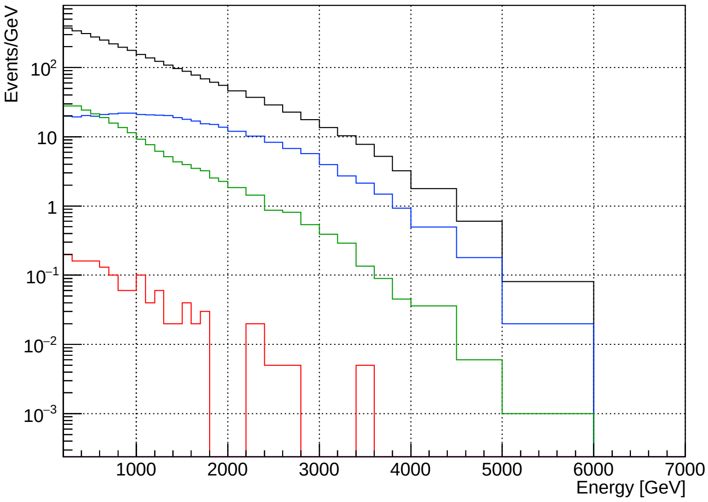

(a) Small tower

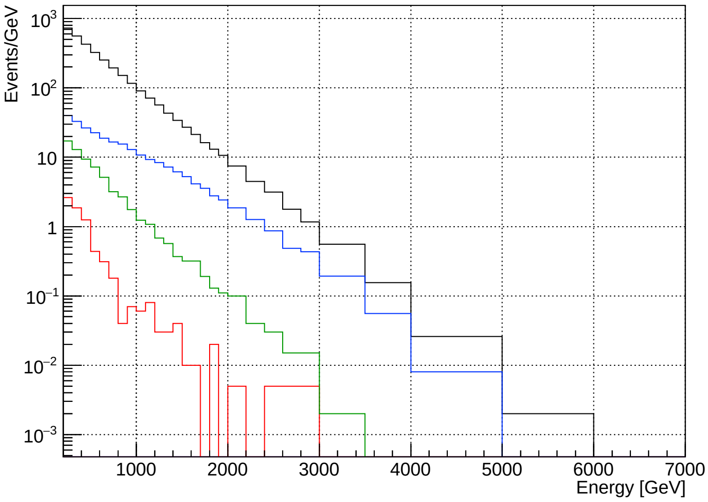

(b) Large tower

Figure 5.14: Contribution of missed events compared with the true spectrum (black): photon-photon multi-hit (blue), photon-hadron multi-hit (green) and single photon misidentified as multi-hit (red). The dominant contribution comes from photon-photon event for both tower, except the very low energy region of small tower where photon-hadron events give the main contribution. Misidentified single-hit photons give a negligible contribution.

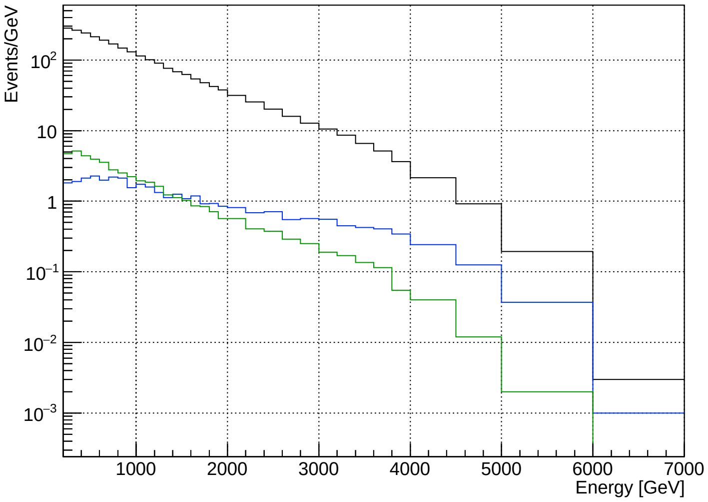

(a) Small tower

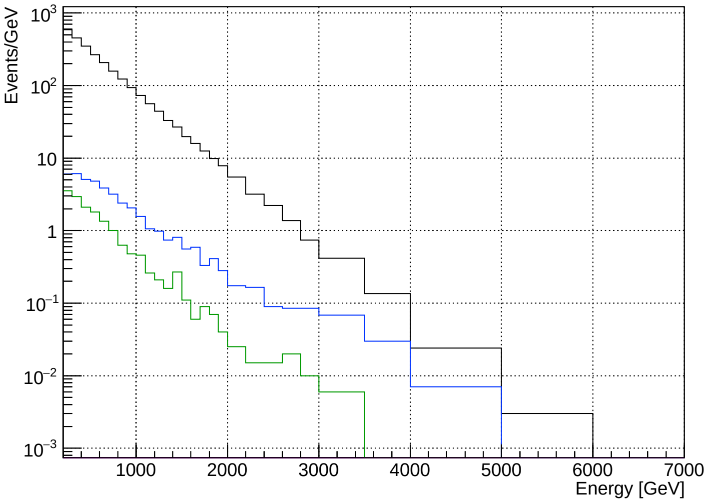

(b) Large tower

Figure 5.15: Contribution of fake events compared with the measured spectrum (black): photon-photon multi-hit (blue), photon-hadron multi-hit (green). The dominant contribution comes from gamma-gamma event for both tower, except the low energy region of small tower where gamma-hadron events give the main contribution.

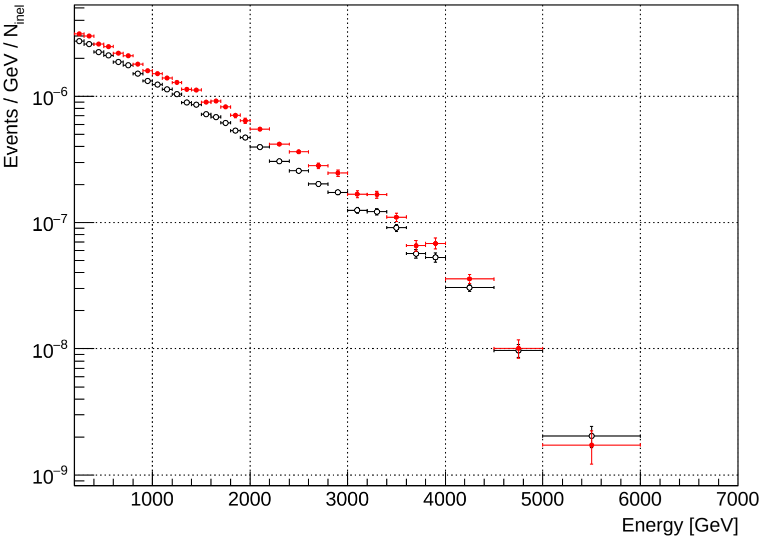

(a) Small tower

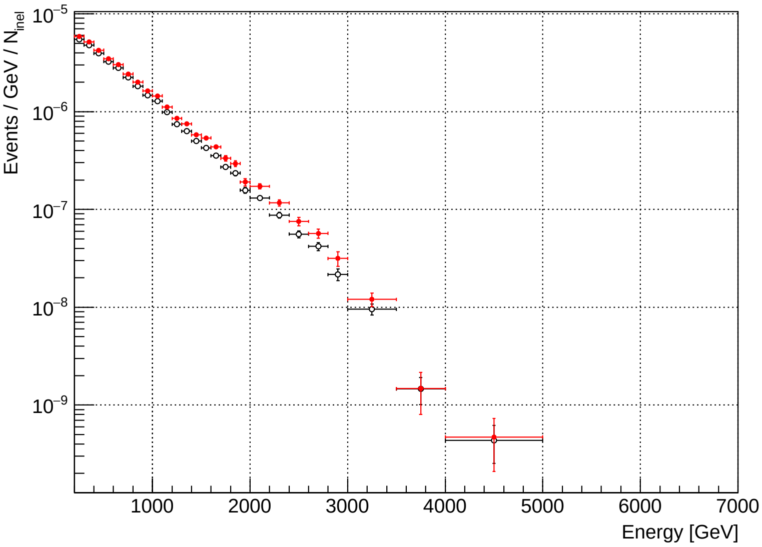

(b) Large tower

Figure 5.16: Comparison between the measured spectrum (black points) and the unfolded spectrum (red points) for both the small and large tower. Spectra are normalised to the number of inelastic collisions.

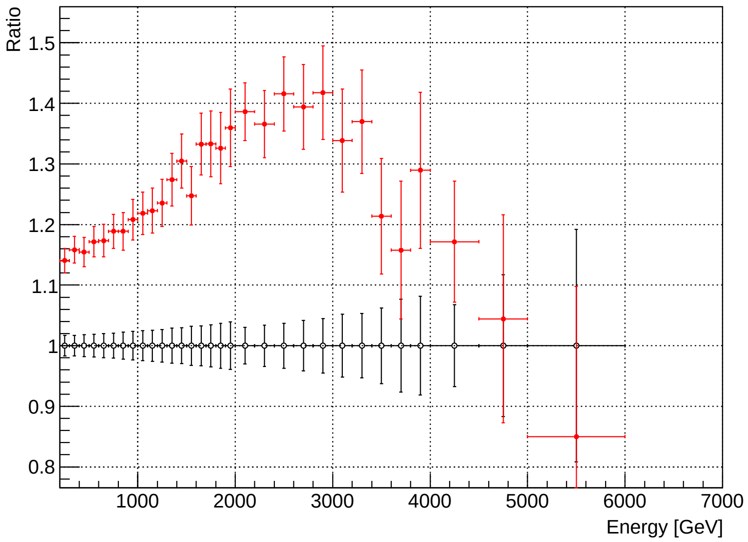

(a) Small tower

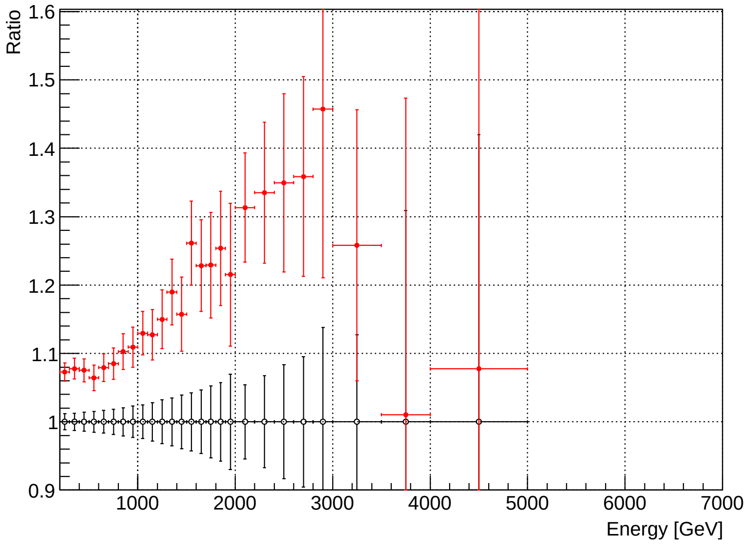

(b) Large tower

Figure 5.17: Ratio between the spectrum after (red points) and before (black points) the unfolding for both the small and large tower.

5.6.1 Energy scale

The contribution to the error from the measurement of conversion factors and of the position dependence of signal in the calorimeter were already studied in section 4.5. A summary of other contributions to the energy scale are listed below. The determination of the magnitude of these errors was not a part of this work, so only a brief description of the source of the uncertainty is given [55].

- PMT gain table: error on the measurement of the relation between the high voltage and the gain of the PMTs. The measurement was done using a calibration laser, whose pulse was brought to each PMT inside the detector through several optical fibres.
- Non-uniformity: error from the position dependence of the signal described in section 4.5.2.
- Conversion factors: error on the conversion factors measurements described in section 4.5.1.
- LPM effect (calibration): the effect of the Landau–Pomeranchuk–Migdal (LPM) effect, which reduces the pair production cross section of high energy photons [56,57], on the determination of conversion factors. The error were estimated comparing the energy deposit in each layer of simulations with and without including the LPM effect. The simulations used in calibration previously described in section 4.3.1 included the LPM effect.
- LPM effect (Sum-dE): how the LPM effect modifies the relation between Sum-dE and energy. Since the Sum-dE was obtained summing the energy deposit until enough deep layers, this contribution is rather small. The relation described in equation 3.1 was obtained including the LPM effect in simulations.
- H.V. table: error on the calculated PMT gain due to the uncertainty on the measured high voltage.
- Cable attenuation: error on the measurement of the attenuation factor of the 200 meters long cable that bring the analog signal of PMTs to the ADCs. This factor was measured at the SPS beam test using a replica of the 200 meters long cable used at LHC.
- ADC linearity: error due to the deviation from linearity of the ADCs that digitize PMTs analog signal.

- Temperature correction: error associated to the estimation of the temperature correction of PMTs gain. The relative variation of the gain $\Delta G/G$ is related to the variation of temperature ΔT by the relation $\Delta G/G = A_T \cdot \Delta T$, where A_T is a constant coefficient different for each PMT. The conversion factors obtained at the beam test at SPS were corrected for the mean difference of temperature with respect to the LHC tunnel. A_T was measured analysing the temperature dependence of the calibration laser signal. Typical values of A_T are around $-0.5\%/°\mathrm{C}$. This error includes both the error on A_T itself and the error on the measurement of the temperature.

All the contributions from the above errors are listed in table 5.2. The total energy scale error was estimated as the quadratic sum of all the contributions, resulting as 2.7%. The π^0 mass shift described in section 5.2.2 was found to be 1.6%, so it is consistent with the absolute energy scale systematic error.

Source	**Error**
PMT gain table	1.8%
Non-uniformity	1.1%
LPM effect (calibration)	1.0%
Conversion factors	0.8%
LPM effect (Sum-dE)	0.7%
H.V. table	0.7%
Cable attenuation	0.5%
ADC linearity	0.1%
Temperature correction	0.1%
Total energy scale error	2.7%

Table 5.2: Summary of all the contributions to the systematic error of the energy scale. The total error is calculated as the quadratic sum of all the errors.

The systematic uncertainty associated to the spectrum was obtained scaling the energy of each event by ±2.7% and comparing the scaled spectra to the original one. The ratio between the scaled spectra and the original spectrum is shown in figure 5.18. Instead of assigning the systematic error as the deviation obtained in each energy bin, which is subject to statistical fluctuations, the systematic error was assigned as a broken linear function with different slopes reproducing the trend of the deviations from the original spectrum (dashed green line in figure 5.18). This approach was used also for the other sources of systematic errors described in the next sections.

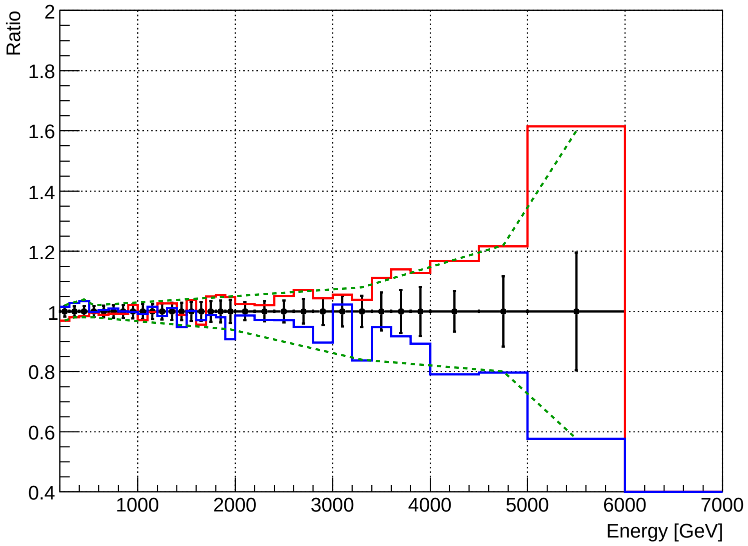

(a) Small tower

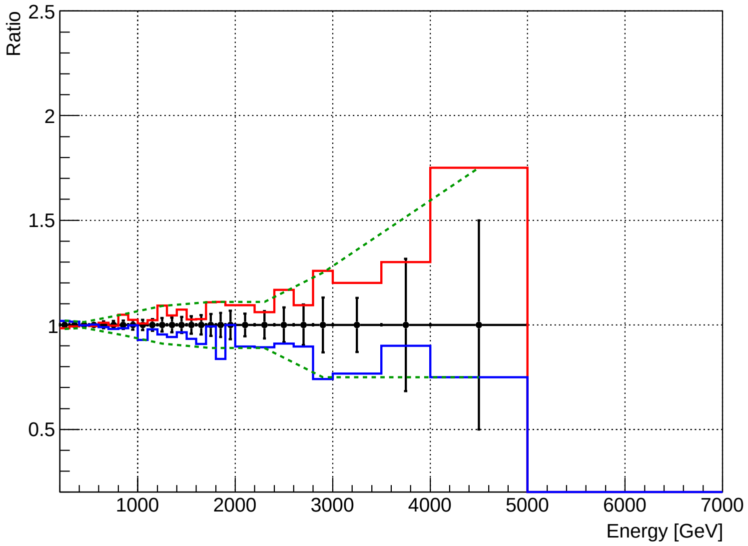

(b) Large tower

Figure 5.18: Ratio between the spectra obtained scaling the energy of each event by -2.7% and +2.7% (blue and red histogram, respectively) and the nominal spectrum (black points). The green dashed line represents the assigned systematic error. Statistical errors of the spectrum with the nominal energy scale are shown for reference.

5.6.2 Beam centre stability

The position of the beam centre affected the selection of the pseudorapidity region, so any uncertainty on the measurement of the beam centre induced a systematic error to the spectrum. Figure 5.19 shows the change of the measured beam centre position during fill #3855. Fluctuations were found to be of the order of ∼0.3 mm, greater than the precision of the mean beam centre measurement using all the data of the fill.

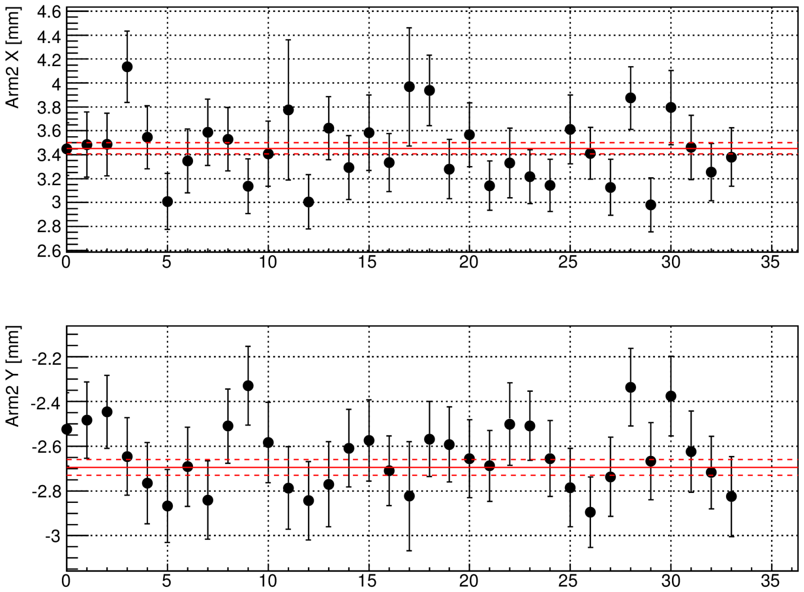

Figure 5.19: Fluctuation of the position of the beam centre along X and Y axis (in the upper and lower picture, respectively) as a function of time. Acquired data were divided in samples of ∼125000 triggered events and the fit on the beam centre was done for each sample. X or Y coordinate is reported in the vertical axis, while the horizontal axis reports the progressive number of the beam centre measurements. The red line represents the value measured using the all sample of data and dashed lines show the uncertainty of the fit.

The systematic error was estimated by artificially moving the position of the beam centre when calculating the pseudorapidity. Beam position was moved by ±0.3 mm on the X and Y axis and the spectra measured with the shifted position were compared to the original one. The ratio of the shifted spectra relative to nominal spectrum are shown in figure 5.20. The

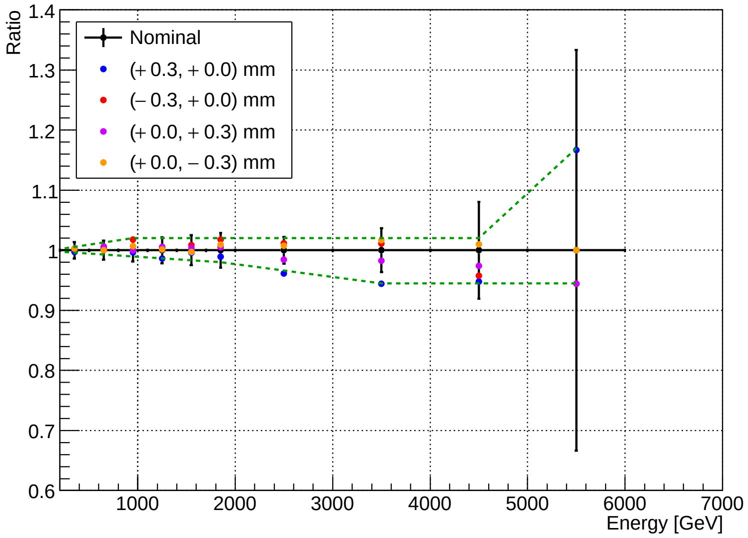

(a) Small tower

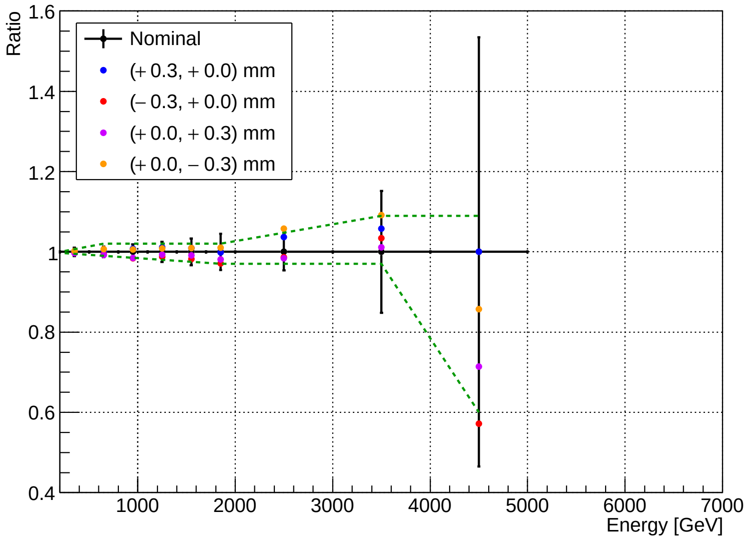

(b) Large tower

Figure 5.20: Ratio between the spectra obtained shifting artificially the beam centre (coloured points) and the nominal spectrum for both small and large tower (black points). Bigger bins were used to reduce statistical fluctuations. The green dashed line represents the assigned systematic error. Statistical errors of the spectrum in the nominal position are shown for reference.

shift toward the positive X axis for the small tower gave a more significant contribution compared to other directions, because it shifted the beam centre very near to the border of the calorimeter. The relative variation from the nominal spectrum was assigned as the systematic error associated to the beam centre determination.

5.6.3 PID correction

The systematic uncertainty associated to the PID correction was estimated changing the criterion for the choice of the threshold L_{thr} discussed in section 5.4. Instead of choosing L_{thr} to get a 90% photon selection efficiency, the PID selection and correction was also performed using the threshold values that gave 85% and 95% photon selection efficiency. The spectra after the correction were compared to obtain the uncertainty associated to the choice of the threshold L_{thr} in the PID correction method. The comparison between the spectra with different threshold is shown in figure 5.21. The systematic error was defined as the relative deviation from the standard spectrum.

5.6.4 Multi-hit detection efficiency

The unfolding process described in section 5.5 was used to correct the energy spectrum for the effect of the multi-hit cut, in addition to the energy resolution. If the efficiency of the detection of multi-hit events predicted by simulation is not consistent with the one obtained for experimental data a systematic error will arise since the number of fake events (i.e., multi-hit events misidentified as a single photon) will not be estimated correctly.

In order to estimate the multi-hit efficiency when analysing real data events, an “artificial” sample of multi-hit events was created merging two different single-hit measured events. In order to create a realistic sample of multi-hit, the two-dimensional distribution of the ratio between the two photon energies ($R_{21} \equiv E_2/E_1$, where E_1 and E_2 are the energies of the more and less energetic photon in a multi-hit, respectively) and the distance between the two peaks ($d_{21} \equiv \sqrt{(x_2 - x_1)^2 + (y_2 - y_1)^2}$, where $x_{1,2}$, $y_{1,2}$ are the coordinates of the two photons) in a multi-hit event was derived from the QGSJET training sample. The artificial sample was created coupling single-hit events according to the predicted R_{21}-d_{21} distribution. An artificial sample of multi-hit events was created with the same method also for a sample of QGSJET simulations in order to compare it with data without a bias due to the construction algorithm used to create the artificial sample.

The multi-hit detection efficiency was measured as the fraction of events properly recognised as multi-hit in the artificial sample. The comparison

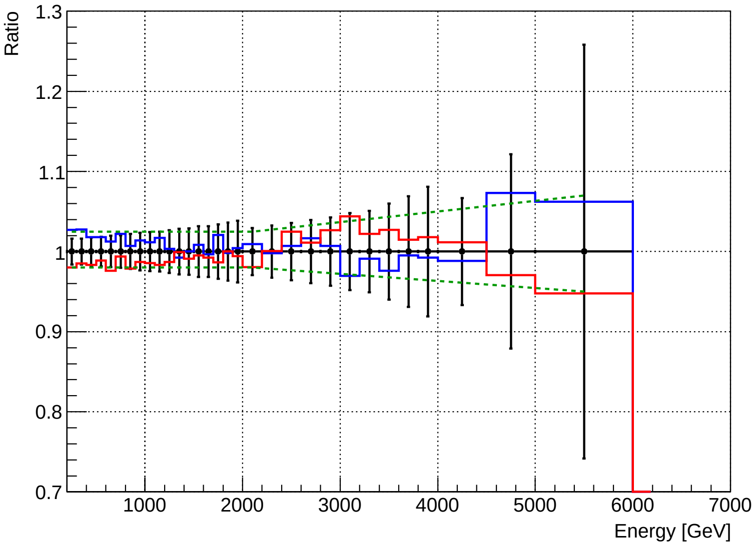

(a) Small tower

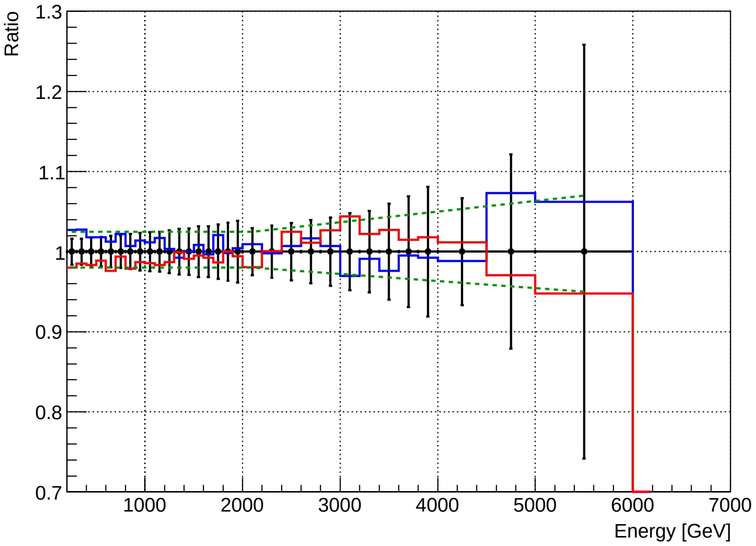

(b) Large tower

Figure 5.21: Ratio between the spectra obtained using 85% and 95% (blue and red histograms, respectively) photon selection efficiency for the choice of L_{thr} relative to the spectrum obtained using the standard value of 90% PID efficiency (black points). The green dashed line represents the assigned systematic error. Statistical errors of standard spectrum are shown for reference.

of the multi-hit detection efficiency between data and simulations is shown in figure 5.22. The systematic error on the multi-hit detection efficiency was estimated as the relative difference between the efficiency of data and simulation. The ratio of the efficiency between data and Monte Carlo is shown in figure 5.23.

Since $M_i = \epsilon_i \, M_i^{true}$, where M_i and M_i^{true} are the number of detected and true multi-hit, respectively, and ϵ_i is the multi-hit detection efficiency in the i-th energy bin, the relative systematic uncertainty of M_i is equal to the one of ϵ_i:

$$\frac{(\Delta M_i)^{sys}}{M_i} = \frac{(\Delta \epsilon_i)^{sys}}{\epsilon_i} \tag{5.17}$$

The number of single-hit event is, trivially, $S_i = N_i - M_i$ where N_i is the total number of event in the i-th energy bin, so the absolute systematic error on S_i is the same of M_i:

$$(\Delta S_i)^{sys} = (\Delta M_i)^{sys} \tag{5.18}$$

The relative error on S_i is therefore

$$\frac{(\Delta S_i)^{sys}}{S_i} = \frac{M_i}{S_i} \cdot \frac{(\Delta M_i)^{sys}}{M_i} = \frac{M_i}{S_i} \cdot \frac{(\Delta \epsilon_i)^{sys}}{\epsilon_i} \tag{5.19}$$

The relative systematic error in each bin content of the measured energy spectrum was therefore assigned as the relative error on the multi-hit detection efficiency multiplied by the ratio of multi-hit and single-hit events. The fraction of multi-hit events relative to the total ($\equiv M_i/(S_i + M_i)$) as a function of the energy is shown in figure 5.24. The systematic error calculated with equation 5.19 as a function of the energy is shown in figure 5.25.

5.6.5 Unfolding

The choice of the model for the construction of the response matrix of the unfolding gave two main sources of uncertainty:

- Choosing a different model, the prior probability used in the first step of the unfolding iteration changed.
- Different models predicted a different number of multi-hit events hitting the towers. Since the multi-hit cut was treated as an inefficiency of the detector, different models predicted a different number of missed event in the unfolding.

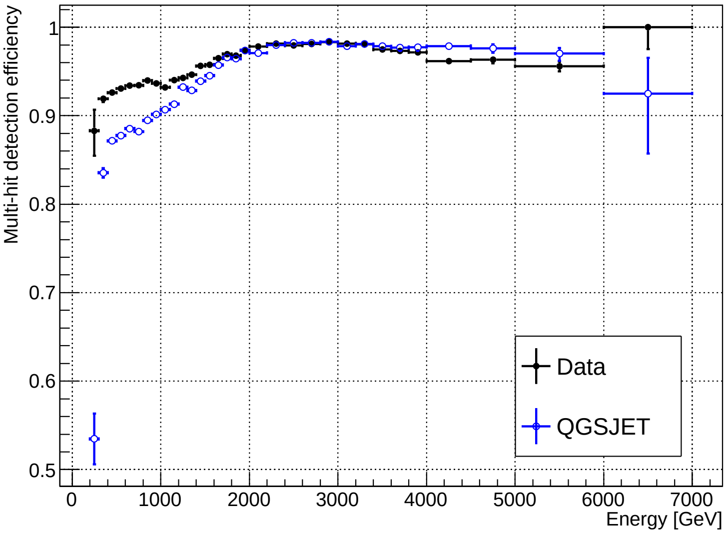

(a) Small tower

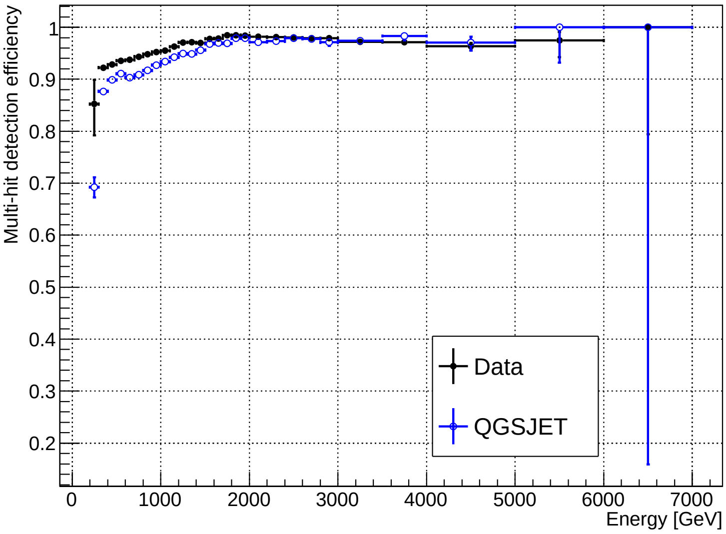

(b) Large tower

Figure 5.22: Comparison of multi-hit detection efficiency between data (black points) and simulation (blue points) as a function of the energy. The energy reported on the horizontal axis is the reconstructed energy of the event if it is misidentified as a single-hit.

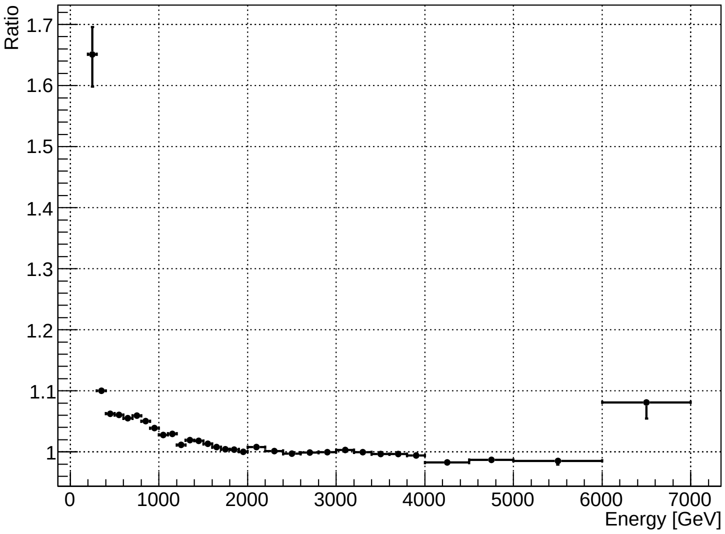

(a) Small tower

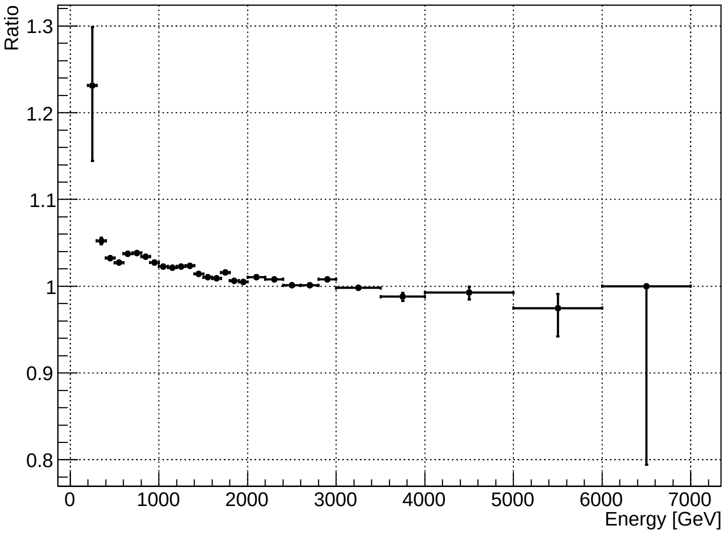

(b) Large tower

Figure 5.23: Ratio between the multi-hit detection efficiency found for data relative to simulation as a function of the energy. The energy reported on the horizontal X axis is the reconstructed energy of the event if it is misidentified as a single-hit.

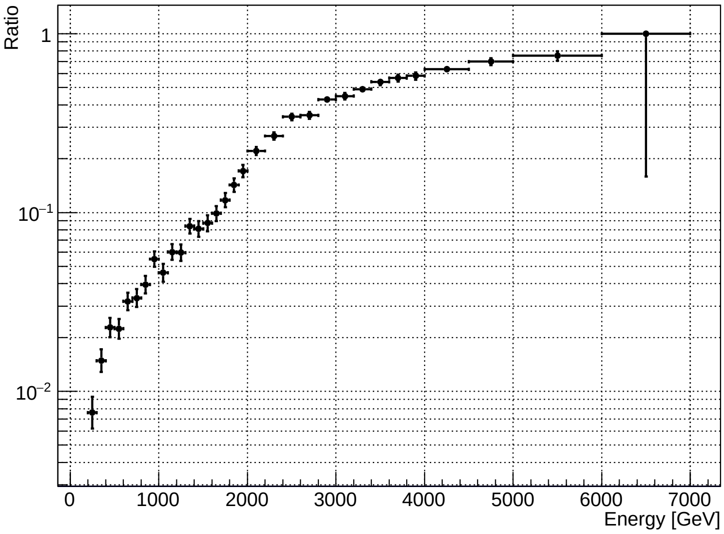

(a) Small tower

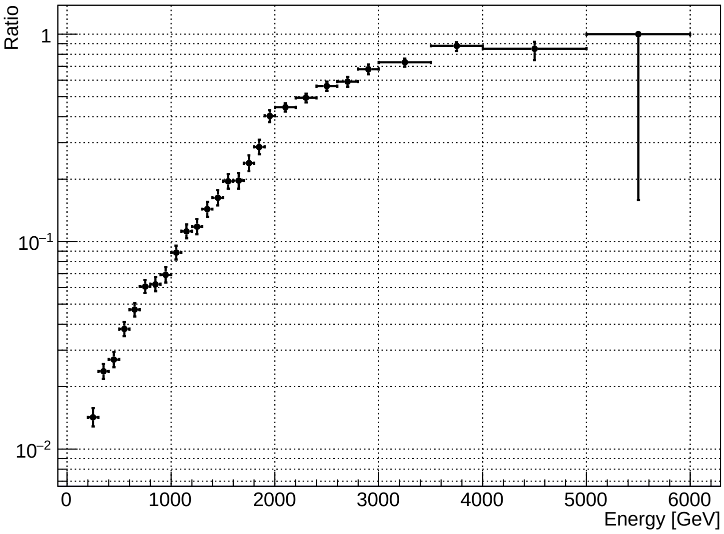

(b) Large tower

Figure 5.24: Fraction of detected multi-hit events with respect to the total number of events in each energy bin of data spectrum for both towers.

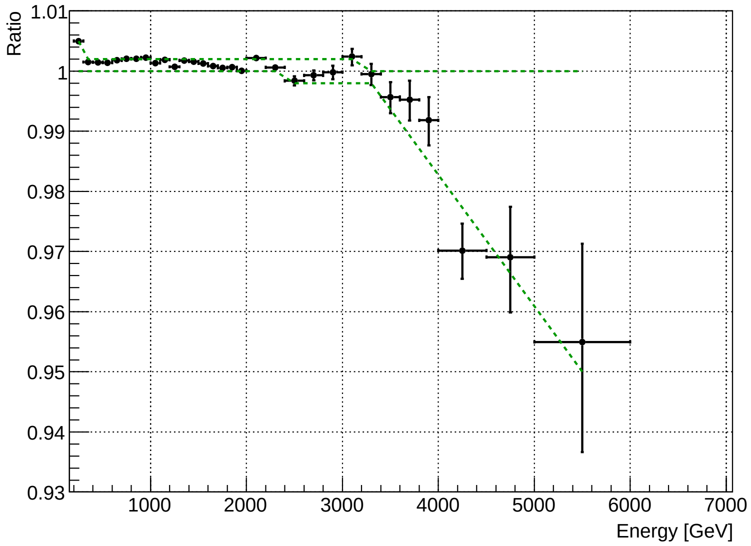

(a) Small tower

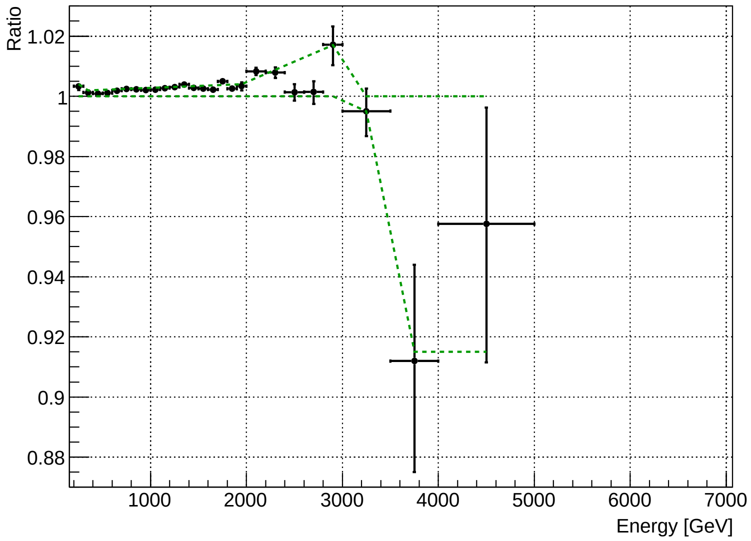

(b) Large tower

Figure 5.25: Systematic error associated to the energy spectrum form the multi-hit efficiency contribution calculated with equation 5.19. The green dashed line represents the assigned systematic error.

Two response matrices were generated with QGSJET and EPOS models in order to estimate the model dependence of the unfolding result. In figure 5.26 the comparison between the unfolded spectra obtained using the response matrix calculated with QGSJET and EPOS is shown. The ratio between the two spectra is shown instead in figure 5.27. The relative difference between QGSJET and EPOS results was chosen as the systematic error associated to the unfolding.

In order to check which is the main contribution to this uncertainty, the contribution of the multi-hit cut to the spectrum was studied. Figure 5.28 shows the ratio between the true spectrum predicted by QGSJET and EPOS simulations and the same spectrum after applying the multi-hit cut with the same reconstruction algorithm used for data. This ratio can be seen as a “multi-hit correction” to convert the reconstructed spectrum to the true one. Since the aim of unfolding was to estimate the true spectrum from the reconstructed one, the ratio between the spectrum before and after unfolding was expected to be similar to the multi-hit correction. The above statement is valid within the statistical uncertainties, as can be confirmed by comparing the multi-hit correction of QGSJET with the ratio shown in figure 5.17. The model dependence of the multi-hit correction is shown in figure 5.29, where the ratio between the QGSJET and EPOS-based corrections is presented. Comparing it with the ratio shown in figure 5.27, the two ratios are consistent until an energy of 4 TeV, so the uncertainty in this energy range is dominated by the multi-hit uncertainty. For higher energies the ratios are not consistent, so the uncertainty can not be explained as coming only from the multi-hit contribution. The discrepancies can be both due to the statistical fluctuations and because of the different prior probability of the two models used in the unfolding process.

5.6.6 Total systematic uncertainty

The total systematic uncertainty was evaluated considering all the contributions described in sections 5.6.1-5.6.5. In each energy bin all the contributions to the systematic uncertainty were quadratically summed. The individual contribution of each source of systematic error as a function of the energy is shown in figure 5.30.

5.7 Analysis results and comparison with MC

The spectrum before the unfolding, but after the PID correction, was compared with the prediction of simulations which include the propagation from

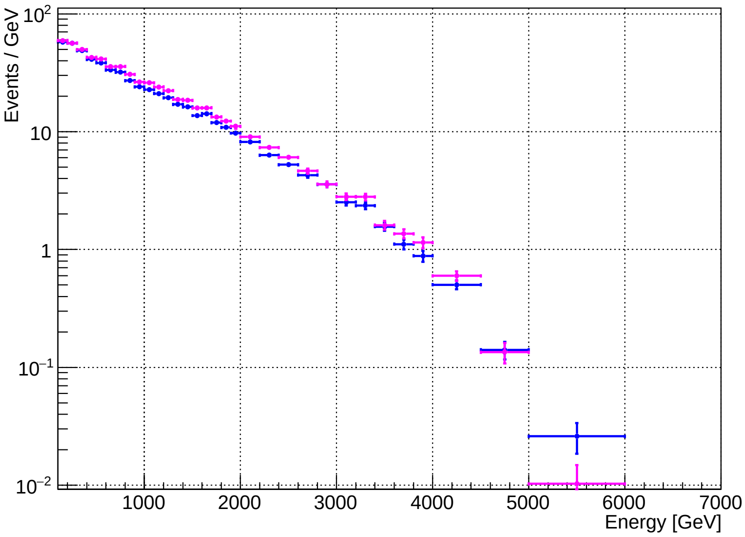

(a) Small tower

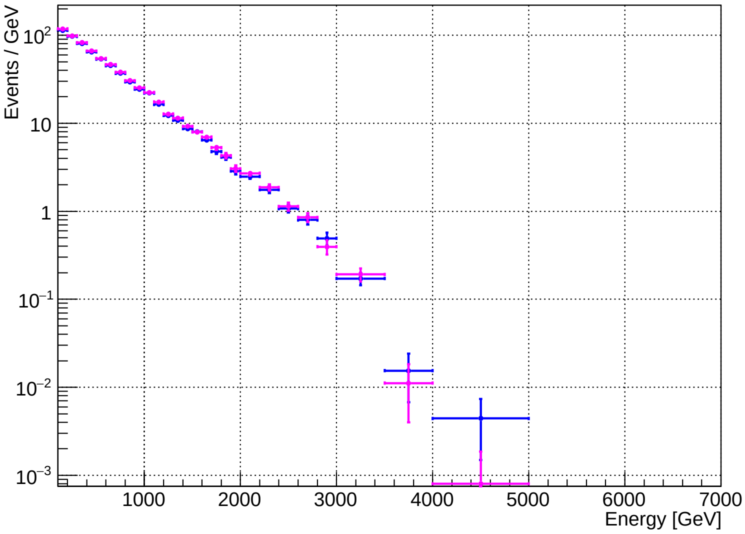

(b) Large tower

Figure 5.26: Unfolded spectra using QGSJET and EPOS response matrices represented as blue and magenta points, respectively.

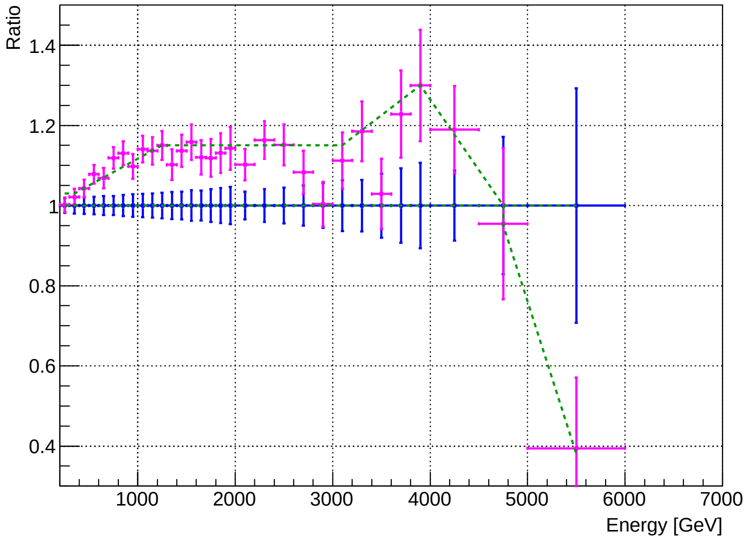

(a) Small tower

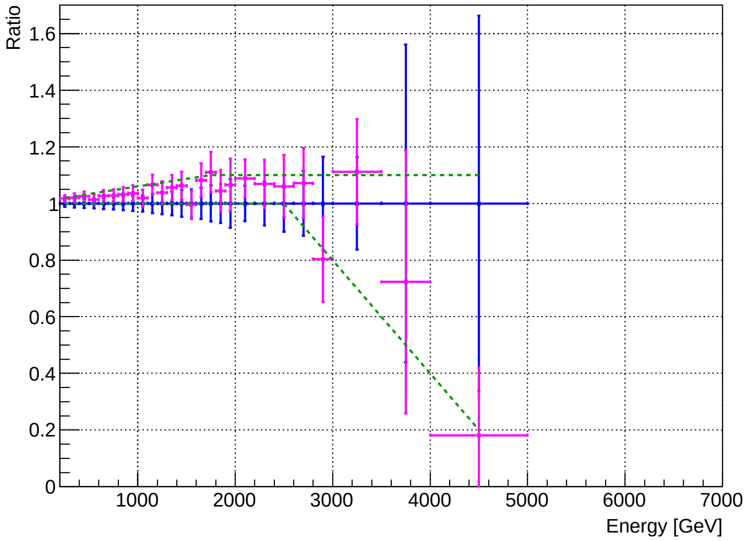

(b) Large tower

Figure 5.27: Ratio between the unfolded spectra using QGSJET (blue) and EPOS (magenta) response matrices. The green dashed line represents the assigned systematic error.

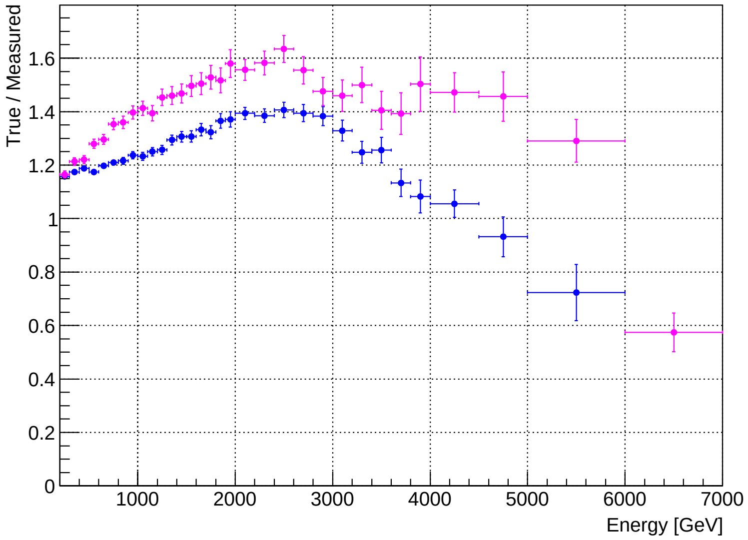

(a) Small tower

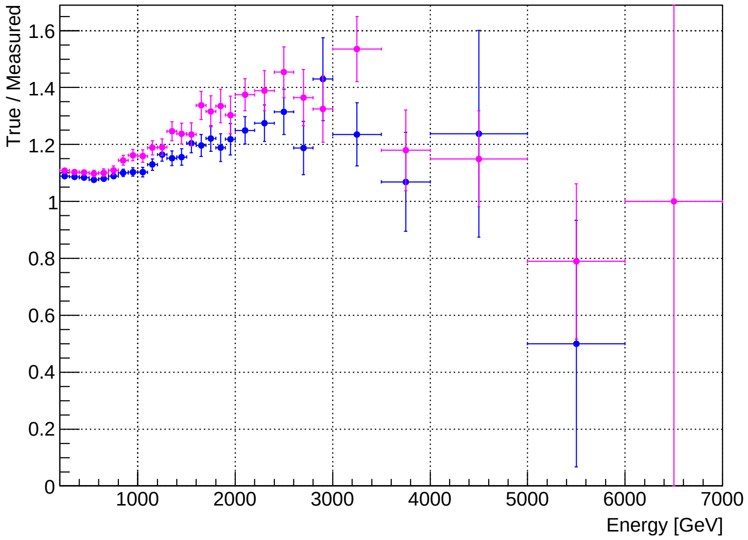

(b) Large tower

Figure 5.28: Ratio between the true spectrum (from Monte Carlo truth) and the measured spectrum after applying the multi-hit cut. The ratio predicted by QGSJET simulations is shown as blue points, while EPOS results are shown as magenta points.

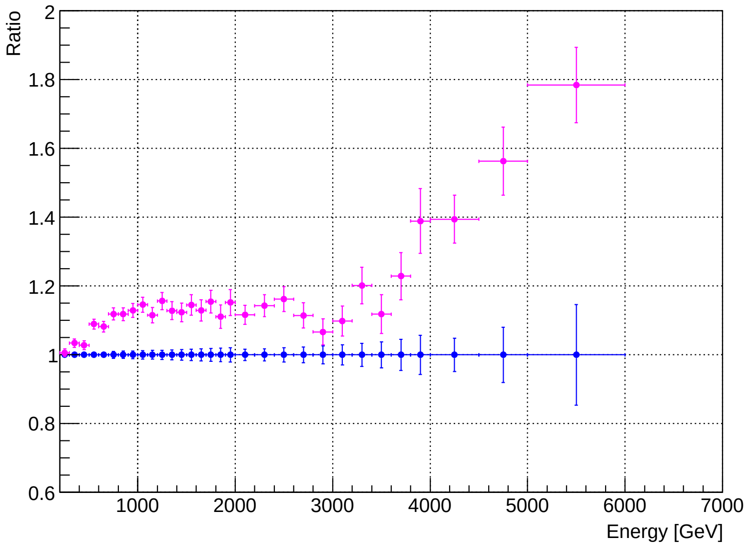

(a) Small tower

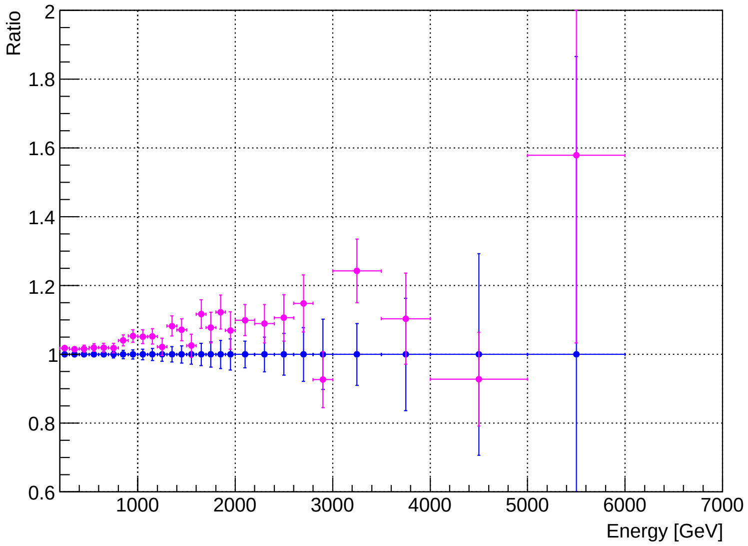

(b) Large tower

Figure 5.29: Ratio between the multi-hit efficiency calculated with QGSJET (blue) and EPOS (magenta) models.

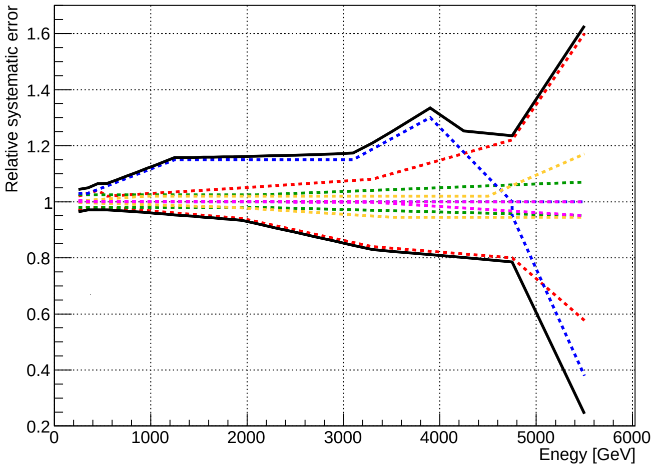

(a) Small tower

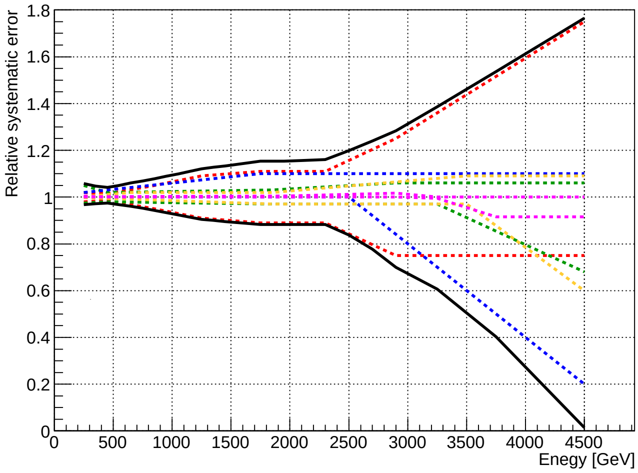

(b) Large tower

Figure 5.30: Individual contributions to the systematic errors as a function of the energy are shown as coloured lines: energy scale (red), beam centre (yellow), PID correction (green), multi-hit efficiency (magenta) and unfolding (blue). The total systematic error is plotted as a black line.

the interaction point to the TAN region and the interaction with the detector. The measured Arm2 spectrum compared with the predictions of DPMJET, EPOS and QGSJET is shown in figures 5.31 and 5.32 for the small and large tower, respectively.

In the pseudorapidity range $\eta > 10.94$, QGSJET presents a good overall agreement with experimental data, while EPOS predict a lower yield. DPMJET has a good agreement with data below 2.5 TeV, while it is harder than data at higher energies. In the pseudorapidity range $8.81 < \eta < 8.99$, DPMJET and EPOS spectra agree with data until ∼3 TeV, while they become harder at higher energies; QGSJET presents generally a lower yield of photons.

Since the spectrum after the unfolding is corrected for the detector response and the multi-hit cut, it was possible to directly compare the unfolded spectrum with the prediction of Monte Carlo generators, without propagating the secondary particles through the beam pipe and the detector. 10^8 proton-proton collisions at $\sqrt{s} = 13$ TeV were simulated with DPMJET, QGSJET, SIBYLL, EPOS and PYTHIA models using the Cosmic Ray Monte Carlo (CRMC [58]) package. The final Arm2 spectrum compared with generators predictions is shown in figures 5.33 and 5.34 for the small and large tower, respectively.

In the pseudorapidity range $\eta > 10.94$, QGSJET and EPOS presents a good overall agreement with experimental data; PYTHIA spectrum agrees with data until ∼3.5 TeV but become harder at higher energies; DPMJET is generally harder than data while SIBYLL predicts a lower yield of photons over all the energy range. In the pseudorapidity range $8.81 < \eta < 8.99$, EPOS and PYTHIA spectra agree with data until ∼3 TeV, while they become harder at higher energies; QGSJET presents a lower yield of photons, while the other models generally predict an harder spectrum than experimental data. Even if there is not an unique model that well reproduces experimental data over all the energy range, measured data lie between the predictions of all the models.

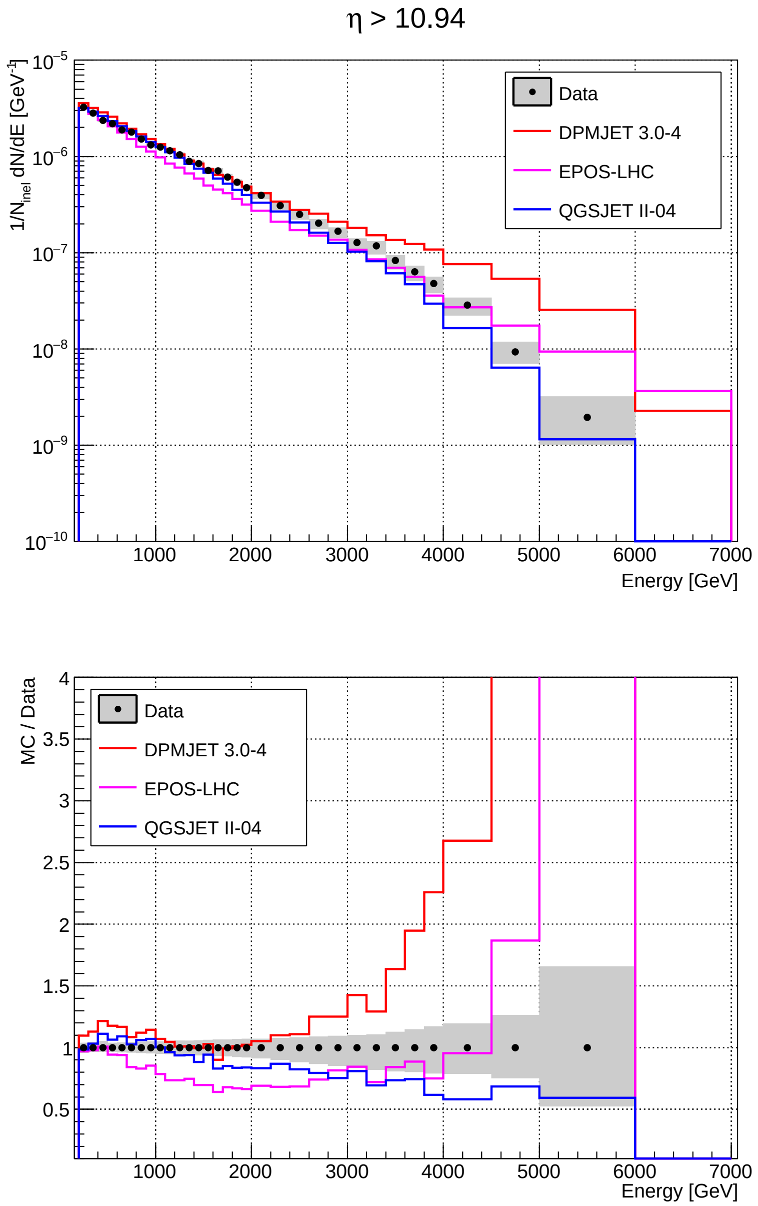

Figure 5.31: In the top picture, spectrum measured by the Arm2 small tower of LHCf before the unfolding (black points) compared with simulations propagated into the detector: DPMJET (red), QGSJET (blue) and EPOS (magenta). Grey shaded area represents the total error (statistical and systematical) of measured spectrum. In the bottom picture the ratio relative to data is shown.

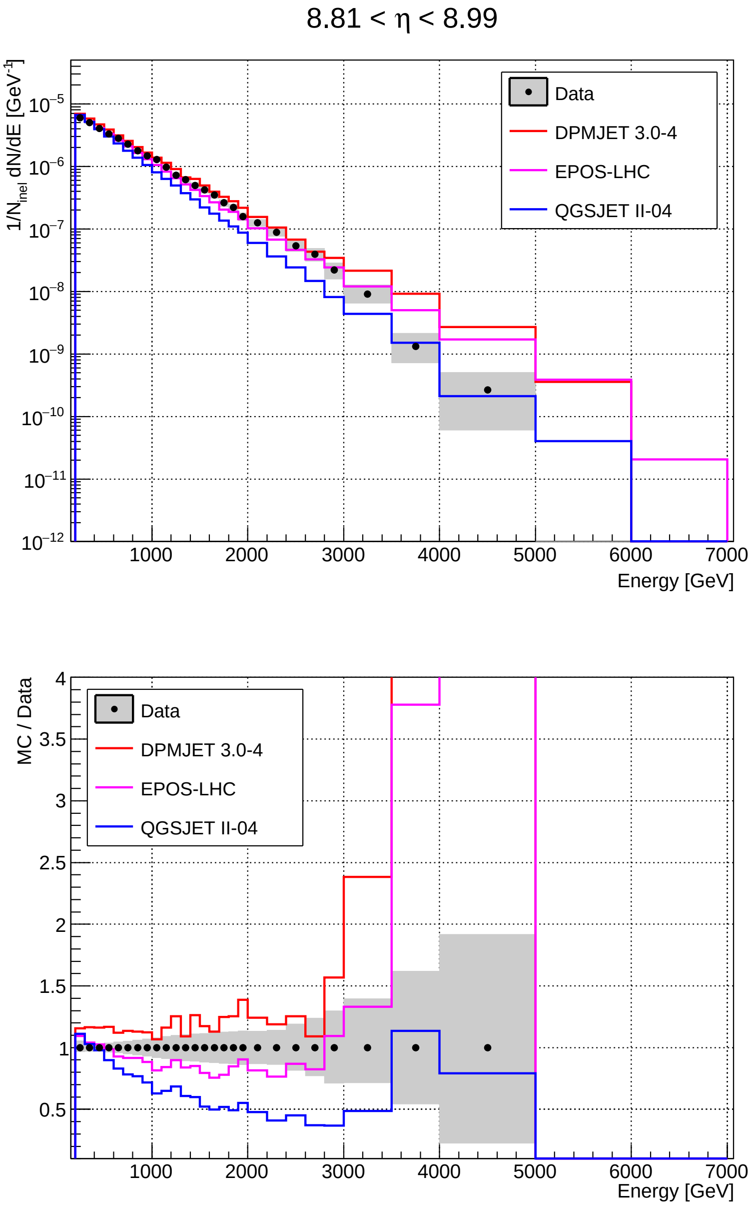

Figure 5.32: In the top picture, spectrum measured by the Arm2 large tower of LHCf before the unfolding (black points) compared with simulations propagated into the detector: DPMJET (red), QGSJET (blue) and EPOS (magenta). Grey shaded area represents the total error (statistical and systematical) of measured spectrum. In the bottom picture the ratio relative to data is shown.

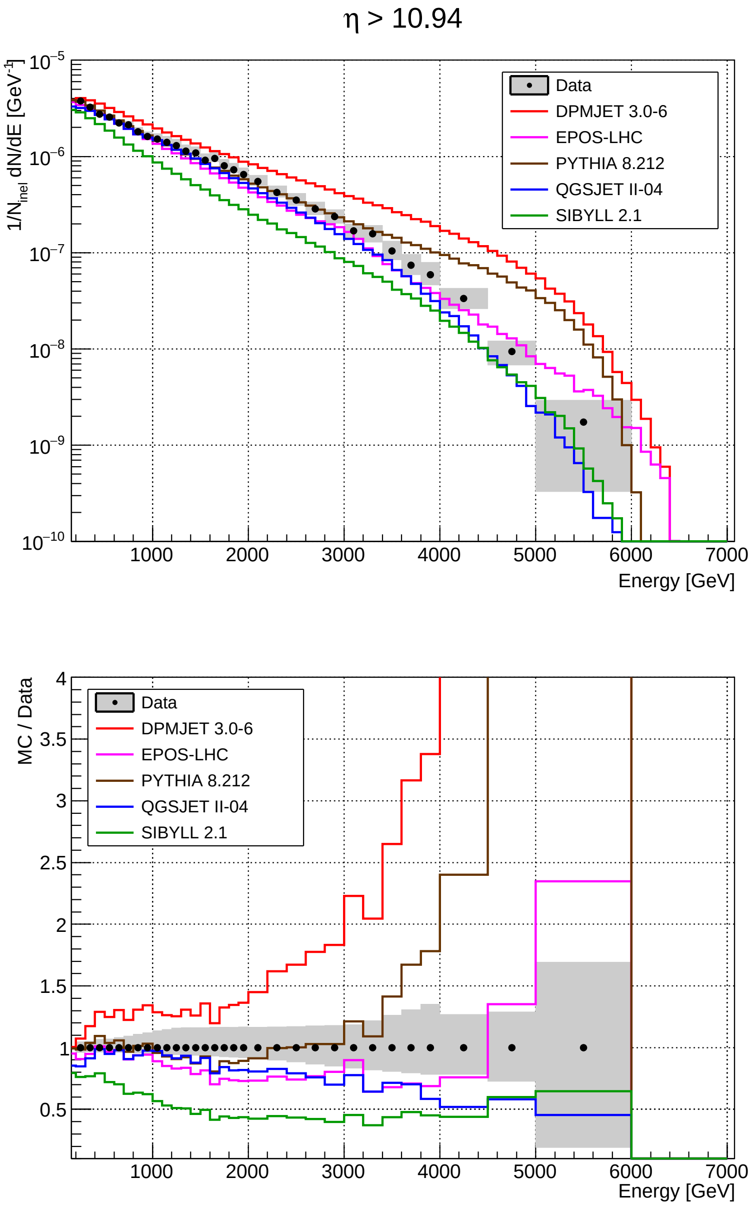

Figure 5.33: In the top picture, unfolded spectrum of the Arm2 small tower (black points) compared with the prediction of several Monte Carlo generators: DPMJET (red), QGSJET (blue), SIBYLL (green), EPOS (magenta) and PYTHIA (brown). Grey shaded area represents the total error (statistical and systematical) of measured spectrum. In the bottom picture the ratio relative to data is shown.

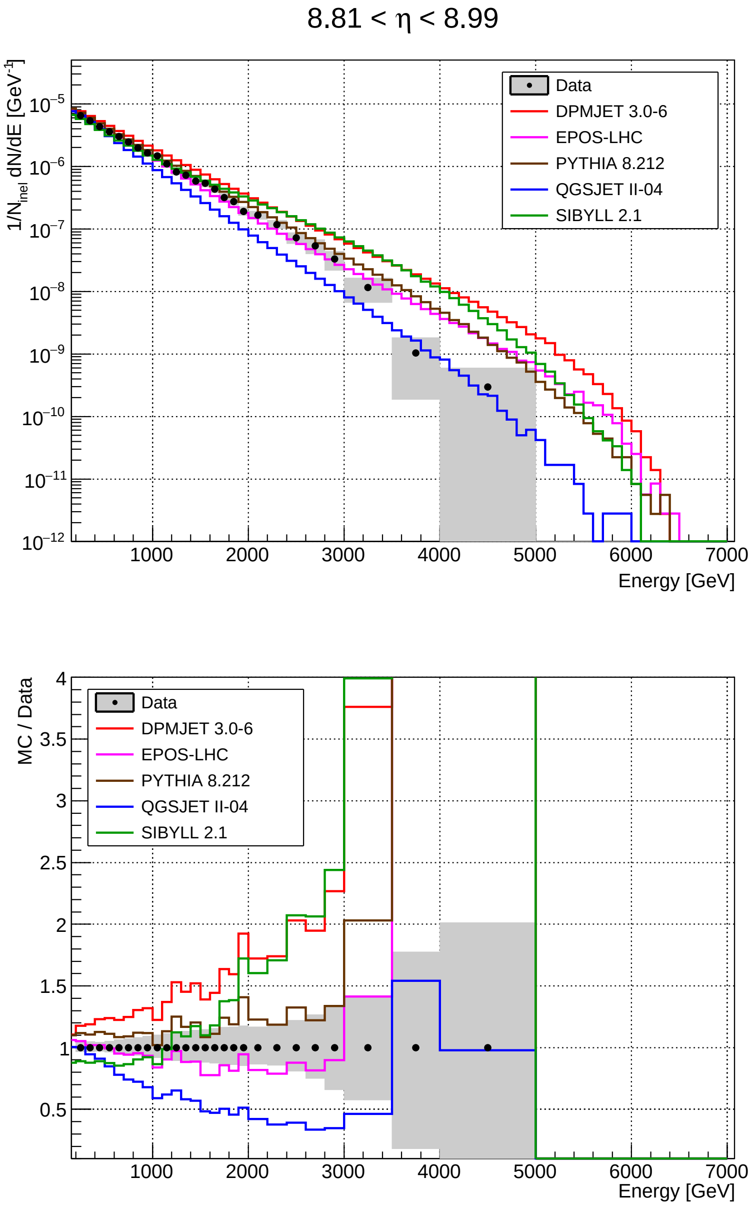

Figure 5.34: In the top picture, unfolded spectrum of the Arm2 large tower (black points) compared with the prediction of several Monte Carlo generators: DPMJET (red), QGSJET (blue), SIBYLL (green), EPOS (magenta) and PYTHIA (brown). Grey shaded area represents the total error (statistical and systematical) of measured spectrum. In the bottom picture the ratio relative to data is shown.

Chapter 6

Conclusions

The only way to measure cosmic rays at energies above $\sim 10^{15}$ eV is with indirect measurements from ground-based experiments. Accurate Monte Carlo simulations of the cosmic rays induced air-shower development in the atmosphere are required to extract astrophysical parameters of the cosmic rays, like their energy spectrum and mass composition. Simulations of air-showers use phenomenological hadronic interaction models, so they rely on experimental data for the tuning of their parameters. EPOS and QGSJET models were tuned using the data from the Run I of LHC, reducing the systematic uncertainty related to the discrepancy between the predictions of different models.

The LHCf experiment studies the very forward neutral particles produced in proton-proton and proton-lead collisions at LHC. This work described the analysis procedure to derive the energy spectrum of photons produced in proton-proton collisions at $\sqrt{s} = 13$ TeV with the Arm2 detector.

Before analysing the data, a study with Monte Carlo simulations was performed to deduce the relation between the total energy deposit in the calorimeters and the energy of the primary particle. The effect of the shower leakage and of the light collection efficiency of the scintillators was also estimated and a method to correct for the resulting non-uniformity of the detector response was found.

A beam test at SPS was performed to calibrate the detectors using both electron and muon beams. An energy resolution of $\sim 2\%$ was found with electromagnetic showers and the linearity of the calorimeters was better than 0.5%. The correction for the leakage and light collection efficiency was also tested, resulting in a non-uniformity suppressed to the $\sim 1\%$ level. The systematic error on the measurement of the calibration factors was estimated as 0.8%.

The data from collisions at $\sqrt{s} = 13$ TeV were reconstructed, corrected for the PID cut and unfolded to correct for the detector response. The sources of systematic errors were investigated. The final energy spectrum of photons was compared with the predicted spectra from several hadronic interaction models. In the pseudorapidity range $\eta > 10.94$, QGSJET and EPOS presents a good overall agreement with experimental data; PYTHIA spectrum agrees with data until ∼3.5 TeV but become harder at higher energies; DPMJET spectrum is generally harder than data while SIBYLL predicts a lower photon yield. In the pseudorapidity range $8.81 < \eta < 8.99$, EPOS spectrum agrees with data until ∼3 TeV, while it become harder at higher energies; QGSJET presents a lower yield of photons, while DPMJET, PYTHIA and SIBYLL spectra are generally harder than experimental data. Even if there is not a single model well reproducing data in the whole energy range, the measured spectrum lie between the predictions of the models.

Bibliography

[1] D. Perkins, *Particle Astrophysics.* Oxford University Press, 2 ed., 2009.

[2] J. A. Simpson, "Elemental and isotopic composition of the galactic cosmic rays," *Annual Review of Nuclear and Particle Science*, vol. 33, no. 1, pp. 323–382, 1983.

[3] P. Sokolsky, *Introduction to Ultrahigh Energy Cosmic Ray Physics.* Westview Press, 2004.

[4] T. K. Gaisser, *Cosmic rays and particle physics.* Cambridge Univ Press, 1990.

[5] M. S. Longhair, *High Energy Astrophysics.* Cambridge University Press, 3 ed., 2011.

[6] E. Fermi, "On the origin of the cosmic radiation," *Phys. Rev.*, vol. 75, pp. 1169–1174, Apr 1949.

[7] E. Fermi *Astrophys. J.*, vol. 119, p. 1, 1954.

[8] K. Greisen, "End to the cosmic ray spectrum?," *Phys. Rev. Lett.*, vol. 16, pp. 748–750, 1966.

[9] G. T. Zatsepin and V. A. Kuzmin, "Upper limit of the spectrum of cosmic rays," *JETP Lett.*, vol. 4, pp. 78–80, 1966. [Pisma Zh. Eksp. Teor. Fiz.4,114(1966)].

[10] J. Abraham *et al.*, "Measurement of the energy spectrum of cosmic rays above 10^{18} eV using the Pierre Auger Observatory," *Physics Letters B*, vol. 685, pp. 239–246, Mar. 2010.

[11] T. Abu-Zayyad *et al.*, "The cosmic-ray energy spectrum observed with the surface detector of the Telescope Array Experiment," *The Astrophysical Journal Letters*, vol. 768, no. 1, p. L1, 2013.

[12] C. Grupen and B. Shwartz, *Particle Detectors.* Cambridge Monographs on Particle Physics, Nuclear Physics and Cosmology, Cambridge University Press, 2008.

[13] J. Abraham *et al.*, "Properties and performance of the prototype instrument for the Pierre Auger Observatory," *Nuclear Instruments and Methods in Physics Research Section A: Accelerators, Spectrometers, Detectors and Associated Equipment*, vol. 523, no. 1–2, pp. 50 – 95, 2004.

[14] T. Abu-Zayyad *et al.*, "The surface detector array of the Telescope Array experiment," *Nuclear Instruments and Methods in Physics Research Section A: Accelerators, Spectrometers, Detectors and Associated Equipment*, vol. 689, pp. 87 – 97, 2012.

[15] V. N. Gribov, "A reggeon diagram technique," *Sov. Phys. JETP*, vol. 26, p. 414, 1968.

[16] T. Regge, "Introduction to complex orbital momenta," *Il Nuovo Cimento*, vol. 14, no. 5, pp. 951–976, 1959.

[17] LHC Forward Physics Working Group, "LHC Forward Physics," 2015.

[18] J. Blümer, R. Engel, and J. R. Hörandel, "Cosmic rays from the knee to the highest energies," *Progress in Particle and Nuclear Physics*, vol. 63, no. 2, pp. 293 – 338, 2009.

[19] O. Adriani *et al.*, "Measurement of zero degree single photon energy spectra for $\sqrt{s} = 7$ TeV proton–proton collisions at LHC," *Physics Letters B*, vol. 703, no. 2, pp. 128 – 134, 2011.

[20] O. Adriani *et al.*, "Measurement of zero degree inclusive photon energy spectra for $\sqrt{s} = 900$ GeV proton–proton collisions at LHC," *Physics Letters B*, vol. 715, no. 4–5, pp. 298 – 303, 2012.

[21] O. Adriani *et al.*, "Measurement of very forward neutron energy spectra for 7 TeV proton–proton collisions at the Large Hadron Collider," *Physics Letters B*, vol. 750, pp. 360 – 366, 2015.

[22] O. Adriani *et al.*, "Measurement of forward neutral pion transverse momentum spectra for $\sqrt{s} = 7$ TeV proton-proton collisions at the LHC," *Phys. Rev. D*, vol. 86, p. 092001, Nov 2012.

[23] O. Adriani *et al.*, "Transverse-momentum distribution and nuclear modification factor for neutral pions in the forward-rapidity region in proton-lead collisions at $\sqrt{s_{NN}} = 5.02$ TeV," *Phys. Rev. C*, vol. 89, p. 065209, Jun 2014.

[24] O. Adriani *et al.*, "Measurements of longitudinal and transverse momentum distributions for neutral pions in the forward-rapidity region with the LHCf detector," *Phys. Rev.*, vol. D94, no. 3, p. 032007, 2016.

[25] L. Evans, "The Large Hadron Collider," *New Journal of Physics*, vol. 9, no. 9, p. 335, 2007.

[26] M. Lamont, "Status of the LHC," *Journal of Physics: Conference Series*, vol. 455, no. 1, p. 012001, 2013.

[27] O. Adriani, L. Bonechi, M. Bongi, G. Castellini, R. Ciaranfi, R. D'Alessandro, M. Grandi, P. Papini, S. Ricciarini, A. Tricomi, and A. Viciani, "The construction and testing of the silicon position sensitive modules for the LHCf experiment at CERN," *Journal of Instrumentation*, vol. 5, no. 01, p. P01012, 2010.

[28] M. Tanaka, K. Hara, S. Kim, K. Kondo, H. Takano, M. Kobayashi, H. Ishibashi, K. Kurashige, K. Susa, and M. Ishii, "Applications of cerium-doped gadolinium silicate Gd_2SiO_5:Ce scintillator to calorimeters in high-radiation environment," *Nuclear Instruments and Methods in Physics Research Section A: Accelerators, Spectrometers, Detectors and Associated Equipment*, vol. 404, no. 2, pp. 283 – 294, 1998.

[29] T. Suzuki, K. Kasahara, K. Kawade, T. Murakami, K. Masuda, T. Sako, and S. Torii, "Performance of very thin Gd_2SiO_5 scintillator bars for the LHCf experiment," *Journal of Instrumentation*, vol. 8, no. 01, p. T01007, 2013.

[30] K. Noda *et al.*, *Data analysis of the LHCf Si microstrip sensors*, vol. 5, pp. 35–38. Institute of High Energy Physics, 2011.

[31] F. W. Bopp, J. Ranft, R. Engel, and S. Roesler, "Antiparticle to particle production ratios in hadron-hadron and *d*-Au collisions in the DPMJET-III Monte Carlo model," *Phys. Rev. C*, vol. 77, p. 014904, Jan 2008.

[32] R. Engel, J. Ranft, and S. Roesler, "Photoproduction off nuclei and pointlike photon interactions. I. Cross sections and nuclear shadowing," *Phys. Rev. D*, vol. 55, pp. 6957–6967, Jun 1997.

[33] S. Ostapchenko, "QGSJET-II: towards reliable description of very high energy hadronic interactions," *Nucl. Phys. B, Proc. Suppl.*, vol. 151, p. 143, 2006.

[34] E.-J. Ahn, R. Engel, T. K. Gaisser, P. Lipari, and T. Stanev, "Cosmic ray interaction event generator SIBYLL 2.1," *Phys. Rev. D*, vol. 80, p. 094003, Nov 2009.

[35] K. Werner, F.-M. Liu, and T. Pierog, "Parton ladder splitting and the rapidity dependence of transverse momentum spectra in deuteron-gold collisions at the BNL Relativistic Heavy Ion Collider," *Phys. Rev. C*, vol. 74, p. 044902, Oct 2006.

[36] T. Sjöstrand, S. Mrenna, and P. Skands, "PYTHIA 6.4 physics and manual," *Journal of High Energy Physics*, vol. 2006, no. 05, p. 026, 2006.

[37] T. Sjöstrand, S. Mrenna, and P. Skands, "A brief introduction to PYTHIA 8.1," *Computer Physics Communications*, vol. 178, no. 11, pp. 852 – 867, 2008.

[38] K. Kasahara, "Introduction to Cosmos and some relevance to ultra high energy cosmic ray air showers," *Proceedings of 24th International Cosmic Ray Conference, Rome*, vol. 1, p. 399, 1995.

[39] K. Kasahara, "Cosmos and Epics web page," *http://cosmos.n.kanagawa-u.ac.jp.*

[40] E. Berti, *Measurement of the energy spectra relative to neutrons produced at very small angle in* $\sqrt{s} = 13$ *TeV proton-proton collisions using the LHCf Arm2 detector.* PhD thesis, University of Florence, 2017 (unpublished).

[41] B. Rossi, *High Energy Particles.* Prentice-Hall, Englewood Cliffs, NJ, 1952.

[42] W. Heitler, *The Quantum Theory of Radiation.* Oxford University Press, London, 3 ed., 1954.

[43] K. Kawade, K. Fukatsu, Y. Itow, K. Masuda, T. Murakami, T. Sako, K. Suzuki, T. Suzuki, and K. Taki, "Study of radiation hardness of Gd_2SiO_5 scintillator for heavy ion beam," *Journal of Instrumentation*, vol. 6, no. 09, p. T09004, 2011.

[44] L. Bonechi *et al.*, "Development of the ADAMO detector: test with cosmic rays at different zenith angles," *Proc. of 29th Int. Cosmic Ray Conf. Pune*, vol. 9, pp. 283–286, 2005.

[45] K. A. Olive *et al.*, "Review of Particle Physics," *Chin. Phys.*, vol. C38, p. 090001, 2014.

[46] M. Aaboud, G. Aad, B. Abbott, *et al.*, "Luminosity determination in pp collisions at $\sqrt{s} = 8$ TeV using the ATLAS detector at the LHC," *The European Physical Journal C*, vol. 76, no. 12, p. 653, 2016.

[47] G. Antchev *et al.*, "Luminosity-independent measurement of the proton-proton total cross section at $\sqrt{s} = 8$ TeV," *Phys. Rev. Lett.*, vol. 111, p. 012001, Jul 2013.

[48] M. Morhac *et al.*, "Background elimination methods for multidimensional coincidence gamma-ray spectra," *Nuclear Instruments and Methods in Physics Research A*, vol. 401, pp. 113–132, 1997.

[49] M. Morhac *et al.*, "Efficient one- and two-dimensional gold deconvolution and its application to gamma-ray spectra decomposition," *Nuclear Instruments and Methods in Physics Research A*, vol. 401, pp. 385–408, 1997.

[50] M. Morhac *et al.*, "Identification of peaks in multidimensional coincidence gamma-ray spectra," *Nuclear Instruments and Methods in Research Physics A*, vol. 403, pp. 108–125, 2000.

[51] A. Lednev, "Electron shower transverse profile measurement," *Nuclear Instruments and Methods in Physics Research Section A: Accelerators, Spectrometers, Detectors and Associated Equipment*, vol. 366, no. 2, pp. 292 – 297, 1995.

[52] M. Paterno, "Calculating efficiencies and their uncertainties." Note available from home.fnal.gov/ paterno/images/effic.pdf, 2003.

[53] G. D'Agostini, "A multidimensional unfolding method based on Bayes' theorem," *Nuclear Instruments and Methods in Physics Research Section A: Accelerators, Spectrometers, Detectors and Associated Equipment*, vol. 362, no. 2, pp. 487 – 498, 1995.

[54] T. Adye, "Unfolding algorithms and tests using RooUnfold," in *Proceedings, PHYSTAT 2011 Workshop on Statistical Issues Related to Discovery Claims in Search Experiments and Unfolding, CERN,Geneva,*

Switzerland 17-20 January 2011, (Geneva), pp. 313–318, CERN, CERN, 2011.

[55] Results presented in the LHCf internal meeting on November 10, 2016 by E. Matsubayashi.

[56] L. D. Landau and I. J. Pomeranchuk, “Limits of applicability of the theory of bremsstrahlung electrons and pair production at high-energies,” *Dokl. Akad. Nauk Ser. Fiz.*, vol. 92, p. 535, 1953.

[57] A. B. Migdal, “Bremsstrahlung and pair production in condensed media at high-energies,” *Phys. Rev.*, vol. 103, p. 1811, 1956.

[58] T. Pierog, C. Baus, and R. Ulrich, “CRMC web page,” *https://web.ikp.kit.edu/rulrich/crmc.html.*

Appendices

Light collection efficiency at HIMAC

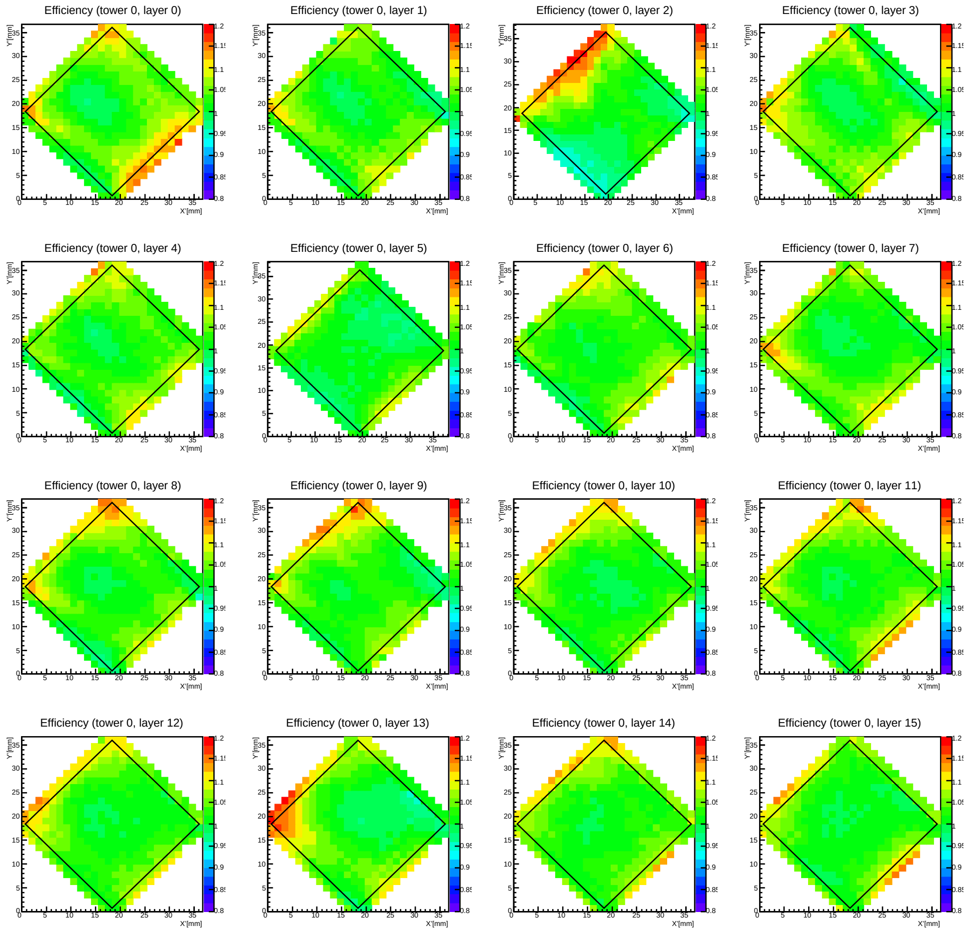
Efficiency (tower 0, layer 0)
Efficiency (tower 0, layer 1)
Efficiency (tower 0, layer 2)
Efficiency (tower 0, layer 3)
Efficiency (tower 0, layer 4)
Efficiency (tower 0, layer 5)
Efficiency (tower 0, layer 6)
Efficiency (tower 0, layer 7)
Efficiency (tower 0, layer 8)
Efficiency (tower 0, layer 9)
Efficiency (tower 0, layer 10)
Efficiency (tower 0, layer 11)
Efficiency (tower 0, layer 12)
Efficiency (tower 0, layer 13)
Efficiency (tower 0, layer 14)
Efficiency (tower 0, layer 15)

Figure 1: Light collection efficiency maps for all scintillator layers of small tower as a function of transverse position. The colour map represents the signal recorded by the PMT in that position, normalised to the signal recorded at the center of the scintillator. Since the grid of measurements was rotated by 45 degrees with respect to the scintillator, the map was rotated in the same way. The light guide is located in the upper-left side of the picture.

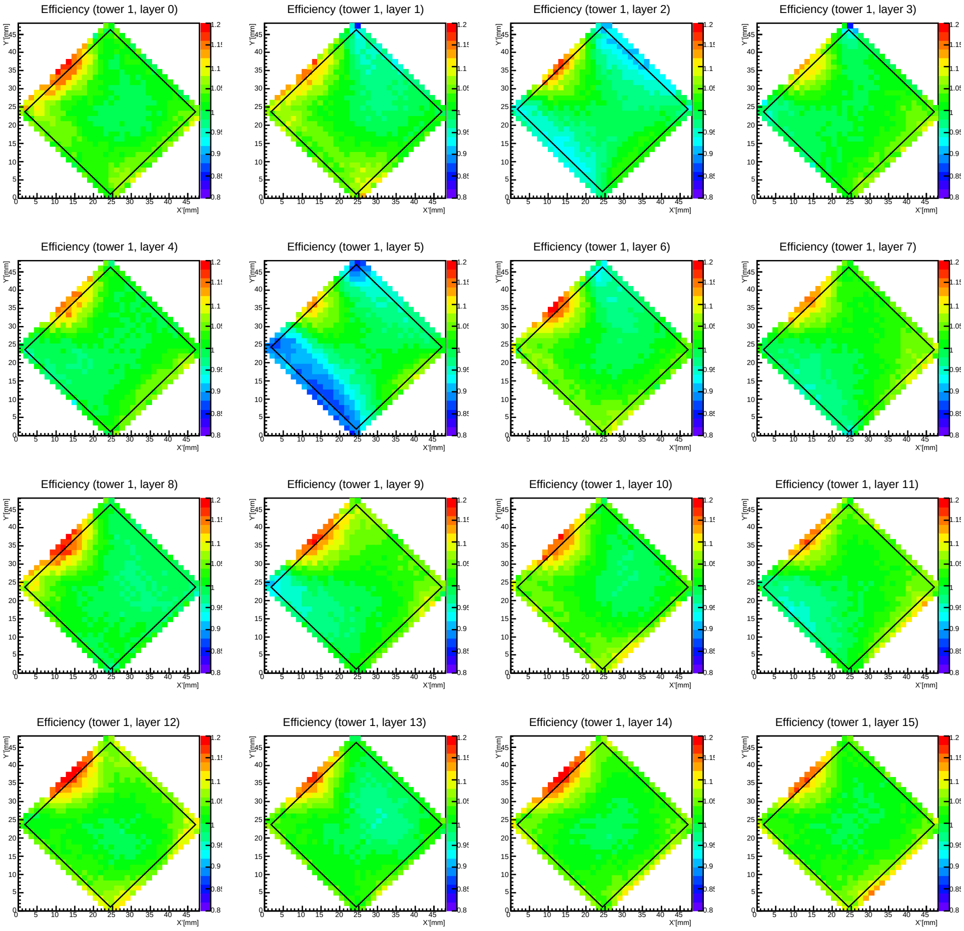

Efficiency (tower 1, layer 0)
Efficiency (tower 1, layer 1)
Efficiency (tower 1, layer 2)
Efficiency (tower 1, layer 3)
Efficiency (tower 1, layer 4)
Efficiency (tower 1, layer 5)
Efficiency (tower 1, layer 6)
Efficiency (tower 1, layer 7)
Efficiency (tower 1, layer 8)
Efficiency (tower 1, layer 9)
Efficiency (tower 1, layer 10)
Efficiency (tower 1, layer 11)
Efficiency (tower 1, layer 12)
Efficiency (tower 1, layer 13)
Efficiency (tower 1, layer 14)
Efficiency (tower 1, layer 15)

Figure 2: Light collection efficiency maps for all scintillator layers of large tower as a function of transverse position. The colour map represents the signal recorded by the PMT in that position, normalised to the signal recorded at the center of the scintillator. Since the grid of measurements was rotated by 45 degrees with respect to the scintillator, the map was rotated in the same way. The light guide is located in the upper-left side of the picture.

Position dependence correction

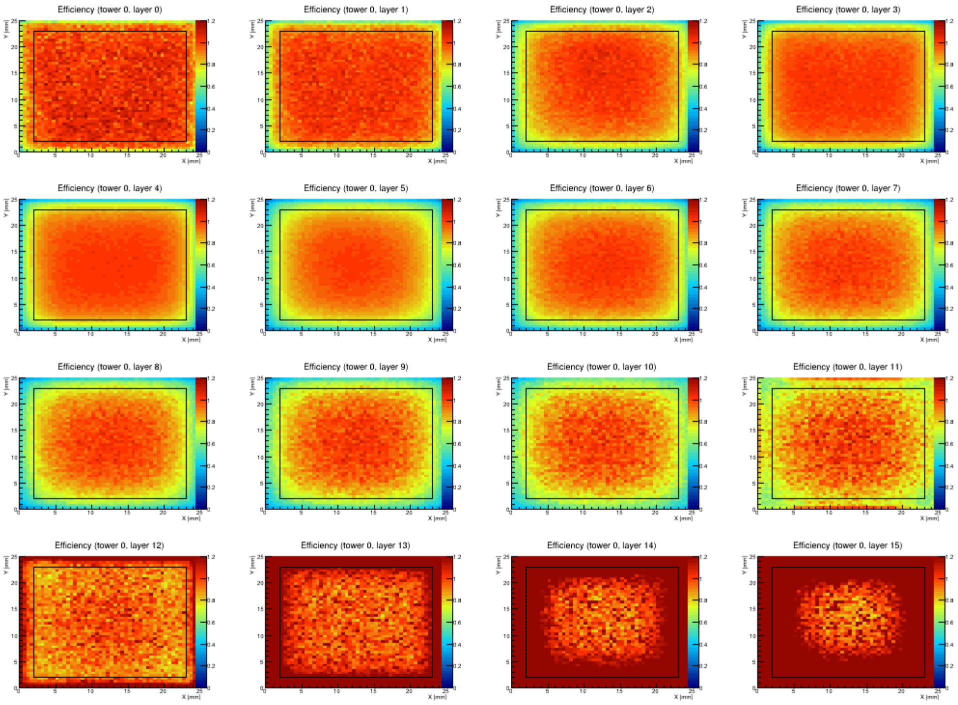

Figure 3: Position dependence correction map for all layers of the small tower generated with a 500 GeV photon Monte Carlo. Both leakage and light collection efficiency effects are implemented in the simulation.

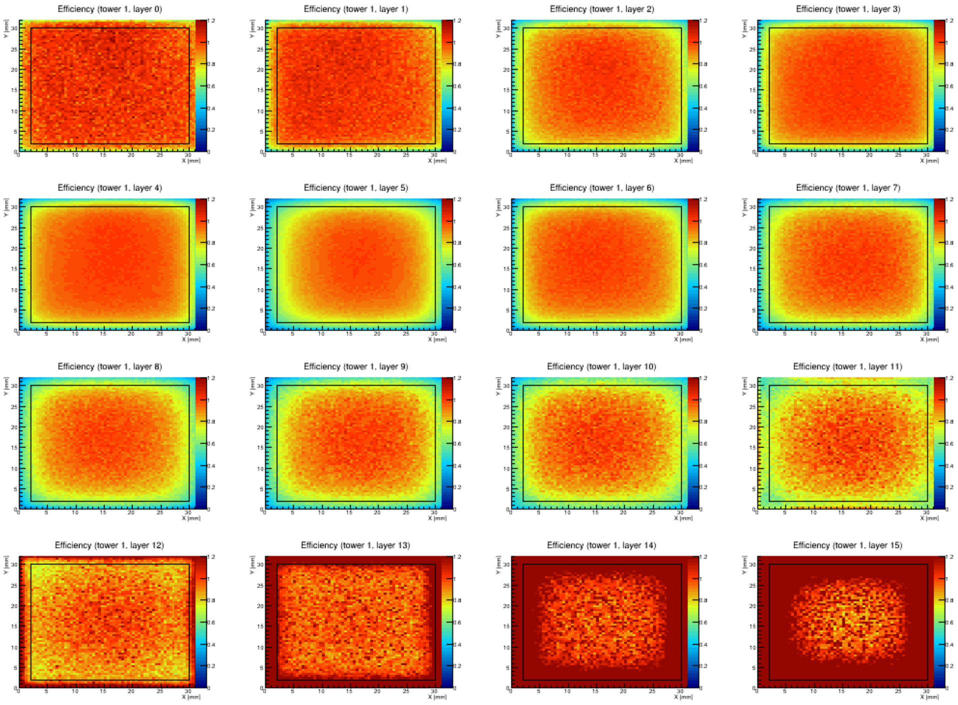

Figure 4: Position dependence correction map for all layers of the large tower generated with a 500 GeV photon Monte Carlo. Both leakage and light collection efficiency effects are implemented in the simulation.

Fits for electron-based conversion factors

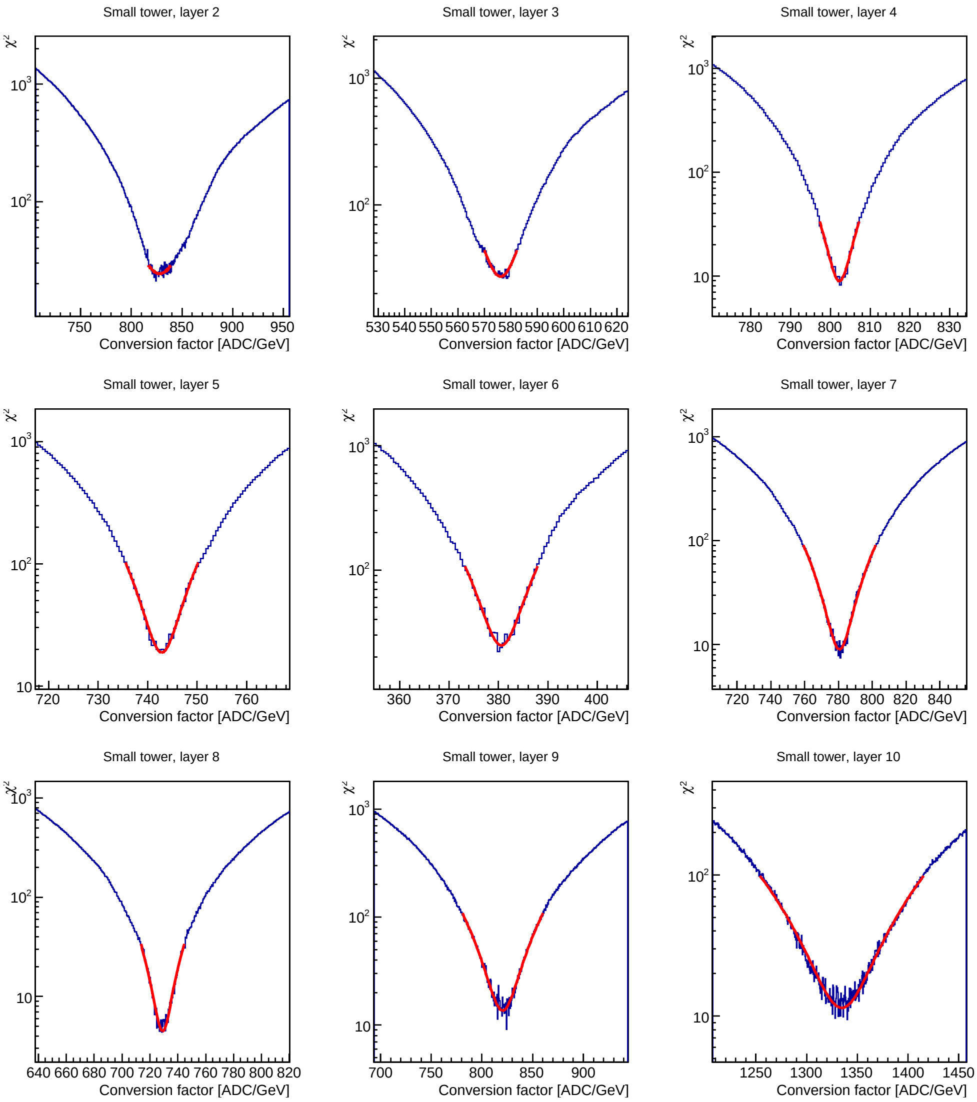
Small tower, layer 2

Small tower, layer 3

Small tower, layer 4

Small tower, layer 5

Small tower, layer 6

Small tower, layer 7

Small tower, layer 8

Small tower, layer 9

Small tower, layer 10

Figure 5: χ_j^2 as a function of C^j for the first 12 layers of small tower with 200 GeV electron beam (blue histogram). The fit function is represented as a red line.

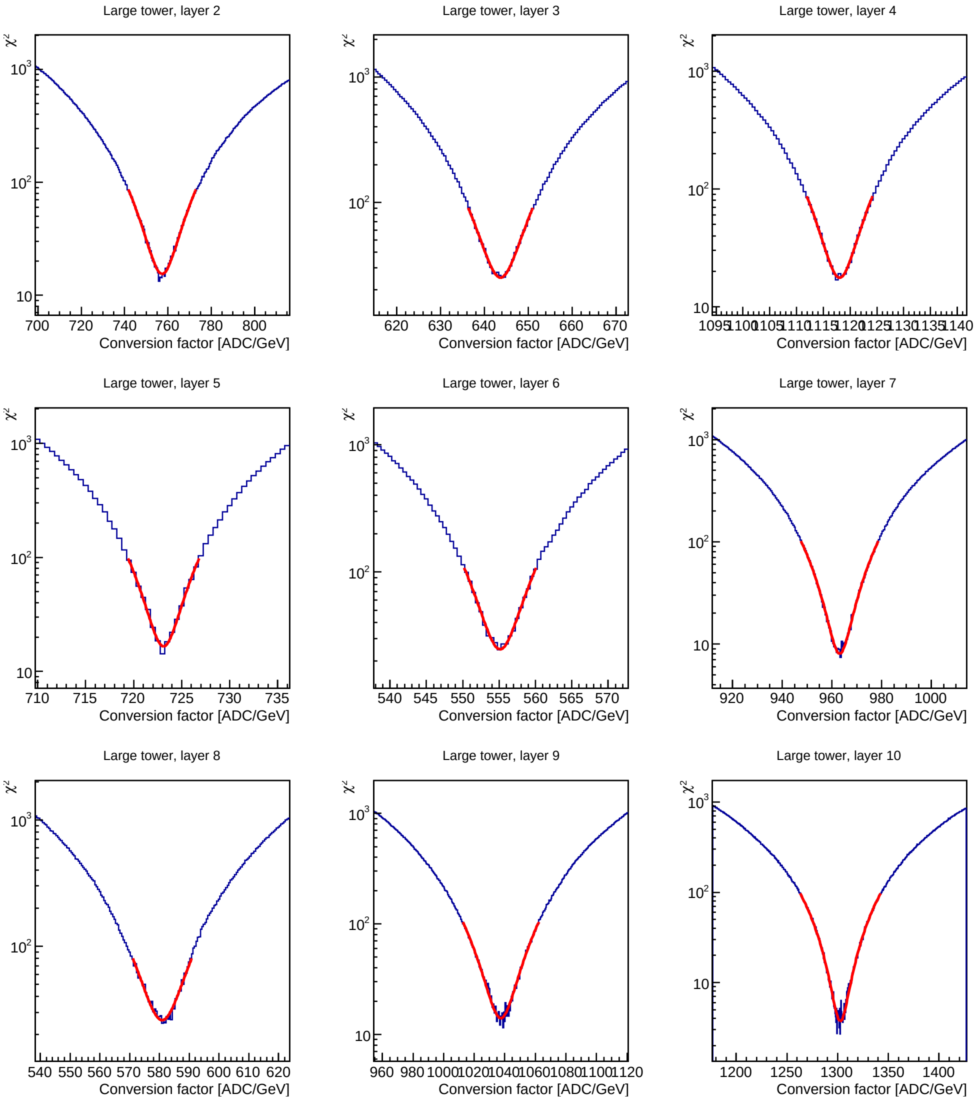

Figure 6: χ_j^2 as a function of C^j for the first 12 layers of small tower with 200 GeV electron beam (blue histogram). The fit function is represented as a red line.

Fits for muon-based conversion factors

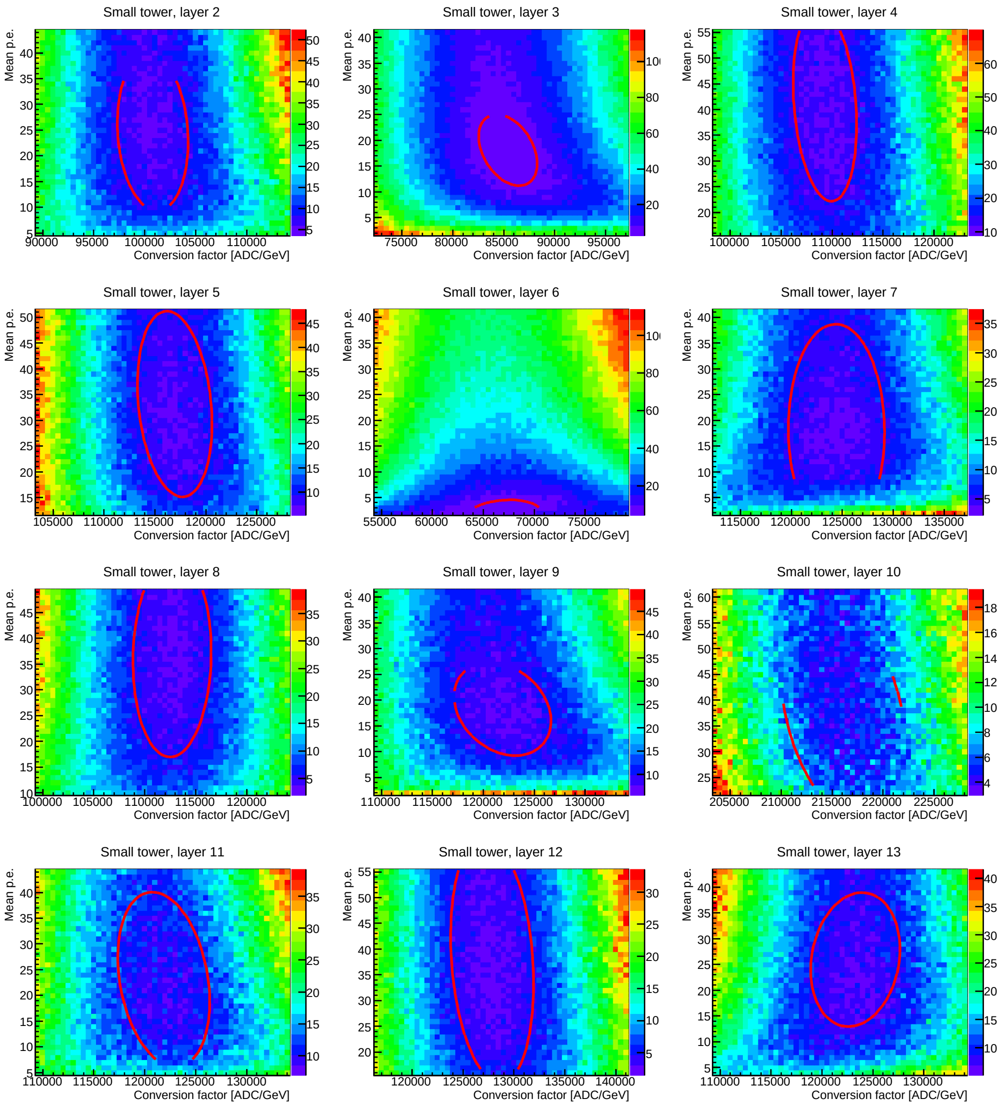

Figure 7: χ^2_j as a function of C_j (on X axis) and ν_j (on Y axis) for all the layers of small tower with 150 GeV muon beam. The colour map represents the value of the χ^2_j. The 1-σ confidence interval is plotted as a red line.

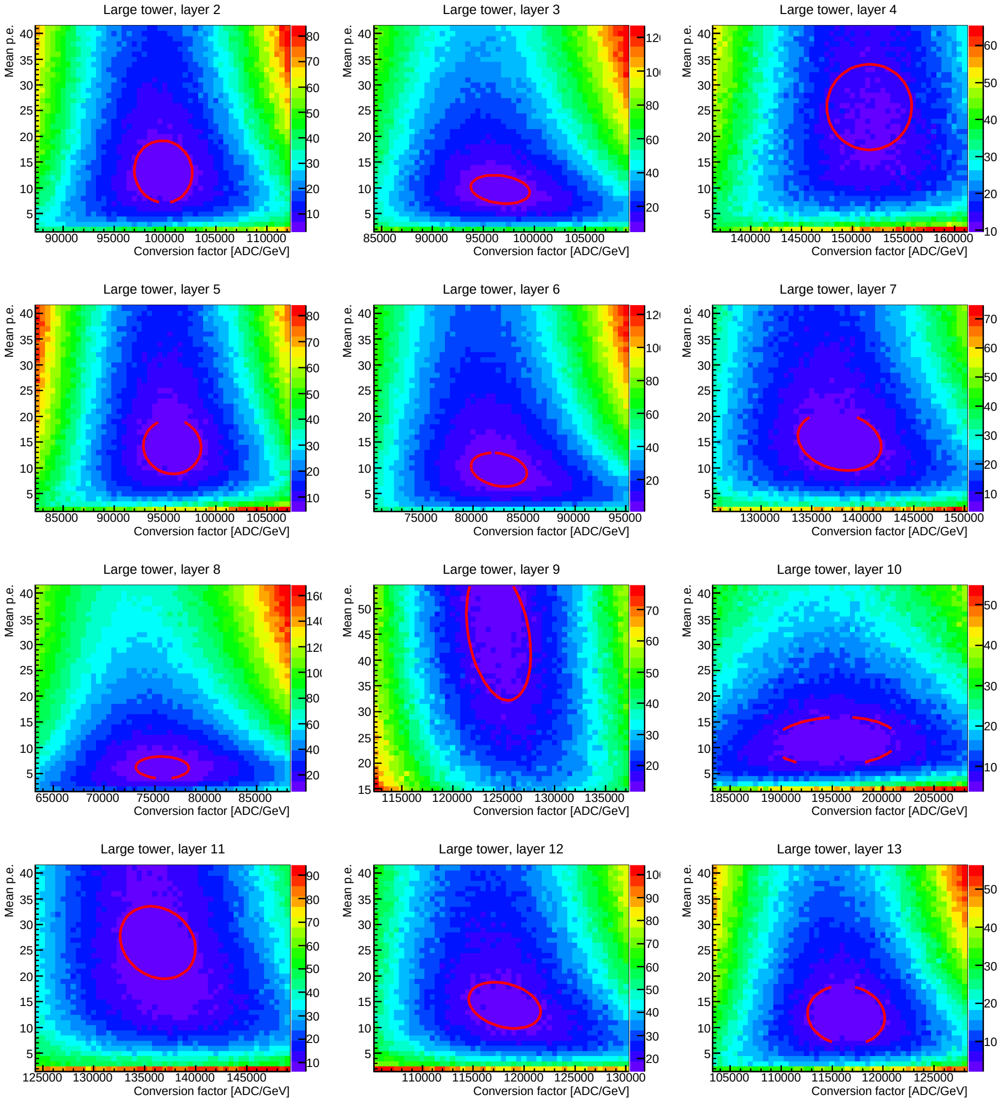
Large tower, layer 2

Large tower, layer 3

Large tower, layer 4

Large tower, layer 5

Large tower, layer 6

Large tower, layer 7

Large tower, layer 8

Large tower, layer 9

Large tower, layer 10

Large tower, layer 11

Large tower, layer 12

Large tower, layer 13

Figure 8: χ_j^2 as a function of C_j (on X axis) and ν_j (on Y axis) for layers from the 2nd to the 13th of the large tower with 150 GeV muon beam. The colour map represents the value of the χ_j^2. The 1-σ confidence interval is plotted as a red line

Ringraziamenti

Sono tante le persone che vorrei ringraziare per avermi aiutato durante lo svolgimento di questo lavoro. Un grazie in particolare al Dott. Lorenzo Bonechi per avermi aiutato nella stesura e nella correzione di questa tesi e al Prof. Oscar Adriani per avermi dato l'occasione di lavorare nel gruppo di raggi cosmici in questi anni e avermi dato la formazione grazie alla quale ho potuto concludere questo percorso di studi. Voglio ringraziare anche tutti gli altri colleghi del gruppo di raggi cosmici di Firenze per i loro consigli e la loro compagnia che sono stati fondamentali in questi anni. Sentiti ringraziamenti a tutti gli amici, dentro e fuori l'Università, che hanno contribuito a rendere meno pesante il lavoro in questi anni. Un rigraziamento in particolare al "compagno" Enrico per la sua compagnia e il suo supporto durante tutti questi anni di studi e ad Eugenio che mi ha accompagnato nelle tante lamentele in ufficio e in trasferta in questi 3 anni. Many thanks to all the colleagues in Japan for all the useful advice during my work and in particular to Makino, Zhou, Matsubayashi and Ueno for letting me enjoy my week in Nagoya and all the periods at CERN. Un sentito grazie ai miei genitori e alla mia famiglia per avermi sempre supportato nelle mie scelte e avermi dato l'opportunità di seguire questo percorso fino alla fine. Tutto questo non sarebbe stato possibile senza Kelushe, che nonostante le difficoltà incontrate durante il lavoro mi ha sempre sostenuto e ha fatto sì che questi siano stati gli anni più belli della mia vita.